DESIGN, FABRICATION, CHARACTERIZATION, AND CONTROL OF VO_2-BASED MICRO-ELECTRO-MECHANICAL ACTUATORS

by

Emmanuell J Merced

A DISSERTATION

Submitted to
Michigan State University
in partial fulfillment of the requirements
for the degree of

Electrical Engineering - Doctor of Philosophy

2014

ABSTRACT

DESIGN, FABRICATION, CHARACTERIZATION, AND CONTROL OF VO_2-BASED MICRO-ELECTRO-MECHANICAL ACTUATORS

by

Emmanuell J Merced

In this work, a vanadium dioxide (VO_2)-based micro-electro-mechanical actuator has been successfully designed, fabricated, characterized and controlled to achieve accurate displacements through the monolithic integration of a localized heater and self-sensing mechanism. VO_2 is a solid-to-solid phase transition material whose electrical, structural, and optical properties change abruptly as a function of temperature. Recent integration of this material in micro-actuators has shown strain energy densities, displacements, actuation speeds, and repeatability values comparable or, in some cases, superior to state-of-the-art micro-actuator technologies. Previous studies on VO_2 micro-actuators focus on open-loop manipulation of the device deflection, whose performance is highly susceptible to environmental disturbances and noises. In order to obtain accurate deflection control in micro-actuators, a closed-loop configuration is generally employed, which involves the use of external or internal displacement sensors. The incorporation of these sensors in micro-actuators usually increase design complexity, fabrication cost, and system footprint. Due to the multifunctional nature of VO_2, a self-sensing technique is achieved, where the micro-actuator deflection is estimated through VO_2 resistance measurements. In addition, the resistance-deflection hysteretic behavior is largely reduced due to the strong correlation between the electrical and structural transition, which greatly simplifies the self-sensing model. The closed-loop deflection control of these devices using self-heating actuation is also studied through voltage and current control, which reduces the need for additional heating components.

ACKNOWLEDGEMENTS

First and foremost I would like to thank my advisor Dr. Nelson Sepúlveda or like he wants me to call him ever since I met him: "Nelson". I am very grateful for his support, and encouragement throughout these years as a Ph.D. student. Apart from providing technical and research guidance, he has also offered me valuable advice that has helped me grow as an individual and professional.

I am deeply grateful to the members of the Applied Materials Group, who have provided friendship and guidance throughout the years. I would like to thank my colleague and friend Rafmag Cabrera, whom I have known from High School, for providing significant advice and collaborations. I also acknowledge David Torres for his unconditional help in performing some of the measurements and depositions used in this work. I am deeply grateful for the guidance and advice I received from Dr. Félix E. Fernández during my first two years of graduate studies.

Members of the Smart Microsystems Laboratory have been a source of invaluable collaborations, innovation, and ideas that have culminated in many of the experiments in this thesis. I would like to thank Dr. Xiaobo Tan for his insights and advice in smart materials and hysteresis compensation. Special thanks go to Jun Zhang who have provided solid theoretical knowledge and analysis for hysteresis compensated devices and systems.

I would also want to thank the National Science Foundation for funding my Ph.D through Grant DGE-0802267 (GRFP) and Grant CMMI-1301243. Thanks to Dr. Hogan for providing some of the resources used in experiments for this thesis.

Finally, I would like to thank my wife for her unconditional support and for joining me in this adventure. Thanks to my family, specially my mom, dad, and brother for believing in me and making all this possible. *Gracias a todos y gracias "Mamá"*.

TABLE OF CONTENTS

LIST OF TABLES

LIST OF FIGURES

CHAPTER 1

INTRODUCTION

Vanadium dioxide (VO_2) has been extensively studied due to its ability to change abruptly its electrical [20], optical [21], and structural [22] properties at a temperature of around 68 °C. However, it was not until recent years that the structural changes in VO_2 across its phase transition were used to produce produce micro-structures displacements orders of magnitude greater than similar sized thermal and electrostatic actuators [14, 23]. The successful integration of VO_2 thin films in micro-electro-mechanical systems (MEMS) fabrication processes has also enabled the design and fabrication of micro-actuators capable of achieving faster actuation speeds and lower power requirements [24, 25]. Despite these advances in VO_2-based micro-actuators the research is still limited to open-loop actuation of the devices, which constrains its use to maximum and minimum deflection values or with high errors across the transition. Other open-loop approaches require the use of complicated offline hysteresis model calculations to compensate for the highly hysteretic behavior [26]. By using closed-loop control of the device deflection in VO_2-based micro-actuators, the structural phase transition can be further exploited through the continuous actuation of the structure across the entire phase transition region, which produces the largest possible displacement.

Figure 1.1 shows a scanning electron microscope (SEM) superimposed image of a VO_2-coated silicon (Si) cantilever at both actuation limits with a maximum tip displacement of approximately 70 µm. These actuation limits correspond to the two VO_2 phases, observed at room temperature and 70 °C. The VO_2 deposition was performed using pulsed laser deposition (PLD). Note that the initial residual stress, which produces the cantilever deflection at room temperature, results from the VO_2 deposition. The total deflection of 70 µm during actuation is caused by the structural phase transition (SPT), during which the VO_2 crystallographic plane parallel to the Si substrate (100) plane contracts abruptly from

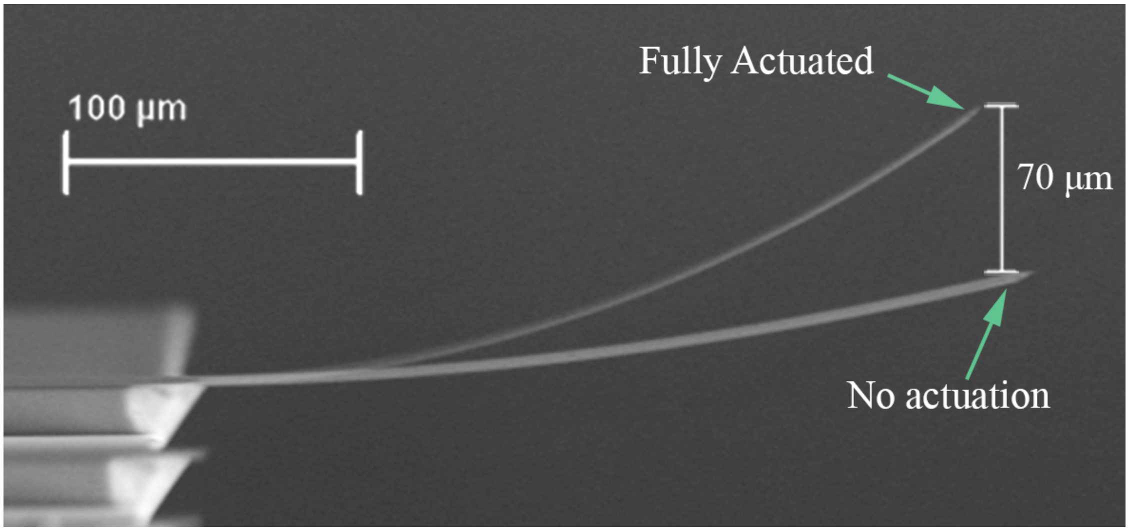

Figure 1.1: SEM image of a VO_2-coated silicon micro-cantilever at both actuation ends.

the monoclinic $(011)_{\mathrm{M}}$ to the rutile $(110)_{\mathrm{R}}$ VO_2 phases as the temperature is increased from room temperature. This lattice reorganization comes with a decrease of approximately 1.7 % of the plane area and is known to be fully reversible [14].

The deflection of the micro-cantilever across the transition is shown in **Figure** 1.2, which shows the hysteresis behavior as a function of temperature. The total actuation range is

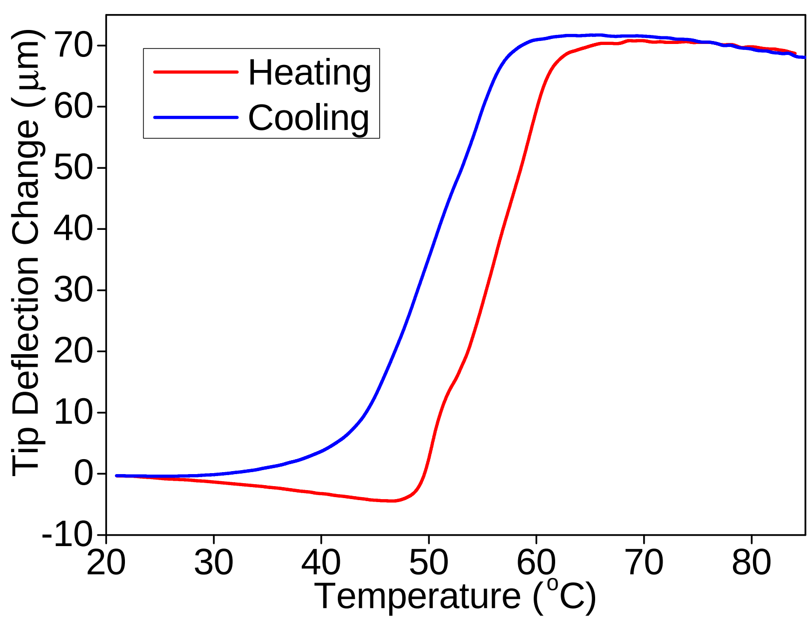

Figure 1.2: Deflection of a VO_2-coated silicon micro-cantilever as a function of temperature.

achieved through a temperature change of only 15 °C. The difficulties of achieving accurate actuation using open-loop are evident, not only due to the hysteresis, but also due to the non-monotonic behavior. In addition, the susceptibility to environmental disturbances and noises can hinder the performance of such devices.

Figure 1.3 shows the resistance of a VO_2 film as a function of temperature through the phase change. This type of transition is usually referred to as an insulator-to-metal transition (IMT). Although the IMT and the SPT occur at a slightly different temperature, both transitions are strongly correlated [27]. Using this correlation between the electrical and mechanical properties of the VO_2 film, it should be possible to estimate the deflection based on resistance measurements and reduce the hysteresis effect.

1.1 Problem Description and Motivation

Closed-loop control of the deflection in VO_2-based MEMS actuators is required for accurate and robust positioning throughout the complete deflection range of a micro-actuator device. This control can be achieved by inducing the transition through localized heating

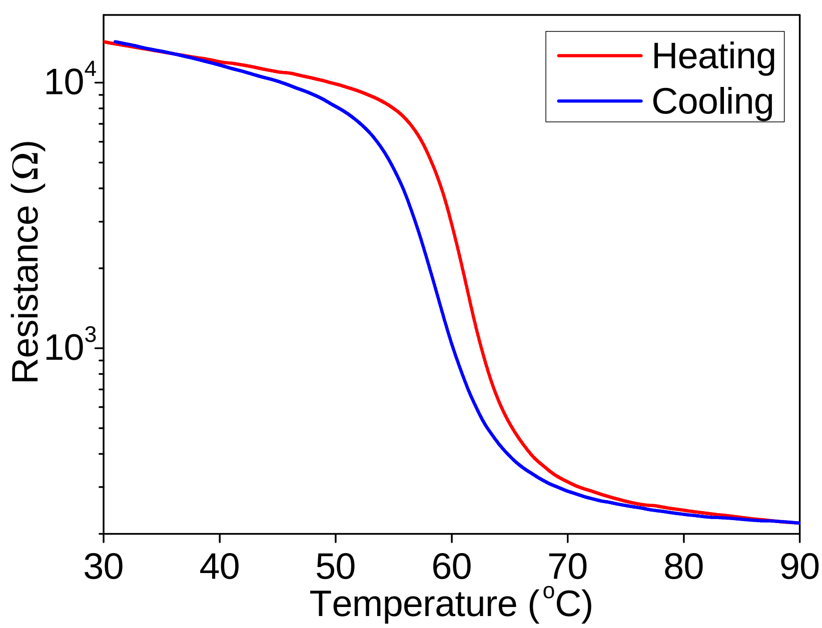

Figure 1.3: Resistance of a VO_2 film deposited on Si as a function of temperature.

and obtaining deflection measurements through the use of external or internal sensors for feedback purposes. In this thesis, both sensing configurations are explored, using a laser scattering technique for the external sensing mechanism and self-sensing — estimation of deflection through resistance measurements — as the internal mechanism. The latter, not only reduces the size and complexity of the system, but also, reduces the hysteresis between deflection and resistance due to the strong correlation between the IMT and SPT. These sensing techniques, in combination with the design and fabrication of a MEMS device, are used to develop an accurate controlled VO_2-based MEMS micro-actuator. In addition, self-heating of the VO_2 will be used as an alternative actuation method, which contributes to further device miniaturization. The problems addressed in this thesis are:

- A detailed study of VO_2-coated micro-actuators must be achieved, which includes quasi-static and photo-thermal actuation, calculations of strain energy density, and demonstration of self-sensing and hysteresis reduction between deflection and resistance.

- A VO_2-based MEMS actuator with monolithically integrated heater and self-sensing mechanism must be designed and fabricated.

- The MEMS actuator must be characterized in terms of quasi-static, frequency, and time responses, reliability, and rate dependency.

- Dynamic actuator deflection model in the thermal and mechanical domains needs to be derived (for controller design purposes).

- A suitable resistance-to-deflection self-sensing model must be determined.

- Closed-loop controlled performance of the actuator needs to be validated through closed-loop frequency, step, and sinusoidal reference tracking.

- For self-actuation of the VO_2-based MEMS actuator, the deflection must be controlled by controlling the supplied voltage or current to the VO_2.

A series of experiments, simulations and analytical approaches are used to address these problems. The techniques used for the characterization, self-sensing, and self-actuation control of this actuator can also be used for other types of VO_2-based structures. References [28–32] are the publications resulting from the work done in this thesis.

1.2 Thesis Statement

This thesis presents the development of an accurate VO_2-based MEMS actuator. The main contributions are: demonstration of VO_2 capabilities as a smart material in terms of strain energy density, overall quasi-static displacement, photo-thermal actuation and self-sensing — the use of VO_2 resistance for actuator deflection estimation; the design and fabrication of a fully controlled VO_2-based MEMS actuator; the integration of VO_2 resistance measurement in the device, which enables simultaneous *in situ* resistance and deflection measurements; the demonstration of VO_2 cross-property hysteresis reduction across the complete actuation range using the resistance-deflection relationship; the use of self-sensing as an integrated sensing mechanism in the MEMS device for achieving accurate deflection control, which eliminates the need for external deflection measurement methods; thorough actuator characterization including quasi-static response, frequency and time domains, reliability, and rate dependency; analytical and numerical micro-actuator thermal and mechanical modeling for use in controller design and results validation; demonstration of the closed-loop actuator performance through a series of reference tracking experiments, which includes closed-loop frequency response, and step and sinusoidal reference tracking; demonstration of closed-loop controlled self-actuation of the VO_2-based MEMS actuators using voltage and current control techniques.

Thesis Statement: *The development of an accurate VO_2-based micro-electro-mechanical actuator is achieved through the successful integration of monolithically integrated electro-thermal heater, self-sensing/self-actuation mechanisms, and closed-loop control, which en-*

hances the performance of these devices (in terms of energy density, robustness, etc.) and broadens their applications for micro-positioning and deflection tracking.

1.3 Anticipated Research Contributions

In this thesis, the problems described in **Section 1.1** will be addressed. The mechanical actuation process in VO_2 will be studied in terms of quasi-static and dynamic displacement, strain/stress, and strain energy density measurements, which will be compared with other smart materials. In addition, the hysteresis reduction effect between resistance and deflection will be demonstrated, which will enable the use of simpler control techniques. The results from these studies will demonstrate the advantages of using VO_2 as the active layer in MEMS actuators. The successful design and fabrication of a monolithically integrated heater and self-sensing mechanism will allow for further miniaturization of current VO_2 actuator technologies. By characterizing the micro-actuator, a deeper understanding of the deflection and resistance effects can be reached and used for future optimizations. Dynamic models for the thermal and mechanical actuator domains in combination with a non-hysteretic self-sensing model will provide the tools needed for controller design. The closed-loop performance validation and testing will provide bandwidth, transient, and frequency dependent information. By controlling the voltage and current through the VO_2 thin film, the deflection of the micro-actuator will be induced. This self-heating technique will be combined with closed-loop feedback in order to obtain accurate deflection control.

1.4 Dissertation Outline

The remaining chapters are organized as follows; **Chapter 2** presents a thorough background on the MEMS actuator techniques, feedback control in micro-actuators, and the electrical and structural transition in VO_2. In **Chapter 3**, a study of the VO_2 capabilities are presented, which involves quasi-static and photo-thermal actuation, as well as the micro-actuator figure of merit: the strain energy density. In addition, the self-sensing effect is briefly studied. All the research performed in this chapter is done in non-MEMS devices and is used to substantiate the thesis statement and the self-sensing and actuation methods used in this thesis. **Chapter 4** shows the design and fabrication of a VO_2-based MEMS actuator with monolithically integrated electro-thermal heater and VO_2 resistance measurement electrodes for self-sensing. In **Chapter 5**, a detailed device characterization and closed-loop controlled experiments are performed using an external deflection sensor. **Chapter 6** presents the use of self-sensing feedback in a VO_2-based MEMS actuator for accurate deflection control. **Chapter 7**, shows the results obtained by using self-heating of the VO_2 achieved by voltage and current control techniques. Finally, **Chapter 8** presents a summary of contributions of this thesis.

CHAPTER 2
BACKGROUND

2.1 Micro-actuators

Micro-mechanical actuators are devices with micrometer dimensions that can convert one type of energy or signal into another. In many cases, the output signal of an actuator is the displacement or force of a suspended structure (e.g. cantilever, membrane, rotating gear) [1–9, 19, 33–42]. They are characterized by the amount of work that they can perform, and can be classified according to the type of energy or signal they receive and how they convert it. A review on the many actuation techniques was published in 2005, which includes selection criteria [37].

There are different actuation methods that have been used successfully, such as thermal [2–4, 19, 39, 40], electrostatic [5–7, 35–38], magnetic [33, 34], and piezoelectric [8, 43, 44]; all of which have their advantages, limitations, and trade-offs. Some of these advantages and limitations are: fabrication simplicity, resolution, efficiency, motion range, force and actuation speeds. Due to the many applications available for micro-actuators there is no single type of actuation mechanism that can meet all the requirements. However, the most common actuation mechanisms for micro-actuators are thermal and electrostatic. VO_2 can be categorized as a thermal-based actuation, although it is also a smart material with particularly interesting multifunctional capabilities.

2.1.1 Thermal Actuators

The family of thermal actuators can be divided according to the phenomenon caused by the difference in temperature. Among all the types of mechanical actuators, shape memory alloy (SMA) actuators (also considered a type of smart material) offer the highest strain energy density [37]. They have been used to develop wireless bio-mimicking micro-robots [1] (see **Figure** 2.1). However, their dimensions are typically in the millimeter range and the

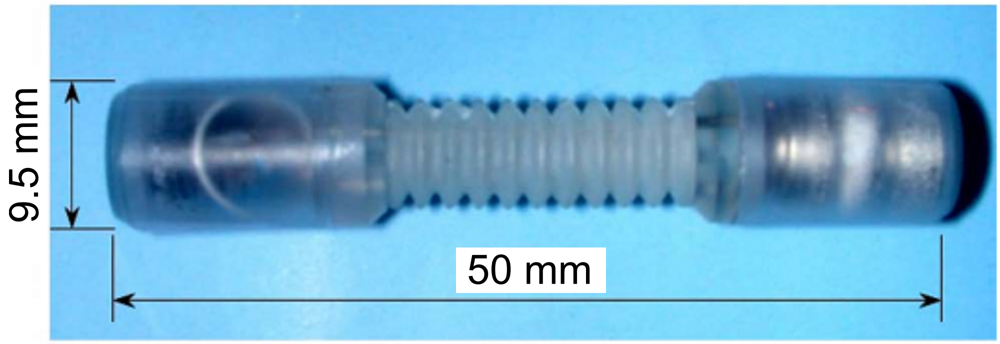

Figure 2.1: A wireless bio-mimicking micro-robot with shape memory alloys actuators [1].

reported displacements are not larger than 35 µm [19]. Thermo-pneumatic actuation can be achieved by changing the pressure level inside a cavity using a heater electrode that moves the sealing diaphragm. A corrugated silicon diaphragm (which is more flexible than a flat one) was driven by thermo-pneumatic actuation and the maximum displacement was 40 µm [2] (see **Figure** 2.2). The third sub-class of thermal actuators uses thermal expansion

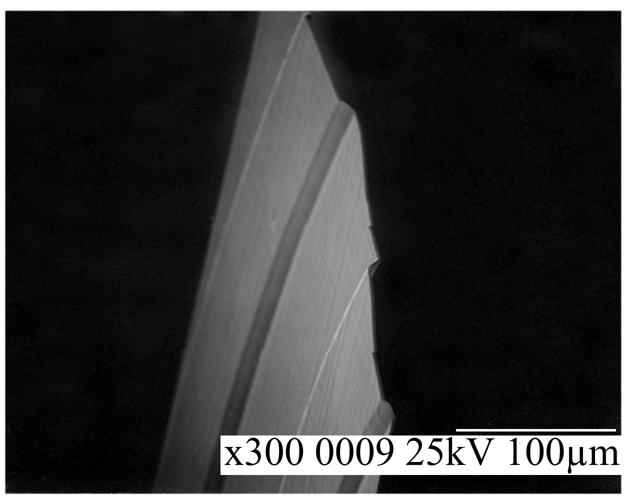

Figure 2.2: A corrugated diaphragm driven by thermo-pneumatic actuation [2].

mechanisms. Thermal expansion actuators are basically released structures (e.g. cantilevers) made out of at least two different materials with different thermal expansion coefficients. When heated, the difference in the thermal expansion coefficients causes both layers to expand at different rates. This produces a cantilever bending in a direction perpendicular to both films, with the film with the lowest thermal expansion coefficient facing the inner side of the arc formed by the cantilever. The largest displacements that have been observed with this type of actuators use some type of polymer as one of the materials that form the bilayer cantilever. Polyimide based bilayered cantilevers have shown impressive bending capabilities [39]. However, once again, the dimensions of these cantilevers are in the millimeter range. Other smaller cantilevers (300 µm long and shown in **Figure** 2.3) have also been coated with polymers to obtain deflections up to 50 µm [3]. The use of polymers limits the use of

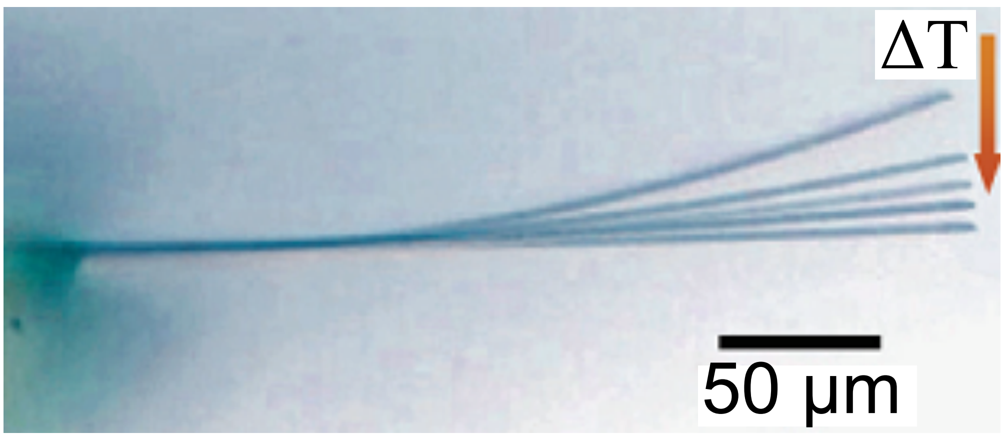

Figure 2.3: Bilayered polyimide coated micro-cantilever [3].

such cantilevers for temperatures below their melting temperature (approximately 400 °C). Finite element methods have been used to optimize the actuator geometry for maximum deflections on thermal actuators about 150 µm long and 50 µm wide, but no deflections larger than 20 µm were obtained [4, 40]. An example of the V-shaped actuator optimized in [4] is shown in **Figure** 2.4.

2.1.2 Electrostatic Actuators

Micrometer sized electrostatic actuators use the attractive (or repelling) force between two charged plates or surfaces. When they are fabricated in the micrometer scale, they can sustain very high electric fields since the gaps between the charged surfaces can be smaller

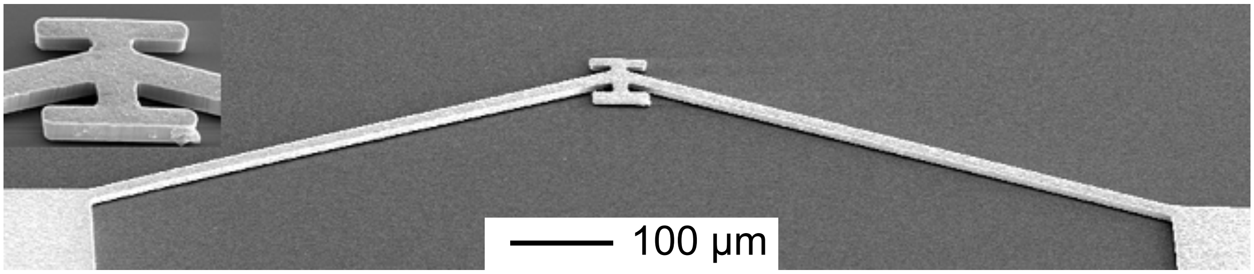

Figure 2.4: V-shaped thermal actuator [4].

than the mean free path of particles in air at room temperature (approximately 6 μm). Electrostatic comb-drives have been actuated with 20 V and achieved displacements close to 30 μm [35]. Later improvements in the design and fabrication led to displacements of up to 150 μm in 1 ms on comb-drive devices actuated with 150 V, which is shown in **Figure** 2.5 [5]. Comb-drives are usually the type of devices used for actuating micro engines. Although relatively large torques have been delivered, because the gear movement is rotational (angular motion), the linear displacements have been close to 40 μm and angular velocities of up to 6 rpm (see **Figure** 2.6) [6,36]. However, other types of electrostatic actuators, such as scratch

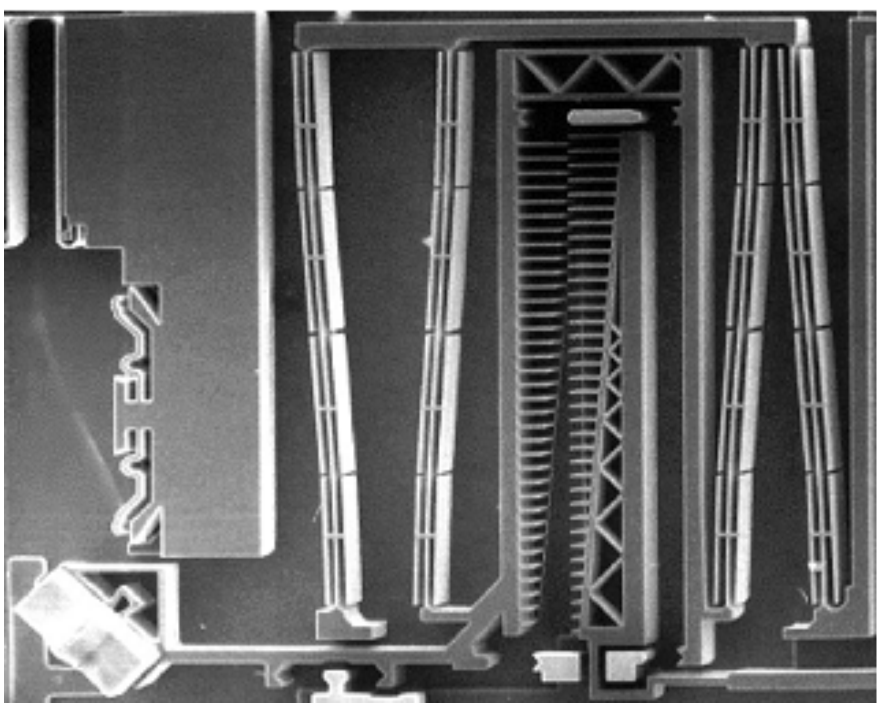

Figure 2.5: Electrostatic linear comb-drive micro-actuator [5].

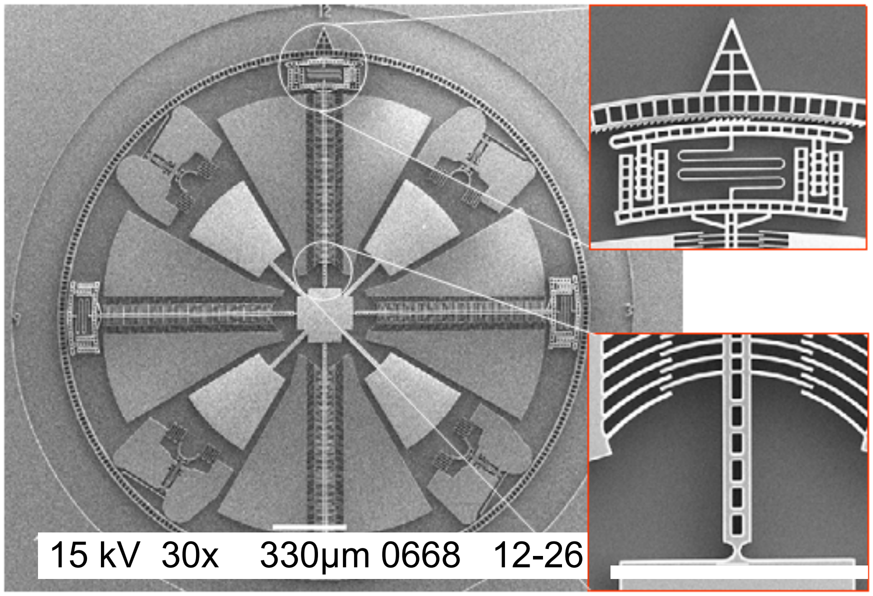

Figure 2.6: Micro rotational motor driven by electrostatic comb-drive actuators [6].

drives and impact actuators, can be used to obtain deflections as large as 200 μm [37]. Impact actuators need multiple motions (or impacts) in order to get a total displacement

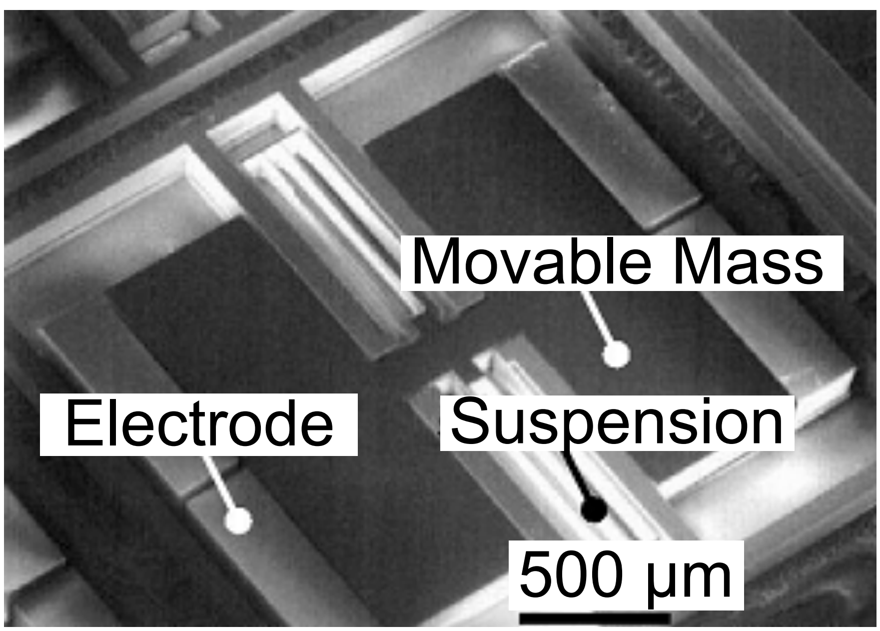

Figure 2.7: A impact micro-actuator driven with AC signals [7].

in the micrometer range. For example, an AC voltage signal with amplitude of 100 V and frequency of 200 Hz was applied to the impact micro-actuator shown in **Figure** 2.7 for

500 ms and a displacement of 1.35 µm was obtained [7]. The dimensions of this device were 3 mm × 3 mm × 600 µm. The device was tested for over 550 cycles on a fixed sample and survived without any deterioration. Scratch drive actuators are also usually operated by an AC voltage and can supply forces close to 1 mN and have displacements close to 200 µm [38].

2.1.3 Smart Actuators

More recently, researchers have found that smart materials — the most common being piezoelectrics, electroactive polymers and phase-change materials — provide new actuation mechanisms capable of performing beyond the theoretical limits of the technologies mentioned above. Smart materials are materials engineered to obtain a significantly amount of change in one or more of its properties, which can be controlled by an external stimuli (e.g. temperature, electric field, etc...). Piezoelectrics are materials that produce stress when a voltage is applied across it. Piezoelectric-based actuators — example shown in **Figure** 2.8 — can generate forces up to 1 mN, and displacements up to 200 µm [8]. These types of actuators require relatively high operation voltages, involve complex compounds (and sometimes toxic; e.g. lead) which complicates their deposition as thin films and limits their applicability in MEMS and NEMS (especially for bio-related applications). Nevertheless, they have

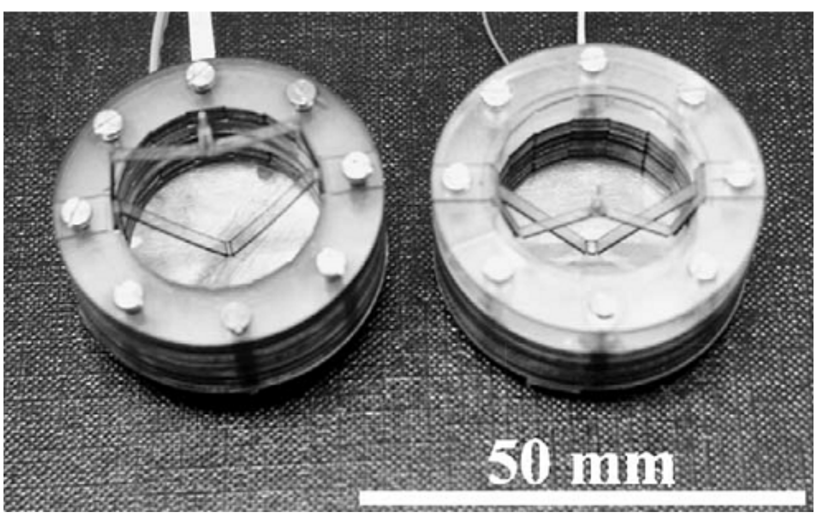

Figure 2.8: A piezoelectric-based micro-actuator [8].

a clear advantage in terms of speed, with frequency responses near 10 kHz, which could be increased by up to two orders of magnitude in piezoelectric bimorph geometries at the cost of a substantial reduction in force capabilities [37].

Electroactive polymers are another type of smart material that produces a deformation, greater than that of piezoelectrics, when a voltage is applied to it. Electroactive polymer-based actuators have demonstrated good performance in air and liquid environments [41,42], which makes them suitable for biomedical applications. They also operate at very low power with highest strain energy density in the vicinity of $5 \times 10^4\,\mathrm{J\,m^{-3}}$ for the micro-actuator in **Figure** 2.9 [9].

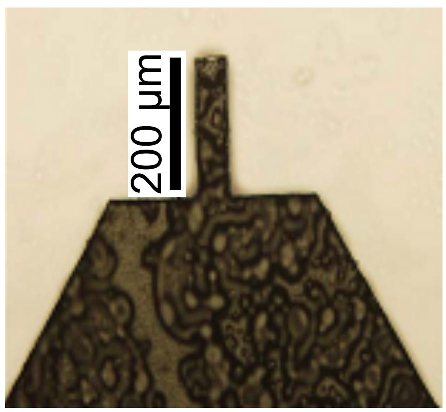

Figure 2.9: An electroactive polymer micro-actuator [9].

Phase change materials are yet another type of smart material that produces an abrupt change in stress through their phase transformation, which is usually thermally induced. SMAs are an example of phase change materials with very high strain energy densities of approximately $10^7\,\mathrm{J\,m^{-3}}$ obtained through the austenite-martensite transformation [19]. An example of a TiNi SMA-based micro-actuator is shown in **Figure** 2.10. The micro-gripper is able to completely close its fingers making it possible to grab microscopic particles [10]. Although other types of phase-change materials exist, their structural changes are not as attractive for actuator applications and their transition temperatures are much farther of room temperature than that of VO_2. For example, an alloy of germanium-antimony-tellurium ($Ge_2Sb_2Te_5$) produces very small deflection changes compared to those observed in VO_2

and SMA. In addition, the deflections observed are a result of an irreversible crystallization process that occurs at temperatures above 300 °C, which are not ideal conditions for micro-actuators [45].

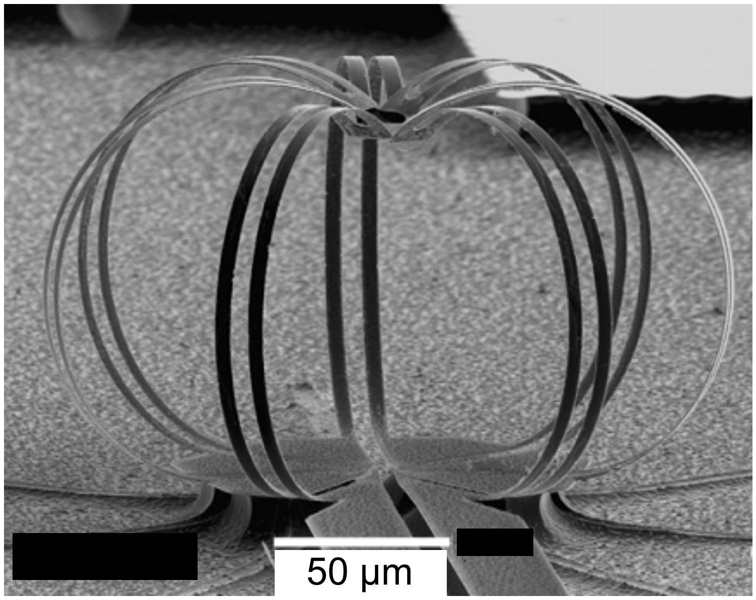

Figure 2.10: An SMA-based micro-gripper under full actuation [10].

2.2 Feedback Control of Micro-actuators

Regardless of the actuation method used for driving micro-actuators, in most applications (e.g. micro-positioning and micro-manipulation) accurate and precise displacement values. This performance can be achieved by actively compensating the actuation signal using feedback control of the displacement. Every sensing and control approach that can be used to achieve such control comes with specific implications on the overall device performance. The following discusses some of the most common sensing and actuation techniques used in micro-actuators.

2.2.1 Sensing Techniques

The developed techniques for the measurement or estimation of displacements of MEMS-based actuators can be divided into two main groups: internal and external sensors. A piezoresistor, for example, can be used as an internal sensor by incorporating it in the device fabrication process and optimizing its location to increase sensing sensitivity. Piezoresistor materials, such as boron doped Si, produce a change in resistivity due to a stress change in the material. An example of piezoresistors (PMT) used in micro-actuation sensing and feedback is shown in **Figure** 2.11, where a Wheatstone bridge configuration is used to cancel out thermal effects [11]. Strain gauge sensors are yet another type of internal sensing mechanism,

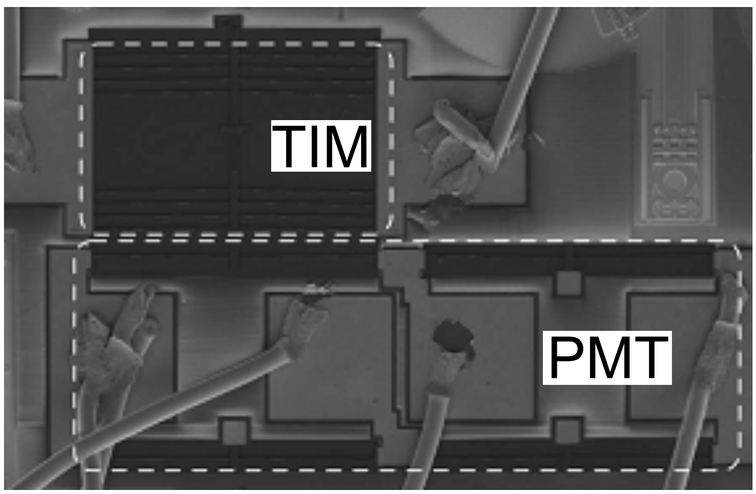

Figure 2.11: Using a piezoresistor to sense displacement in micro-actuators through a Wheatstone bridge configuration [11].

in which a change on strain produces a change in resistance. Unlike piezoresistors, the change in resistance in strain gauges is product of geometry changes rather than the material resistivity. This makes resistance gauges highly dependent on the direction of measurement and in temperature variations. An example of a strain gauge sensor is shown in **Figure** 2.12, where a MEMS-based structure with integrated mechanical amplifier is used [12]. Two parallel metal electrodes can also be used to measure displacement in micro-structures by measuring the change in capacitance as the gap or overlapping area between the plates changes. This method can be employed in double clamped structures due to its relatively

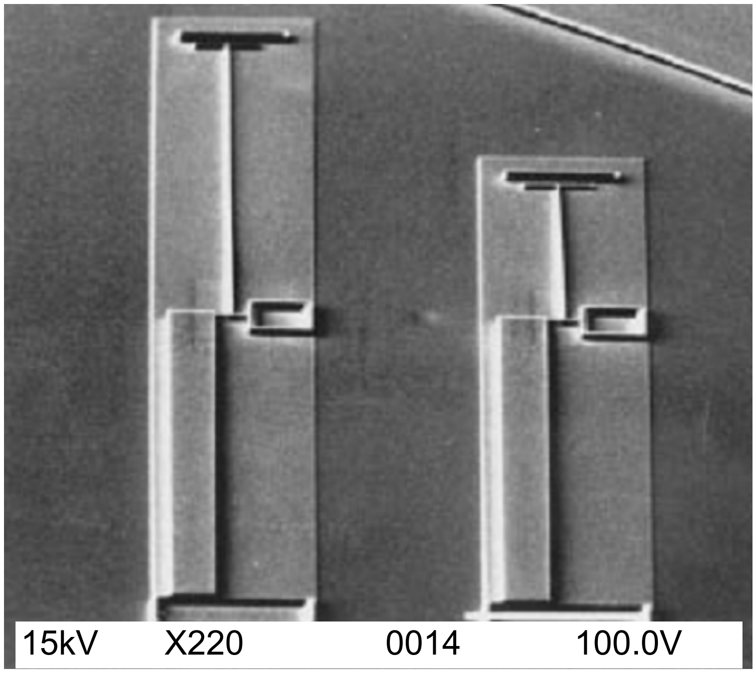

Figure 2.12: MEMS strain gauge sensor and mechanical amplifier [12].

high deflection sensitivity. One disadvantage of this method is that it is not compatible for micro-benders since the change in gap/area overlap is generally non-uniform and highly non-linear. **Figure** 2.13 shows an accurate displacement sensing mechanism based on overlapping area change [13].

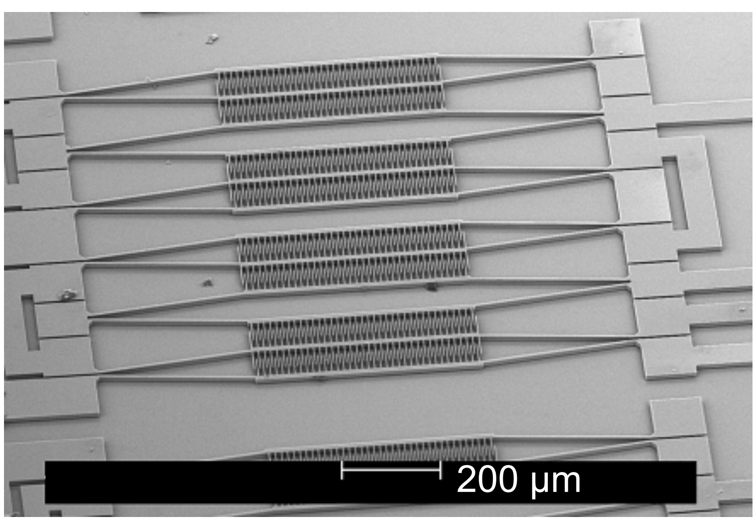

Figure 2.13: Parallel capacitive plates used as displacement sensing through change in overlapping area [13].

External sensors are less invasive mechanisms that generally allow for large displacement measurements. One of the most common external displacement measurement technique is laser scattering, where a laser is focused at the micro-actuator and the reflected light movements produced by the device displacement is measured with a position sensitive detector (PSD). **Figure** 2.14 shows a schematic representation of laser scattering used to measure displacements in micro-actuators [14]. One disadvantage of this method is its high sensitivity to external vibrations and correct position of the laser, which depends on the laser spot size. The use of an interferometer can generate even higher displacement sensitivity and precision

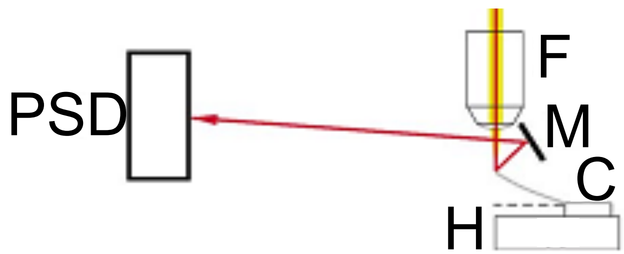

Figure 2.14: Schematic representation of a laser scattering technique for measuring displacements in micro-actuators [14].

at the expense of more complicated and expensive setups, with even higher disturbance sensitivity. A schematic of a interferometry setup is shown in **Figure** 2.15. The basic principle of an interferometer is to measure the phase change between two beams that travel through different path and that originate from the same coherent light. This creates an interference pattern that is highly sensitive to the displacement of the micro-actuators. An example of an interference pattern on a MEMS device created with a imaging interferometer is shown in **Figure** 2.16 [16]. This pattern can then be used to unwrap the measured phase image and detect height and slope of the micro-actuators.

In general, internal sensors complicate the fabrication of the MEMS devices, increase the fabrication cost and are usually inefficient in measuring large displacements. On the other hand, external sensors require the use of bulky and high cost measurement setups, which hinders the miniaturization of the device. Self-sensing is yet another method for measuring displacements, in which the deflection is estimated based on some other material parameter

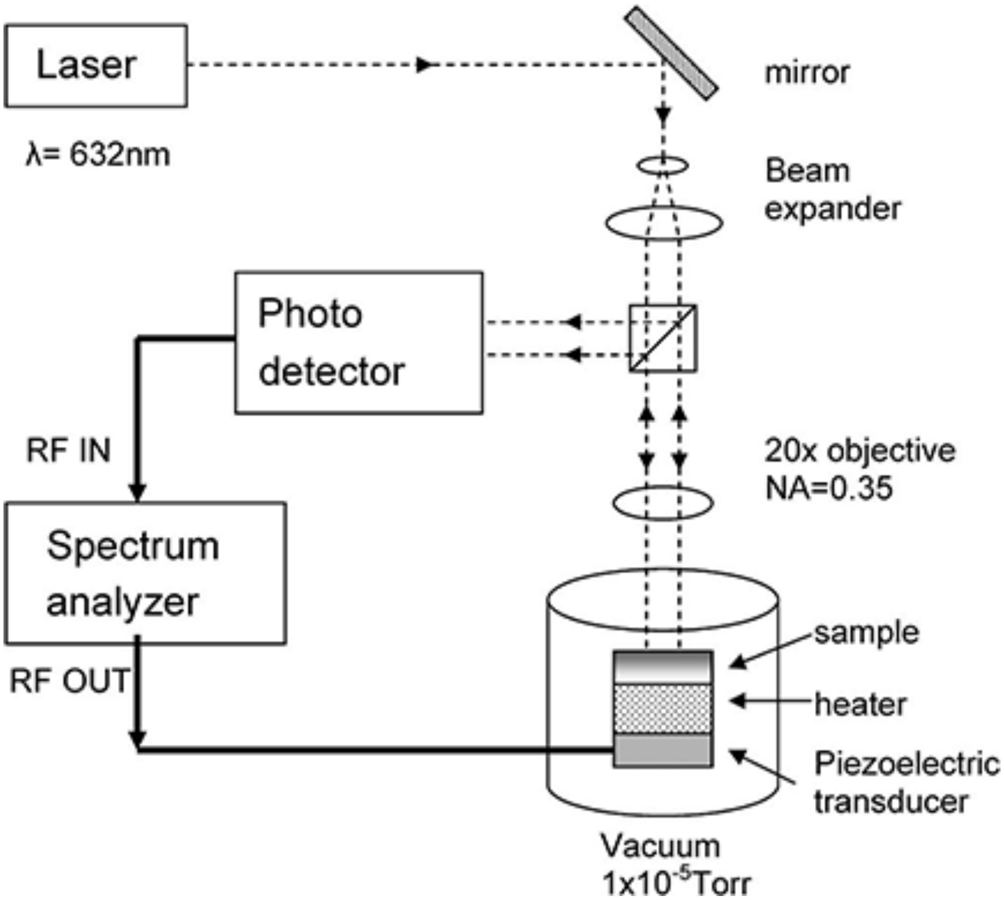

Figure 2.15: Schematic of a interferometer [15].

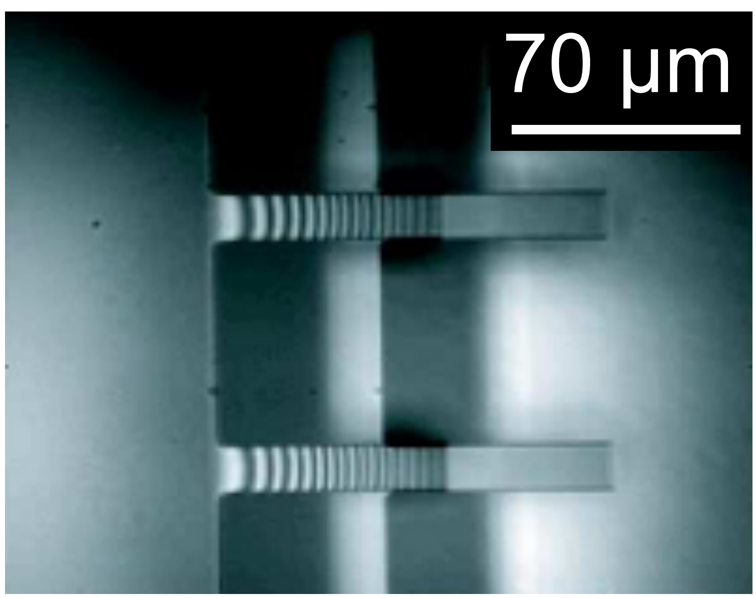

Figure 2.16: Interference pattern on a micro-actuator created with an imaging interferometer [16].

change, such as resistance or permittivity [17,46,47]. This method is particularly popular in smart material-based MEMS actuators, such as shape memory alloys (SMAs), piezoelectrics, and electroactive polymers, where usually more than one material parameter is sensitive to the actuation signal. A more detailed self-sensing background is presented in **Section 2.2.3**

2.2.2 Control Techniques

Many control techniques have been employed for accurate actuation of micro-devices, the most widely used being proportional-integral-derivative (PID) due to its simplicity and easy tunability of its parameters. Examples of PID controllers used in micro-actuation can be found in literature, particularly for linear and non-hysteretic actuators. In the work done in [48], a proportional controller is used to control the gap of a comb-drive micro-actuator to produce displacement parallel to the substrate (i.e. in-plane displacement). A maximum controlled displacement of 20 μm was achieved with input voltage of 100 V and a maximum operating frequency of 30 Hz. In [49], a RLC circuit is used to control the gap of a micro-actuator with a maximum gap range of 1.6 μm using position feedback. A maximum control voltage of 4 V was reported with operating frequencies of up to 90 Hz. Yet another example of PID control in micro-actuators is shown in [50], where a MEMS cantilever-based parallel plate (131 μm long with an initial gap of 1.9 μm) is controlled with a maximum voltage of 10 V.

PID compensators have also been used to accurately control the displacements in thermal actuators. The 800 μm long out-of-plane micro-actuator shown in [51] was controlled with a PID through a maximum deflection range of 15 μm with maximum power consumption of 698 mW. Another work, reported in-plane deflection control of a 200 μm long structure with maximum deflection and power of 10 μm and 90 mW [52].

For non-linear micro-actuators based on smart materials, more complicated compensator techniques are required. The research in this area is very limited due to the miniaturization difficulties imposed by smart materials. Non-linear sliding mode compensation was used in [53] to control the mechanical displacement in SMAs. Although the actuator is in the macro-scale, it serves to show the capabilities of this type of control for achieving SMA-based positioning. Fuzzy logic and robust controllers have also been used to control micro-actuators, especially whenever system uncertainty is present [54, 55]. In [55], a robust compensator was used to control an Ionic PolymerâĂŞMetal Composite — a type of EAP — actuator. The device length was 39 mm with a maximum deflection of 0.3 mm.

Hysteretic micro-actuators require even more complicated control approaches, which usually involve some type of hysteresis compensation, such as Preisach and PrandtlâĂŞIshlinskii inverse. The SMA actuator in [56] was controlled using a Preisach hysteresis inverse in combination with a PID controller. The 2 mm long actuator achieved a maximum deflection of 180 µm and a closed-loop response time of around 25 ms. Another example of hysteresis compensation is shown in the work done in [57], where a Prandtl-Ishlinskii inverse model was used as the hysteresis compensation and a PID was used to control the system dynamics. A different hysteresis compensation technique is achieved by using self-sensing feedback, which can be used in combination with PID or robust controllers for accurate positioning control in micro-actuators.

2.2.3 Self-sensing Feedback

Self-sensing, in micro-actuators, refers to the estimation of a mechanical parameter (such as displacement or strain) based on the measurements of another coupled parameter (such as resistance or permittivity) of the same material that exerts the actuation. In other words, the actuation or active material is also used as the sensing element, which greatly reduces the measurement setup and signal processing. Self-sensing has been used effectively in multiple studies as a mechanism for achieving closed-loop control of mechanical displacements in micro-structures [46, 58–60]. For example, self-sensing of lead zirconate titanate (PZT)-based microactuators has been used to effectively control the vibrations of the device for hard disk drives [59]. By measuring the PZT voltage, which is modeled through a capacitor decoupled in a bridge circuit, the deflection of the PZT-based microactuator can be estimated and controlled.

Thermal expansion-based deflection of a microactuator comprising layers of two different materials has also been estimated using the resistance change of one of the materials and the monotonic coupled changes in the structural deflection as the temperature is varied [46]. A micro-structure composed of layers of two different materials was heated, causing both materials to expand at different rates; producing monotonic coupled changes in materialâĂŹs resistance and structureâĂŹs deflection. Shape memory alloys (SMAs)-based micro-grippers have taken advantage of self-sensing by approximating and controlling their strain/deflection using contraction force-to-resistance polynomial models [60]. Although the operation of SMAs is similar to that of thermal expansion, their response is highly hysteretic [19], which makes resistance-to-deflection modeling more challenging and produces relatively large errors (higher than 5 %) between the achieved and desired deflections in tracking-control experiments (see **Figure** 2.17) [17]. These large errors in hysteretic micro-actuators, like VO_2-based actuators, are undesirable and could be detrimental in applications such as micro-manipulation [61, 62], micro-optics [63], and micro-sorting [64], where highly precise control is required.

Inverse compensation has been used to reduce the impact of strong hysteresis non-linearity in smart material actuators [18, 65–68]. **Figure** 2.18 shows the effects of hysteresis compensation in a piezoelectric micro-actuator in terms of measured and desired displacement values. By using hysteresis compensation it is possible to reduce the hysteresis, which reduces the tracking errors. Although this technique is effective, it is also highly computationally demanding and does not perform robustly against disturbances. Control theory has been used in systems based on self-sensing to reduce environmental disturbances and plant uncertainties, but such studies have been typically limited to piezoelectric-based actuators [69–72]. The controllers in [69, 70] were designed to control the deflection of piezoelectric microactuators based on charge measurements. Although external disturbances and model

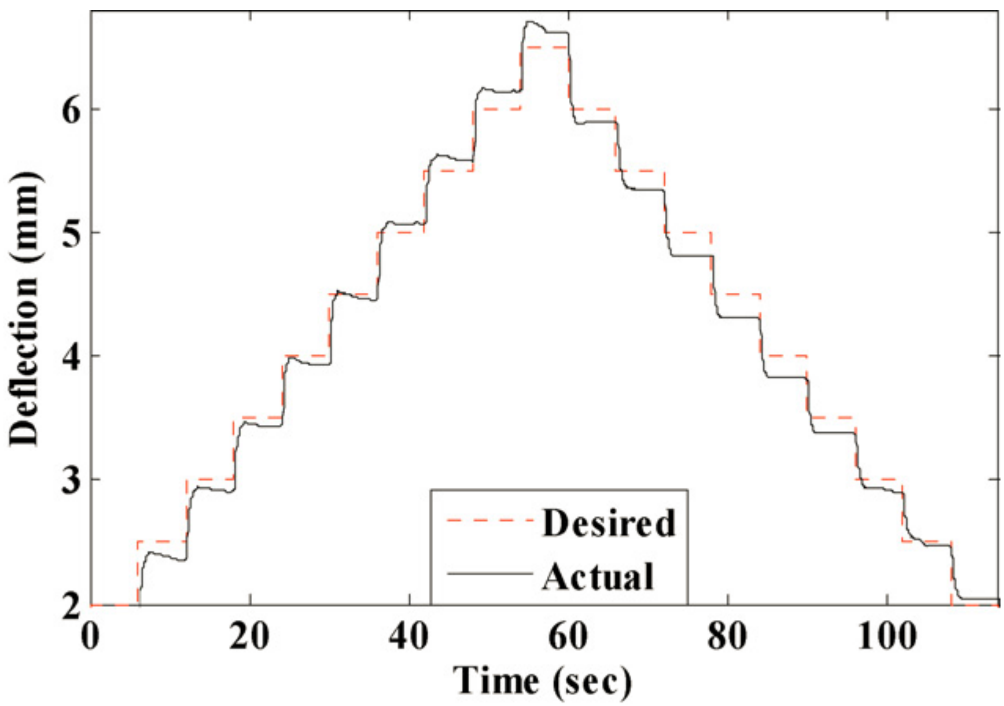

Figure 2.17: Closed-loop step reference response of a SMA micro-actuator using self-sensing feedback without hysteresis compensation [17].

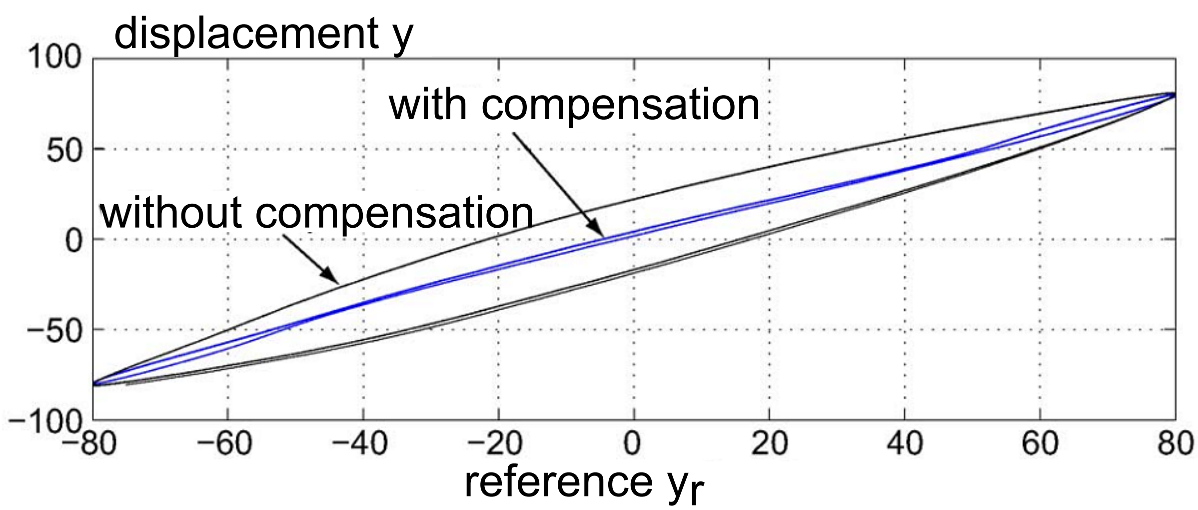

Figure 2.18: Actual displacement as a function of reference for a hysteresis uncompensated and compensated micro-actuator using hysteresis inverse [18].

uncertainties were considered for the controller designs, the error between the actual deflection and the reference error was not addressed. The robust controllers in [71, 72] were synthesized for suppression of piezoelectric structure vibrations by self-sensing the rate of strain change, where tracking desired reference signals was not considered. The work done in [71] followed a similar control framework as in [69], but it was designed to follow a desired deflection value of zero (in order to reduce vibrations). Although the controller design in [72] accommodates constraints on control effort, it does not account for effects of model uncertainties, hysteresis or disturbances. Hysteresis compensation has also been achieved in self-sensing feedback systems through external manipulation [73], or by limiting the actuation range of the device [74]. Recently, more interest has been given to accurate control of VO_2 micro-actuators due to its high strain energy density and miniaturization capability. Since highly coupled parameters from multiple domains change across the material transition, it is possible to reduce or even cancel out the hysteresis between mechanical deflection and electrical resistance.

2.3 Vanadium Dioxide

VO_2 is a stable vanadium oxide phase known to undergo abrupt changes in its electrical [20], mechanical [14], and optical [21] properties during its solid-to-solid phase transition. This transition can be induced thermally at a transition temperature (T_{Tr}) of approximately 68 °C, during which the material changes from its monoclinic crystalline structure (M_1) at room temperature, to a tetragonal, rutile-type (R) at higher temperatures. The transition is fully reversible when deposited as thin films. The schematic representation of unit cells for both VO_2 phases are shown in **Figure** 2.19.

Although other vanadium oxides also exhibit phase transitions, their T_{Tr} are much further from room temperature than VO_2 (e.g. V_6O_{13} [75] and V_2O_3 [76] show phase transitions at $T_{Tr} = -123\,°C$, and V_2O_5 [77] at $T_{Tr} = 280\,°C$). The proximity of the T_{Tr} to room temperature has given VO_2 the upper hand when it comes to most practical applications. Defects in the VO_2 lattice may generate room-temperature phases different than the typical monoclinic M_1 phase of pure VO_2, which has an influence on the magnitude of the changes of the materialsâĂŹ properties and on T_{Tr}. Such defects can be induced through substitutional vanadium ions (V^{5+} for V^{4+}), or via doping by Cr, Ti, W, Fe, among other elements [78–81].

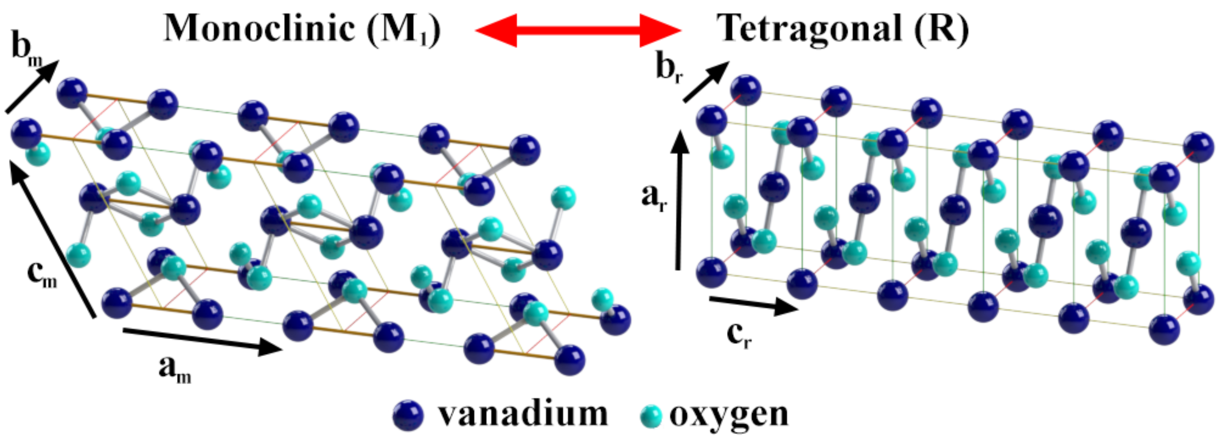

Figure 2.19: Schematic representation of the units cells in the M_1 and R VO_2 phases. Note the orientation change from one phase to the other.

The physics that produce the drastic changes in VO_2 properties is still a subject of debate in the scientific community, although recent work has revealed that the behavior can be described as a Mott-Peierls transition [82]. During this transition, two different mechanisms occur: the insulator-to-metal transition (IMT), responsible for the electrical resistance change [20], and the structural phase transition (SPT) [22], responsible for the large strain produced as a consequence of the lattice reorganization. These two mechanisms are strongly coupled — the reordering of the vanadium ions that causes a reduction in the bandgap comes with a change in the crystal structure that causes strain in a highly oriented film. These two mechanisms have been used in the development of a variety of applications, such as thermo-optical modulators [83], optical switched [84], uncooled micro-bolometers [85], thermochromic smart windows [86], field effect transistors [87] among other applications.

VO_2 can be deposited using Pulsed Laser Deposition (PLD) [14], Sputtering [88], and Sol-Gel [89], among other techniques, and usually involve temperatures above 300 °C in an oxygen atmosphere and/or a post-annealing step. PLD is the deposition technique employed to deposit all the poly-crystalline VO_2 thin-films used in this thesis.

2.3.1 Electrical Transition

The effects produced by the IMT in VO_2 was explained more than four decades ago in [90] and more recently in [91]. In the tetragonal (rutile) structure at high temperatures, the oxygen (O) atoms surround the vanadium (V) atoms in an octahedral configuration. This configuration results in O sharing through the edge of the octahedral along the c_r axis (shown in **Figure** 2.19). The V ions in the d levels are divided into t_{2g} states, which are then divided into d_{ll} and π^*, and e_g states, which have higher energy. The d_{ll} produce V-V strong bonding pairs along the c_r direction resulting in a metallic bond, which produces the metallic or low resistance values at high temperatures. As the temperature is decreased through T_{Tr}, the V-V pairs tilt and V-O bonds are formed resulting in the monoclinic structure and an increase in the energy of the π^* states. During this change in lattice, the d_{ll} band is divided into two regions: a bonding combination with low energy and a anti-bonding combination with high energy. This results in a bandgap of 0.7 eV, which explains the increase in resistance at lower temperatures. The change in the bands diagrams can be seen in the schematics shown in **Figure** 2.20.

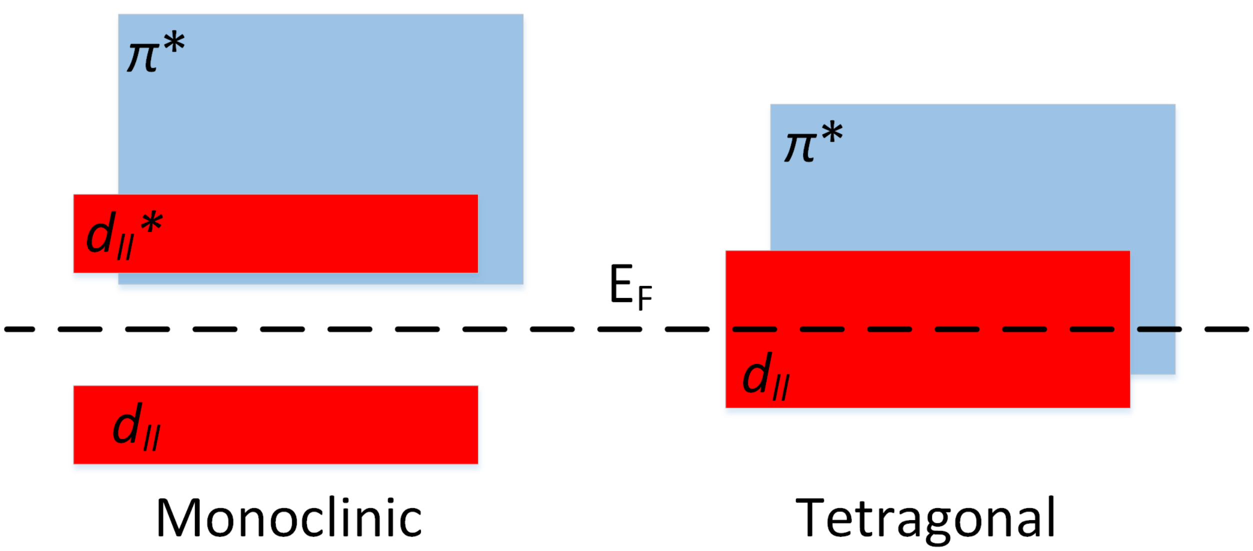

Figure 2.20: Band diagram representation of the tetragonal and monoclinic phases in VO_2.

2.3.2 Structural Transition

The electrical transition in VO_2 is immediately followed by a SPT, which requires a slightly higher energy level [27]. During this SPT, the VO_2 crystalline structure contracts in the c_r direction while it expands in the a_r and b_r directions [91]. The abrupt effects produced by the SPT were not discovered until the last decade, when it was reported that a VO_2-coated 350 µm-long single crystal silicon (SCS) cantilever produced curvature changes of over $2000\,\mathrm{m}^{-1}$ when heated across T_{Tr} [14]. The observed changes were not due to the difference in thermal expansion coefficients between the SCS and VO_2, since the measured strain was 0.3 %, which is much larger than that produced with thermal expansion alone. Instead, the curvature changes were a result of the changes produced by the SPT. VO_2 tends to orient itself with its c_r axis parallel to the substrate when deposited by PLD over amorphous Si and SiO_2. As a result, when the c_r axis contracts it produces the observed behavior. Following this discovery, the study of the SPT has resurfaced. Other studies in bimorph structures have been recently performed, which include more curvature studies [23], mechanical resonance changes [92], and stress measurements [93]. This investigations have prompt the development of new technologies involving the SPT of VO_2.

2.3.3 Vanadium Dioxide Actuators

Since the development of the first VO_2-based micro-actuators [14], there have been other types of VO_2-based structures and improvements. In [23] a VO_2-coated Cr cantilever was used to achieve curvature changes of $24\,000\,\mathrm{m}^{-1}$ through the SPT. This was possible due to device optimization and smaller device thicknesses. Photo-thermal experiments were performed on VO_2-based micro-actuators to show fast actuation of the devices in different surrounding media [24, 28]. The results showed that not only can the VO_2 be actuated thermally with laser light, but it can also reach actuation bandwidth much higher than conduction heating actuation. A method for obtaining more precise strain energy density values in large bending devices was used in VO_2-coated Si micro-actuators. The strain energy density is the figure of merit in micro-actuation since it normalizes the work performed with device volume. A value of $8 \times 10^5\,\mathrm{J\,m^{-3}}$ was obtained, which is comparable to that found in SMA-based actuators.

More experiments in VO_2 micro-actuators were performed to achieve deflection hysteresis modeling through the use of Preisach operators [26]. By measuring the curvature change of a VO_2-coated silicon cantilever across the SPT it was possible to find a hysteresis model that could fit the curvature-temperature relationship. This was then used to significantly reduce the hysteresis and perform open-loop actuation of the device. Additional control experiments were performed in [29], where self-sensing feedback was used to control the deflection of a VO_2-coated Si cantilever. This served as the proof of concept of hysteresis reduction in VO_2 using self-sensing and the basis for the work performed in this document. Further integration of VO_2 into MEMS-based micro-actuation was achieved by incorporating localized heating elements inside the structure in order to decrease power consumption, increase bandwidth, and decrease device size [25]. Using this MEMS devices it was also possible to exploit the hysteresis in deflection in order to develop programmable mechanical states [94]. In addition, a closed-loop system for controlling device level temperature was developed in order to compensate for temperature variations in the environment.

All of these results suggest that VO_2-based micro-actuators can achieve better performance than other thermal actuators (such as those based on SMAs) in terms of power consumption, bandwidth, strain energy density, and repeatability. Some of these studies, including photo-thermal actuation, strain energy density calculations, and the proof of concept of self-sensing feedback in VO_2-coated structures, were performed towards the development of this thesis. Their results are explained in detail in **Chapter 3**.

2.4 Summary

In this chapter, a comprehensive background on micro-actuator mechanisms, feedback control in micro-actuators and VO_2 was presented. The discussion on micro-actuators included the most common mechanisms, such as thermal, electrostatic, and smart materials-based actuators. The use of feedback control techniques in the different actuation mechanisms was divided into types of deflection sensors, compensation schemes with emphasize on self-sensing feedback and hysteresis compensation. Lastly, the VO_2 electrical and structural phase transition mechanisms were explained, and an overview of VO_2-based actuators was given. It was shown that VO_2 micro-actuators can achieve better performance than other types of thermal actuators with strain energy densities greater than other technologies and comparable to that from SMAs. The following chapters are aimed at studying and exploiting the capabilities of VO_2 in order to design, fabricate, characterize and control a MEMS micro-actuator with integrated localized heaters and self-sensing mechanism using the IMT and SPT of the VO_2.

CHAPTER 3

VANADIUM DIOXIDE AS A SMART MATERIAL

In this chapter a series of experiments are developed in order to test the mechanical capabilities and limits of the material: 1) Quasi-static thermal actuation using conduction heating is used to determine maximum deflection range, transition temperature and hysteresis characteristics; 2) Strain and stress calculations using experimentally measured curvature changes are also used to obtain the strain energy density of VO_2 micro-actuators; 3) Photo-thermal actuation is used to determine frequency response, limiting mechanisms and repeatability in VO_2 micro-actuators; 4) Self-sensing feedback is achieved by estimating deflection of a VO_2 micro-actuator using resistance measurements from a separate substrate. Experiments 1 and 2 were performed using the same VO_2 micro-actuator and measurement setup, while 3 and 4 were performed using different VO_2 depositions and experimental procedures. All the SCS micro-cantilevers used were supplied by the same manufacturer (MikroMasch). The VO_2 depositions were all performed using very similar PLD recipes except for experiment 3 in which the V target was doped with a low concentration of Cr. More detailed descriptions of VO_2 depositions, measurement setups, and other experimental procedures can be found in [28, 29, 31].

3.1 Quasi-static Actuation

The VO_2 used in this experiment was deposited on a SCS microcantilever with length, width and thickness of 300 µm, 35 µm and 1 µm, respectively. The deposition was performed in a vacuum chamber at a pressure of 20 mTorr with a background pressure of approximately 10^{-6} Torr. An oxygen and argon atmosphere was maintained with gas flows of 15 and 10 standard cubic centimeter per minute (sccm), respectively. Although the sample temperature was not directly measured throughout the deposition time of 30 min, a substrate-to-controller temperature calibration was conducted before the deposition. From this calibration, the approximate substrate deposition temperature was approximately 550 °C. A krypton fluoride excimer laser (Lambda Physik LPX 200, $\lambda = 248$ nm) was focused on a rotating vanadium target with an intensity of 350 mJ at a repetition rate of 10 pulses per second. The sample was positioned 12.7 mm away from the heater and facing the target at a distance of 63.5 mm. The sample was constantly rotated through the deposition in order to ensure a uniform temperature and thickness distribution. The thickness of the VO_2 layer was 172 nm, as measured by a profilometer on a Si test substrate to which the sample was attached during deposition. **Figure** 3.1 shows the micro-actuator cross-section after the VO_2 deposition and the scanning electron microscopy (SEM) photo of the device.

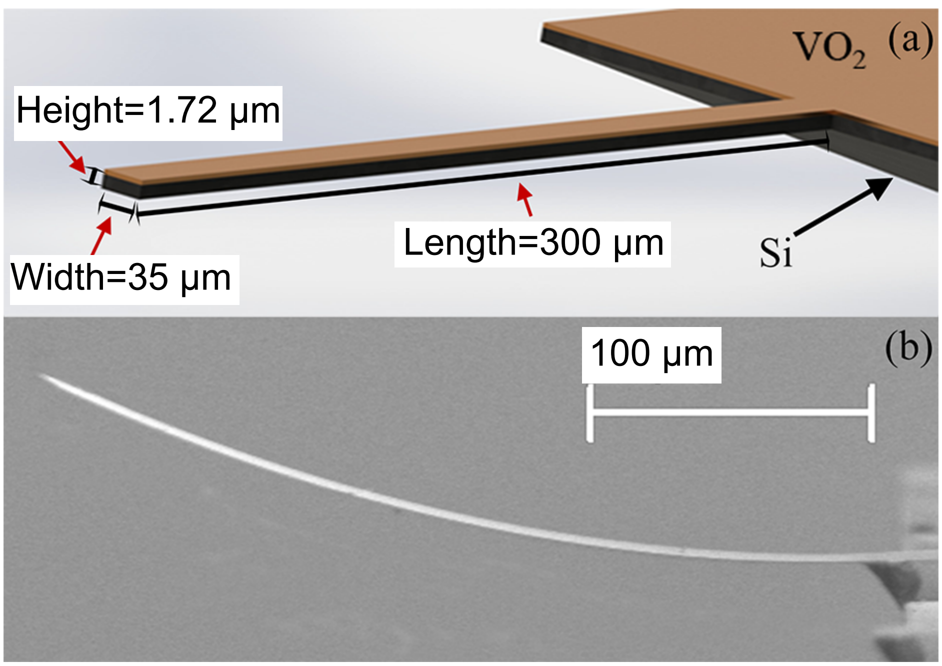

Figure 3.1: Micro-actuator device diagram after VO_2 deposition in microcantilever (a) and SEM picture of the finalized device (b). The height in the diagram corresponds to the total thickness of the silicon and the VO_2 layers. The observed post-deposition bending is due to the residual film stress.

The test substrate, which also contained VO_2, was used for electrical resistance characterization purposes. The test piece was placed on top of a Peltier heater in a 4-point probe (Signatone, $S-301-4$) and two of its electrical terminals were connected to a multimeter

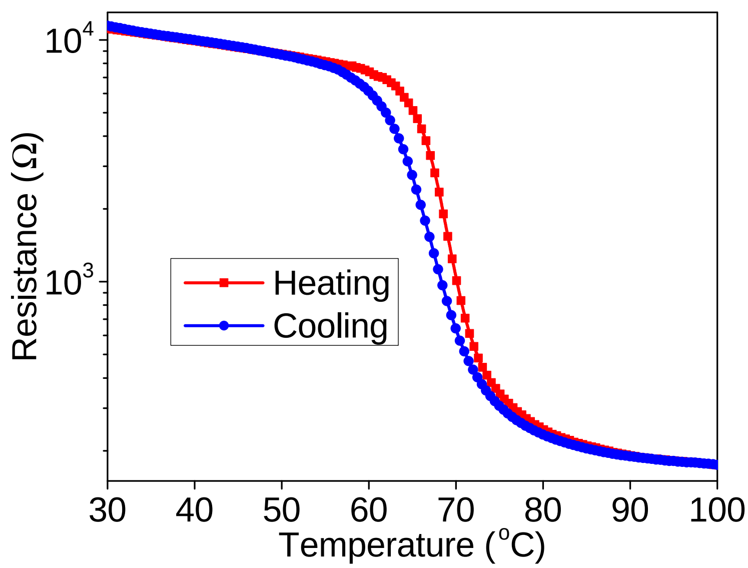

Figure 3.2: Resistance as a function of temperature of the VO_2 thin film deposited on (100) silicon.

(Keithley, 2400). The temperature of the heater was measured with a monolithic integrated circuit temperature transducer (AD592) and controlled in closed-loop with a benchtop temperature controller (Thorlabs, TED4015). **Figure** 3.2 shows the VO_2 film resistance as a function of temperature through a heating-cooling cycle from 30 to 100 °C in steps of 0.5 °C. For each setpoint, the measurements were performed after 4 s of reaching steady-state temperature value. This hold time value was empirically found to be optimal in the trade-off between temperature settling time and experiment duration. The same hold time was used for all the experiments presented here. A transition temperature of approximately 68 °C can be noticed. The curve follows the abrupt drop in resistance and exhibits pronounced hysteretic behavior as observed in previous work for VO_2 deposited on (100)-oriented SCS structures [95].

The VO_2 thin film was also characterized by its structural change across the phase transition. The inset picture in **Figure** 3.3 is a superimposed scanning electron microscopy (SEM) photo of the VO_2-coated SCS cantilever at 30 and 100 °C, which shows the characteristic large deflections of the bi-layered structure due to the phase transition [14, 95, 96]. **Section 2.3.2** presents a detailed explanation of the thermal mechanisms that drive the micro-actuator.

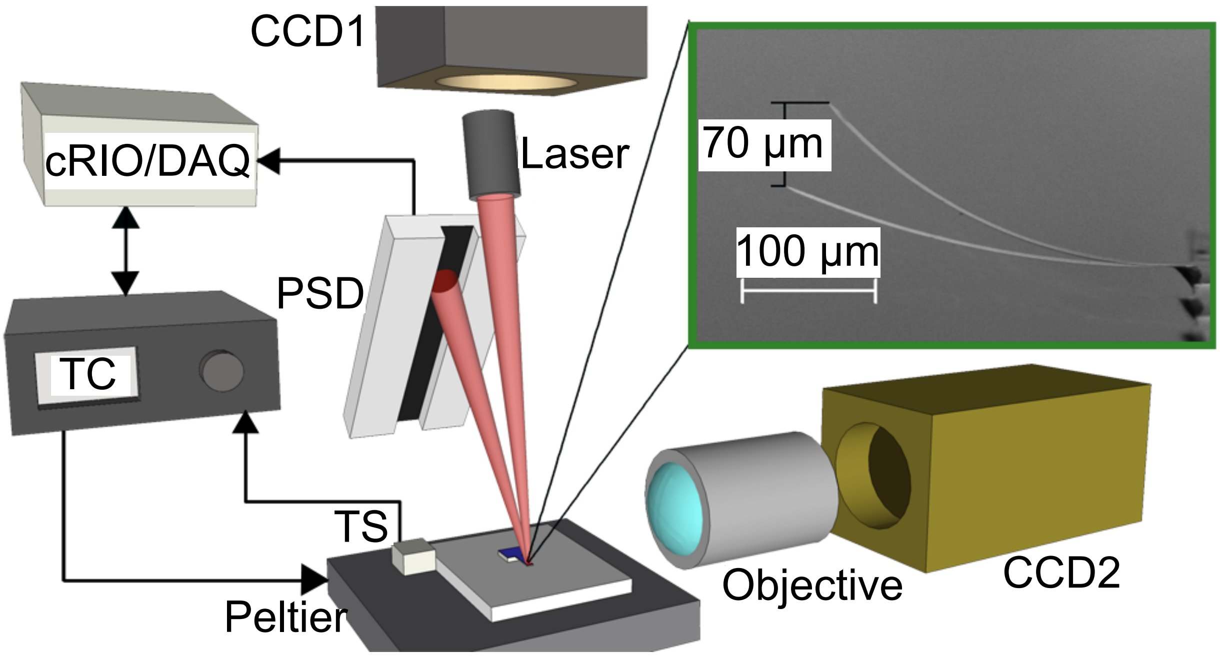

Figure 3.3: Setup used for the temperature-dependent micro-actuator tip displacement measurements. The inset is an SEM picture of the micro-actuator sideview, which shows large tip displacements under temperature change.

The VO_2-coated Si micro-actuator was placed in the setup shown in **Figure** 3.3 in order to measure its tip deflection change through heating-cooling cycles between 21 °C and 84 °C. The micro-actuator chip was glued with a highly thermally conductive silver paint to a silicon substrate which was then placed on a Peltier heater. The silicon substrateâĂŹs only purpose was to hold the micro-actuator chip during the experiments. The temperature of the heater was controlled in closed loop using the same benchtop temperature controller (TC) and sensor (TS) used for the resistance measurements in **Figure** 3.2. The cantilever deflection was measured by using the reflection of an infra-red (IR) laser ($\lambda = 808$ nm, rated at a maximum of 20 mW) aimed at the tip of the micro-actuator. The reflected light beam was then focused to the active area of a one-dimensional position sensitive detector (PSD, Hamamatsu S3270). The intensity of the sensing IR laser was kept at the minimum possible for reducing laser self-heating while maximizing the signal to noise ratio. The bending of the bilayer micro-actuator was monitored by the displacement of the sensing IR laser beam incident on the PSD, which changed its output voltage. The PSD voltage was measured by an embedded real-time controller (NI cRIO 9075) with an analog input module (NI 9201). For alignment purposes, two charge-coupled device (CCD) cameras were used; one of them provided top view alignment of the sensing laser (CCD1) while the other provided a side view of the micro-actuator (CCD2) through an objective lens that magnified the image. Images obtained from the micro-actuator sideview were used to calibrate the output voltage from the PSD into micro-actuator tip deflection. A LabView program was developed to automatize the tip deflection measurements of the bilayer micro-actuator as a function of temperature. In this program, an arbitrary temperature sequence could be programmed into the cRIO controller. The cRIO acted as a supervisory controller, which communicated the temperature setpoint from the input sequence to the temperature controller while monitoring the tip deflection change and the sensor temperature.

The measured tip displacement of the microcantilever was used to calculate the curvature (κ) from the transcendental equation given by

$$\Delta z = \frac{2}{\kappa} sin^2 \left(\frac{\kappa L}{2} \right), \tag{3.1}$$

where Δz is the tip deflection change and L is the length of the micro-actuator. Since the micro-actuator in this work showed large initial deflection (see inset in **Figure** 3.3), this Δz corresponds to the deflection change relative to the initial deflection at room temperature. The initial value measured was 67 µm. **Figure** 3.4 shows the curvature change (relative to the initial curvature) as a function of temperature in steps of 0.5 °C, calculated from **Equation** (3.1). A maximum curvature change of approximately $1800\,\mathrm{m}^{-1}$ was observed through the VO_2 phase transition.

The curvature change follows a non-monotonic behavior as a function of temperature, which is briefly explained. The thermal expansion coefficient of Si at room temperature ($2.6 \times 10^{-6}\,\mathrm{K}^{-1}$) [97] is smaller than the average coefficient of VO_2 ($5.7 \times 10^{-6}\,\mathrm{K}^{-1}$) [98], meaning that for increasing temperatures, the change in curvature due to differential thermal expansion will be negative and linear. This is what is observed in **Figure** 3.4 for temperatures

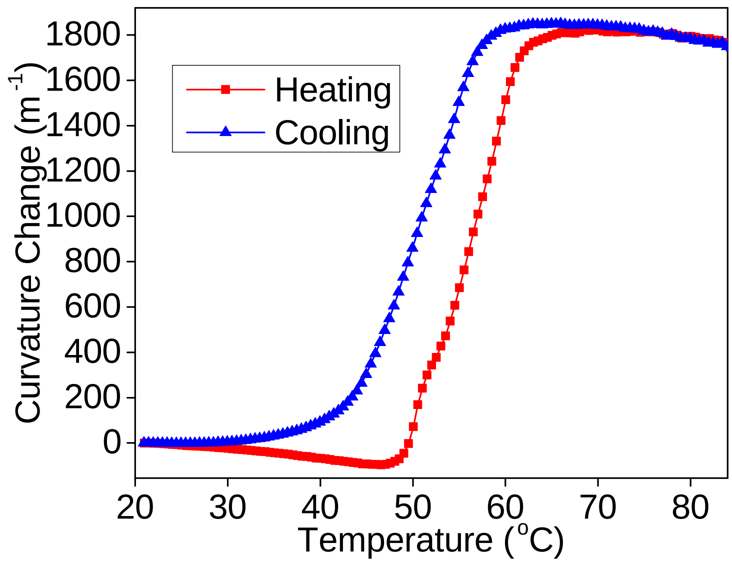

Figure 3.4: Experimental measurement of micro-actuator curvature change as a function of temperature through a complete heating and cooling cycle (21 °C — 84 °C).

less than 30 °C and above 70 °C. However, as the temperature increases into the transition region, the VO_2 crystallographic plane parallel to the surface of the SCS cantilever shrinks, producing a compressive stress that bends the cantilever upward (positive curvature change) [14]. Thus, the observed curvature change is produced by two competing mechanisms: 1) the differential thermal expansion from both materials (dominant mechanism outside the phase transition) and 2) the abrupt built up of compressive stress produced by the VO_2 layer as the material undergoes its phase transition (dominant mechanism during the phase transition). This process is fully reversible as will be shown in **Section 3.3**.

3.2 Strain Energy Density

In order to find the stress and strain produced by the micro-actuator due to the phase transition of the VO_2, including the effect of the thermal expansion between the two layers, the following mathematical treatment was employed. The relationship between the bilayer micro-actuator curvature and strain is given by [99]

$$\varepsilon_T = \frac{E_f^2 H_f^4 + E_s^2 H_s^4 + 2E_f E_s H_f H_s \left(2H_f^2 + 2H_s^4 + 3H_f H_s\right)}{6E_f E_s H_f H_s \left(H_f + H_s\right)} \kappa, \tag{3.2}$$

where the subscripts f and s are for the film and substrate parameters, respectively, E is the biaxial modulus, H is the thickness, and ε_T is the thermal strain. For the particular case of the VO_2 micro-actuator studied here, the total thermal strain is defined as the sum of the strains produced by: 1) the difference in thermal expansion coefficients from the two layers and 2) a hysteretic nonlinear term that represents the strain generated by the phase transition of the VO_2 layer. Since the thickness of the two layers are known, ε_T can be calculated from **Equation** (3.2) for every temperature value, by assuming the silicon biaxial modulus in the (100) direction, $E_s = 180.5\,\text{GPa}$ [100] and the biaxial modulus of VO_2, $E_f = 156\,\text{GPa}$. Although the used value for VO_2 is an average of the values found in literature [101–103], an error of up to 10 % was taken into consideration in all calculations. The strain change of the micro-actuator throughout the major heating-cooling loop is shown in **Figure** 3.5. A total strain change of −0.32 % (where the negative denotes compression) was obtained with a strain change rate of −0.022 %/°C through the VO_2 transition, which is in accordance with the previously obtained results [14]. A maximum error of ±2.6 % was obtained with the deviation of the VO_2 biaxial modulus. This strain change produces an axial thermal stress (σ_T), which can be calculated from [99]

$$\sigma_T = \frac{E_f E_s \left(H_f + H_s\right) \left(E_s H_s^2 \left(3H_f + H_s\right) + E_f H_f^2 \left(H_f + 3H_s\right)\right)}{E_f^2 H_f^4 + E_s^2 H_s^4 + 2E_f E_s H_f H_s \left(2H_f^2 + 2H_s^4 + 3H_f H_s\right)} \varepsilon, \tag{3.3}$$

Figure 3.5 also shows the thermal stress change as a function of temperature for the same major heating-cooling loop. A maximum error of ±0.2 % is obtained when considering the VO_2 biaxial modulus variations. A recoverable stress of −510 MPa was obtained from the results of **Equation** (3.3) (stress change rate of $-36\,\text{MPa}\,°\text{C}^{-1}$ through the materialâĂŹs transition), which is higher than the −379 MPa obtained by wafer curvature measurements of VO_2 deposited on Si reported by Viswanath, et al. [93]. In another work, the stress

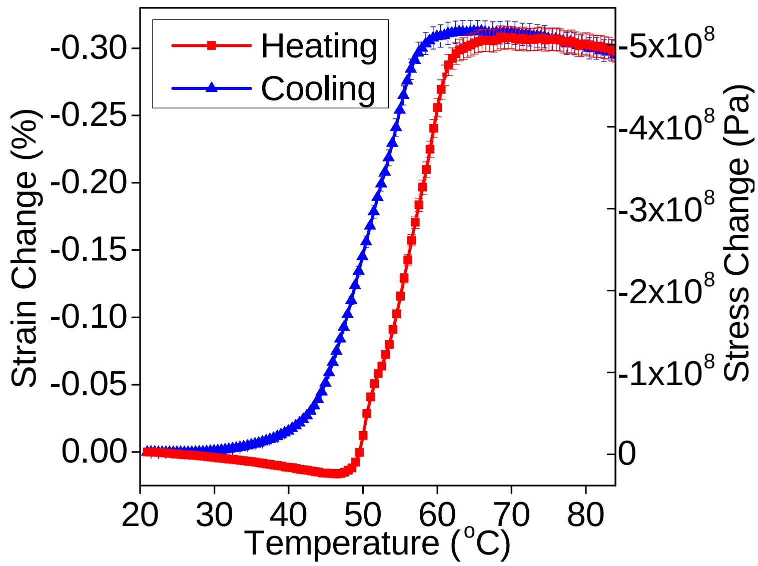

Figure 3.5: Micro-actuator strain and stress change as a function of temperature through the complete heating and cooling cycle (21 °C — 84 °C). The error bars (±2.6 %) correspond to the strain error due to the uncertainty of the biaxial modulus of the VO_2 layer. The error produced on the stress values is much less (±0.2 %) and is not shown for clarity.

produced by the materialâĂŹs transition was estimated from cantilever curvature changes using a modified version of StoneyâĂŹs equation [14]. A value of approximately 1 GPa was estimated, which is about twice the value reported here. However, since the StoneyâĂŹs equation used to estimate this value assumes infinitesimal deflection (small angle approximation) the 1 GPa value is likely to be an overestimate of the real value. Hence, the analytical study presented in this thesis is believed to result in a more accurate representation of the reversible stress produced in VO_2-coated silicon micro-actuator.

The strain energy density (W) of a bilayer micro-actuator made of isotropic materials is defined by [104]

$$W = \frac{1}{2}\varepsilon_T \sigma_T, \tag{3.4}$$

where ε_T and σ_T are the produced stress and strain, respectively. For the case of the micro-actuator presented in this thesis, the stress and strain values were those obtained from **Equation** (3.2) and **Equation** (3.3) for each of the temperature values measured. After substituting **Equation** (3.2) and **Equation** (3.3) on **Equation** (3.4) the strain energy density can be expressed in terms of the curvature, biaxial elastic moduli, and thicknesses:

$$
\begin{aligned}
W = {} & (E_f^2 H_f^4 + E_s^2 H_s^4 + 2E_f E_s H_f H_s (2H_f^2 + 2H_s^4 + 3H_f H_s) \\
& \times \frac{E_s H_s^2((3H_f + H_s) + E_f H_f^2 (H_f + 3H_s))}{72 E_f E_s H_f^2 H_s^2 (H_f + H_s)} \kappa^2.
\end{aligned} \tag{3.5}
$$

Figure 3.6 shows the strain energy density induced by the device through the major heating-cooling loop calculated from **Equation** (3.5). A strain energy density change of approximately $8.1 \times 10^5\,\mathrm{J\,m^{-3}}$ was produced by the VO_2-based micro-actuator with a maximum deviation error of $\pm 2.4\,\%$ (due to the VO_2 biaxial modulus uncertainty) through a temperature window of only $15\,°\mathrm{C}$. The strain energy density change rate throughout the transition is constantly increasing due to the squared curvature term in **Equation** (3.5). As the phase transition ends, the difference in thermal expansion coefficient between the VO_2 and the SCS begins to become the dominant actuation mechanism, and the energy density change rate begins to decrease, also following a parabolic behavior.

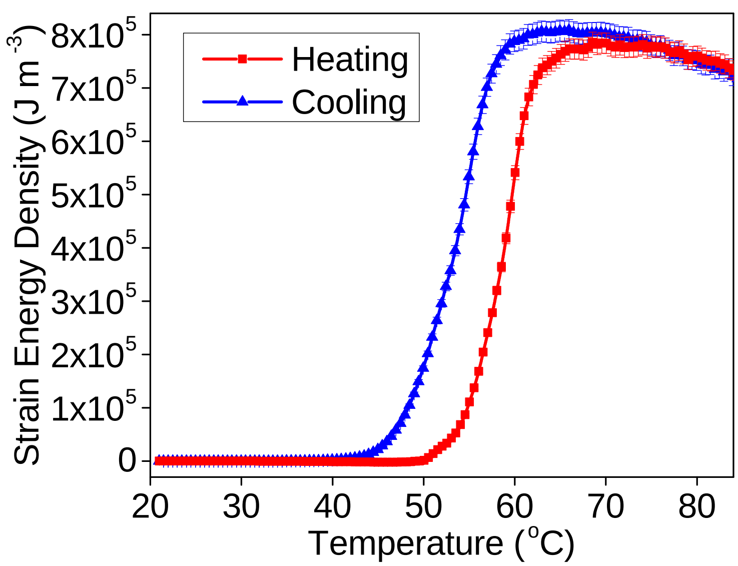

Figure 3.6: Micro-actuator strain energy density as a function of temperature through the complete heating and cooling cycle ($21\,°\mathrm{C}$ — $84\,°\mathrm{C}$). The error bars represent the ($\pm 2.4\,\%$) error due to the uncertainty of the biaxial modulus of the VO_2.

Krulevitch, et al., compared the strain energy density of various types of micro-actuators [19], all of which are shown in **Figure** 3.7 along with that of VO_2-based micro-actuator studied in this thesis. The strain energy density values are calculated from the product of stress and strain divided by two (according to **Equation** (3.4)). Although the VO_2-based micro-actuator does not have the highest value, it encompasses some other advantages. Firstly, the phase transition of the VO_2 transition is fully reversible, (which means that the micro-actuator will return to its original state after a complete actuation cycle), and they have been operated hundreds of thousands of cycles without showing degradation in the amplitude of deflection. In comparison, SMAs are not fully reversible and start fatiguing after less than a hundred cycles [19]. This means that the strain energy density of the SMA micro-actuator decays rapidly as the number of cycles increases. Secondly, VO_2-based micro-actuators are simple structures, easy and relatively inexpensive to fabricate, with demonstrated photo-thermal responses of fractions of milliseconds [96]. The fabrication of thermo-pneumatic micro-actuators is a very complicated process and its actuation usually involves very high temperatures (around 300 °C) and slow transients (in the range of seconds) [105]. Solid-liquid phase transition based micro-actuators are also complicated structures and are mainly used for micro-fluidic applications, making difficult a fair technological comparison [106]. Finally, the reported strain energy density measured for VO_2-based micro-cantilevers in this thesis is produced by a temperature difference of only 15 °C, whereas thermal expansion-based cantilevers require large temperature variations (> 200 °C) in order produce a strain energy density comparable to that of VO_2-based cantilevers [107].

In order to validate the calculated values from **Equation** (3.5) a numerical simulation was performed using the solid mechanics module from the finite element analysis software, COMSOL Multiphysics. The thermal expansion and phase transition effects were considered in the model as to replicate the experimental procedure and find agreement between theory, experiment and model. The simulated geometry consisted of a bilayer cantilever with length, width and thicknesses corresponding to the ones previously discussed. The material parameters used — YoungâĂŹs moduli, coefficients of thermal expansion, and PoissonâĂŹs ratios — were the same ones used for obtaining the analytical results. All boundaries were free to move

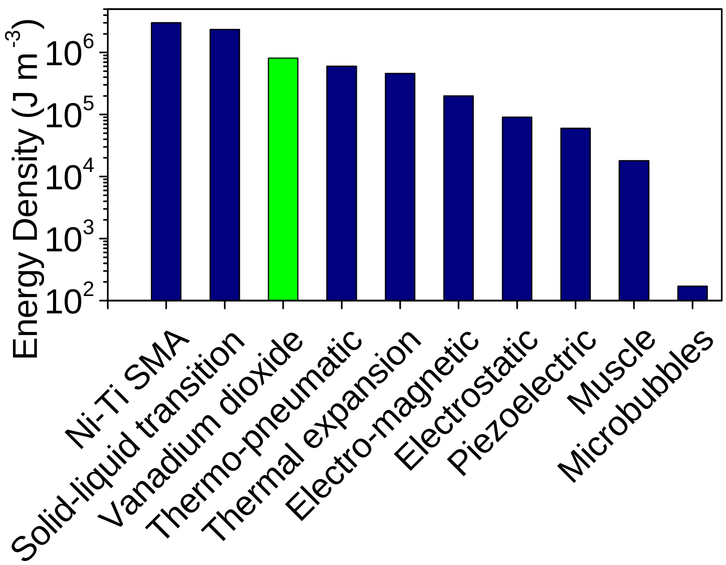

Figure 3.7: Strain energy densities of different micro-actuators including the VO_2-based micro-actuator studied in this thesis (green). The actuation mechanism for each micro-actuator can be found in the referenced work [19].

except one end of the cantilever, which was fixed. An initial strain of $-0.256\,\%$ was chosen, which produced the initial micro-actuator tip deflection of 67 µm observed experimentally at 21 °C. Since the VO_2 phase transition is a highly nonlinear hysteretic phenomenon, there are no preset parameters or functions that capture the behavior of VO_2 in the simulation software. To include this effect in the simulation, a nonlinear fit of the calculated strain as a function of temperature produced solely by the VO_2 transition was done through a nonlinear least square method of a modified Boltzmann model. For simplicity purposes, only the strain major heating curve, shown in **Figure** 3.5, was taken into consideration in the simulation and in the nonlinear fit. The strain produced only by the VO_2 transition was obtained by subtracting the thermal expansion terms from **Equation** (3.2) such that

$$\varepsilon_{\Phi T} = \varepsilon_{\Phi T} - \left(\alpha_f - \alpha_s\right)\left(T - T_{ref}\right), \tag{3.6}$$

where is the thermal expansion coefficient, T is temperature in Celsius, and T_{ref} is the strain reference temperature (assumed to be 21 °C). The transition strain $\varepsilon_{\Phi T}(T)$ was used to find the parameters of the model $\varepsilon_{\Phi TS}(T)$ given by

$$\varepsilon_{\Phi TS}(T) = \frac{a_1}{1 - \exp{(T - a_2)/a_3}} + a_4 T^2 + a_5 T + a_6, \tag{3.7}$$

where a_{1-6} are the six model parameters (summarized in **Figure** 3.8). As seen in **Figure** 3.8, the model efficiently fits the experimental data with a coefficient of determination (R-squared) of 0.9998.

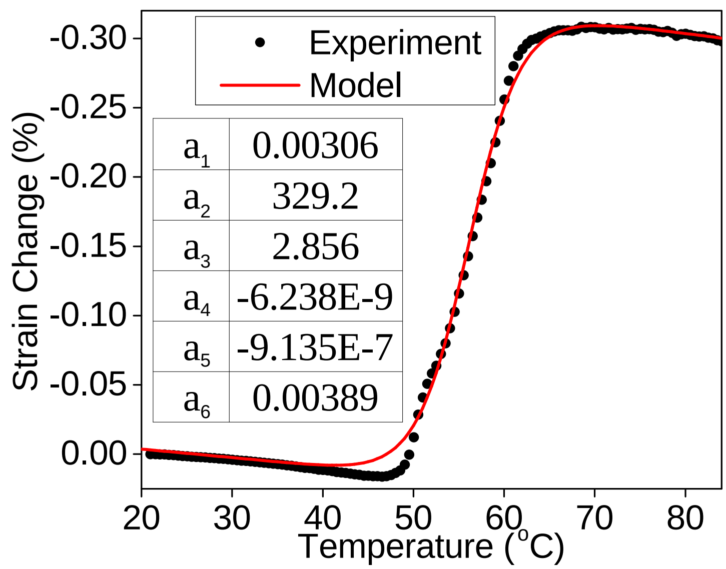

Figure 3.8: Experimental strain change produced by the VO_2 phase transition (dots) and modified Boltzmann model (line) as a function of temperature. The inset table show the model parameters fitted by the experimental values.

Equation (3.7) was included in the simulation as an axial strain, in the direction of the micro-actuatorâĂŹs length, on the VO_2 layer in the micro-actuator along with the thermal expansion effect of both layers. A temperature dependent study was performed where the temperature was monotonically increased from 21 °C to 84 °C uniformly through the cantilever length in steps of 0.5 °C. **Figure** 3.9 shows the curvature change obtained from the simulation along with the experimental values. The simulated values clearly follow the experimental values, which validates the strain change obtained from the experimental data with **Equation** (3.2). **Figure** 3.10 shows the strain energy density obtained from the simulation and the experimentally obtained values as a function of temperature. The behavior

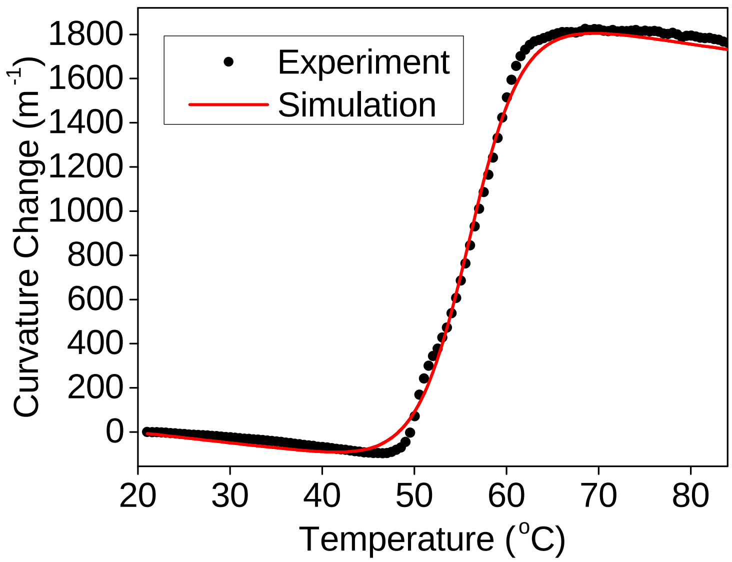

Figure 3.9: Experimental (dots) and simulated (line) curvature change as a function of temperature.

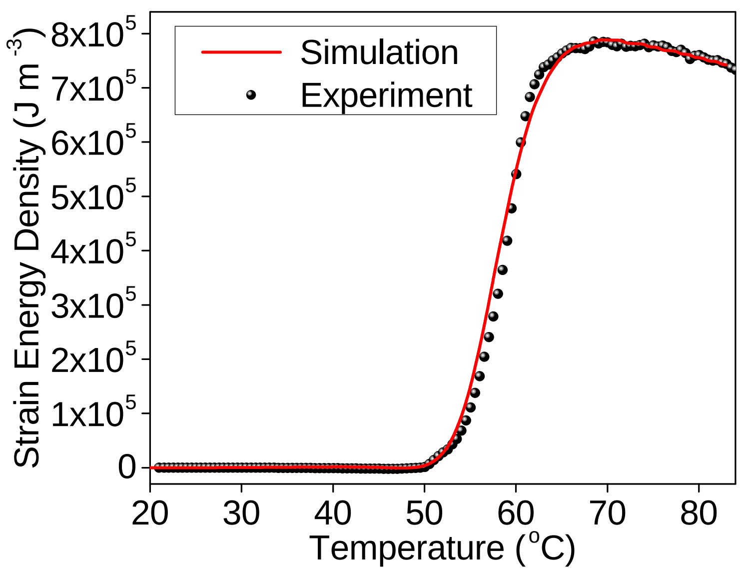

Figure 3.10: Experimental (dots) and simulated (line) curvature change as a function of temperature.

between both curves is similar, corroborating the strain energy density values obtained experimentally.

3.3 Photo-thermal Actuation

The following two types of experiments were designed to study and compare the dynamics of photo-thermally driven VO_2:Cr-coated micro-cantilevers when actuated in air or water. The reason for using Cr-doped VO_2 thin films is due to the slightly higher quasi-static performance that was observed in other experiments [95].

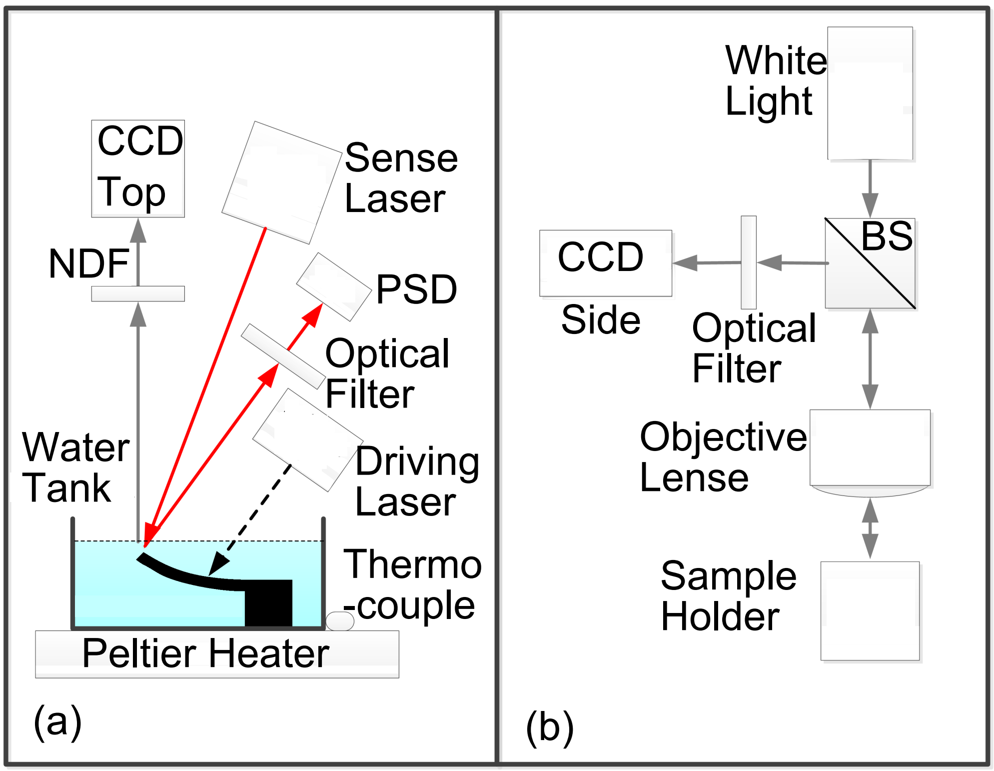

Figure 3.11: Measurement setup for frequency and time response experiments (a) and optical setup for the side view images of the micro-cantilever (b).

The setup schematically shown in **Figure** 3.11 was used, with the tank empty or filled with DI water, according to the case. In the frequency response experiments, a modulated driving laser (672 nm wavelength) was focused on the cantilever plane, illuminating the film surface, while the maximum amplitude of the tip oscillation was monitored as a function of frequency using a side-looking CCD camera. In the time response experiments the transient signal of the tip displacement as the cantilever was illuminated by a heating pulse was recorded by detecting the beam from a second laser (low power, 808 nm wavelength), which was reflected from the cantilever tip.

The chip body and tank base, cemented to the heater, acted as a heat sink. The power of the actuating laser beam used in each case was 100 mW and 150 mW in air and in water, respectively. The driving laser was focused on the cantilever plane with a spot size diameter corresponding to that of the microcantileverâĂŹs length (250 µm). The laser output was modulated as a square wave with 50 % duty cycle using a house-built electronic circuit. The âĂIJonâĂİ value corresponded to the minimum power required for maximum bending for the cantilever (for each medium). The sensing laser used for the time-response experiments and was focused on the tip of the cantilever with a laser spot size close to the width of the cantilever (40 µm). The reflected sensing beam was detected by a linear position sensitive diode (PSD) (Hamamatsu C-3683-1) with very high sensitivity in the near IR range. The PSD outputs a voltage proportional to the position of the laser spot, which was observed and recorded in a storage oscilloscope. Since the output of the PSD represents a relative displacement, the system was calibrated using the side-looking CCD camera. This camera and its corresponding optical components — shown in **Figure** 3.11-(b) — were arranged in a spatial plane perpendicular to the first setup, providing a side view of the cantilever.

The results for the frequency response experiments in both fluids are shown in **Figure** 3.12. The amplitude is expressed in decibels (dB), relative to the amplitude at 1 Hz, as a function of frequency in a log scale (i.e. a Bode diagram). For illustrative purposes, **Figure** 3.13 shows still images from the video taken with the side-view camera as the cantilever was actuated with the pulsed laser in air or in water, and at two different driving frequencies.

With the cantilever in air, the vibration amplitude is constant up to a frequency of 500 Hz, when it starts decaying and reaches the 3 dB loss at 1 kHz and afterward continues decaying at a rate of $-22\,\mathrm{dB\,decade}^{-1}$. For the case where the cantilever is submerged in water, from 1 Hz up until 7 Hz the amplitude decays at approximately $-1.5\,\mathrm{dB\,decade}^{-1}$ where it reaches -1.3 dB. From 7 Hz the amplitude starts decaying at a much more rapid rate of approximately $-8.5\,\mathrm{dB\,decade}^{-1}$ and reaching a 3 dB loss, compared to its initial

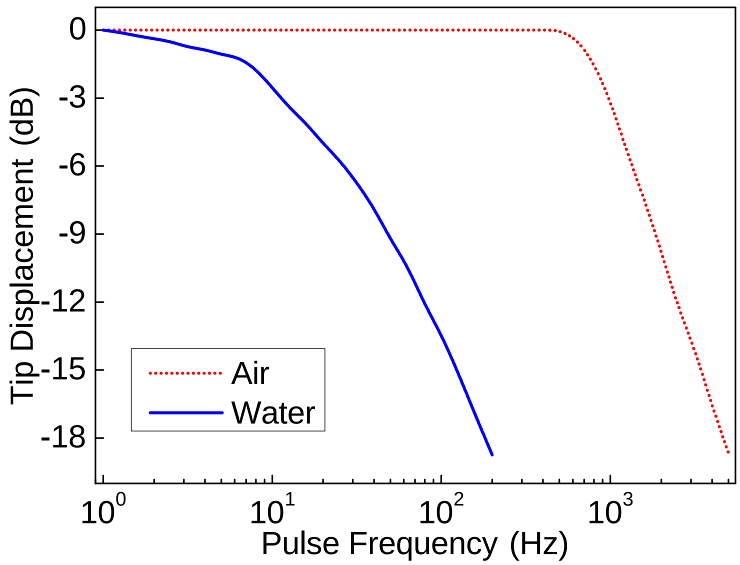

Figure 3.12: Vibrational amplitude in decibels as a function of laser pulse frequency for the cantilever actuated in air and water.

gain, at approximately 11 Hz. After 30 Hz the decay rate becomes slightly steeper as the frequency is increased, up to the maximum measured frequency of 200 Hz. The amplitude, after this driving frequency, was too small to be measured by the means employed. At a driving frequency of 100 Hz the cantilever in air still vibrates at maximum amplitude, while in water it has already decayed from 53 µm to 11 µm. At 1 kHz, there is no longer an observable response in water, while it is still 33 µm in air. In order to test for response degradation under repeated laser pulses with the beam intensities used for actuation during the experiments in both media, the cantilever was exposed, for two hours, to laser pulses of 100 Hz and 10 Hz in air and in water, respectively. After these exposures the cantilever had been subjected to tens of thousands of pulses and showed no reduction in vibration amplitude. A more detailed discussion can be found in [28]. In [28] it is concluded that the amplitude decay observed in the measurements are essentially unrelated to fluid drag and can instead be a consequence of heat transfer effects in the cantilever and the surrounding medium.

To better understand the transient effects of the pulse-driven cantilever, the time response experiments were performed. **Figure** 3.14 shows the measured tip displacement as a function

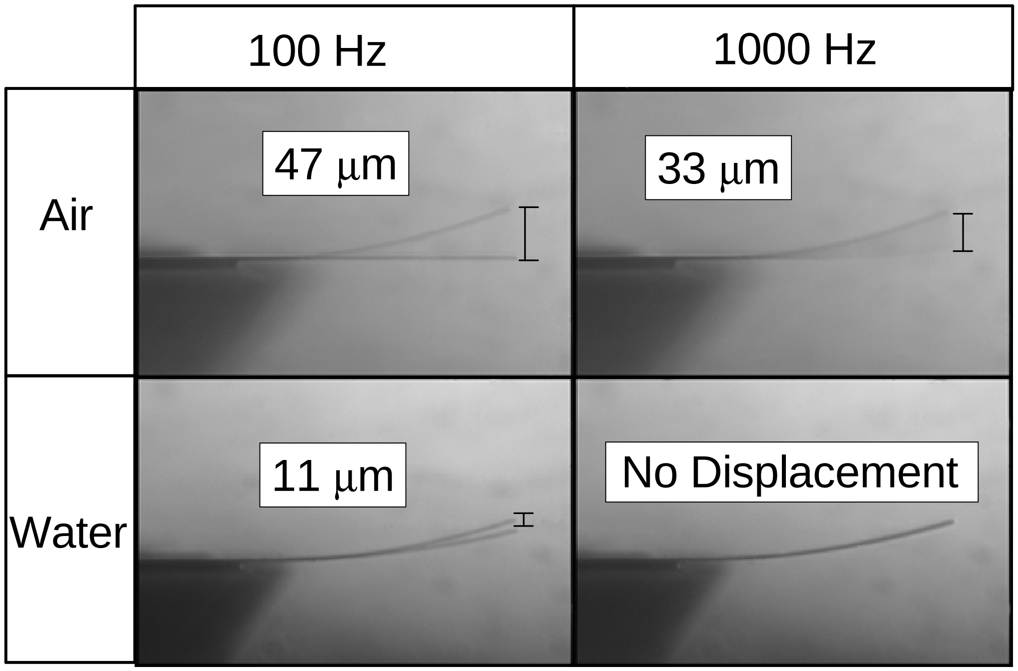

Figure 3.13: Still images from the video taken with the side-view CCD camera as the cantilever was actuated at the indicated frequencies with the heating laser in air (top images) and in water (bottom images). The measured vibrational amplitude is shown for each case. After 200 Hz there was no measurable displacement for the cantilever in water.

of time for the cantilever in air and in water. In both cases the laser was turned on and off at the specified âĂIJlaser onâĂİ and âĂIJlaser offâĂİ instants. Slower response is observed for the cantilever in water, in which case the rise-time is 30 ms, compared to 0.58 ms air and the fall-time is 32.5 ms, while in air it is just 0.45 ms. Both, rise- and fall-times are defined here as the time it takes the cantilever to go from 10 % to 90 % of its final deflection value. The relatively fast rise- and fall-times for the cantilever in air are in good agreement with the observed 3 dB cut-off frequency of nearly 1 kHz. While the frequency dependence results for the cantilever in water were more complex, the 3 dB cut-off frequency, at slightly more than 10 Hz is also in agreement with the observed transient times. The transient response in air shows small oscillations just after the laser pulse is turned on and just after it is turned off (**Figure** 3.14-(a)). These oscillations may be caused by rapid thermal transients along

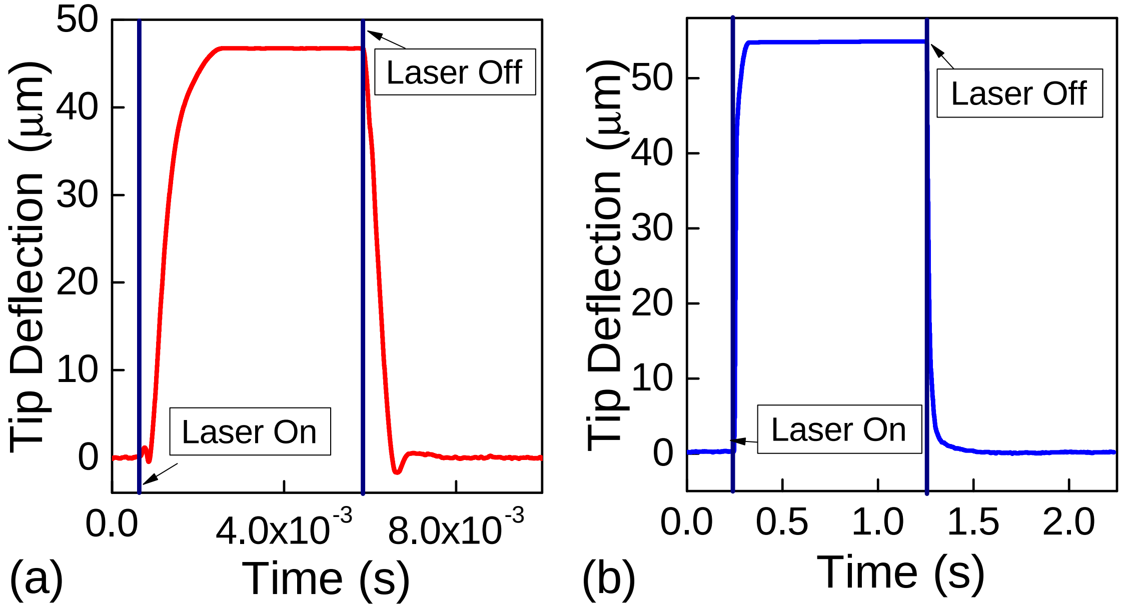

Figure 3.14: Measured tip displacement of the VO_2:Cr coated cantilever as a function of time in air (a) and in water (b) through a complete laser pulse.The vertical lines denote the times of laser pulse turning on and off. Note the difference in the time scale.

the cantilever associated with the fact that light intensity is not constant across the incident beam. These oscillations were not observed in the case of the cantilever immersed in water. It is possible that the enhanced heat conduction provided by the water in contact with the cantilever reduces the magnitude of these transients.

The results obtained in this experiment suggest that VO_2-coated micro-actuators can be driven photo-thermally at frequencies higher than 500 Hz. The photo-thermal actuation can be substituted with integrated heaters in the devices that will make further device miniaturization possible.

3.4 Self-sensing and Hysteresis Reduction

The following experiments were performed to shown that self-sensing feedback can be achieved in VO_2-coated micro-cantilevers by using the VO_2 resistance to estimate the cantilever deflection. The VO_2 thin film was deposited following a similar procedure to the one used in **Section 3.1** and is discussed in more detail in [29].

The measurement setup shown in **Figure** 3.15 was used for all experiments performed in this thesis. The VO_2-coated Si micro-actuator (shown in cross-sectional view) was attached to the same test piece used during deposition, which was also Si coated with the same VO_2. This test piece was needed in order to create the electrical connections to the VO_2 and measure its resistance. These contacts were located next to the micro-actuator chip and fabricated by evaporating aluminum through a custom-made metal mask. A voltage divisor (not shown in the schematic) was used in order to measure the resistance of the VO_2 film.

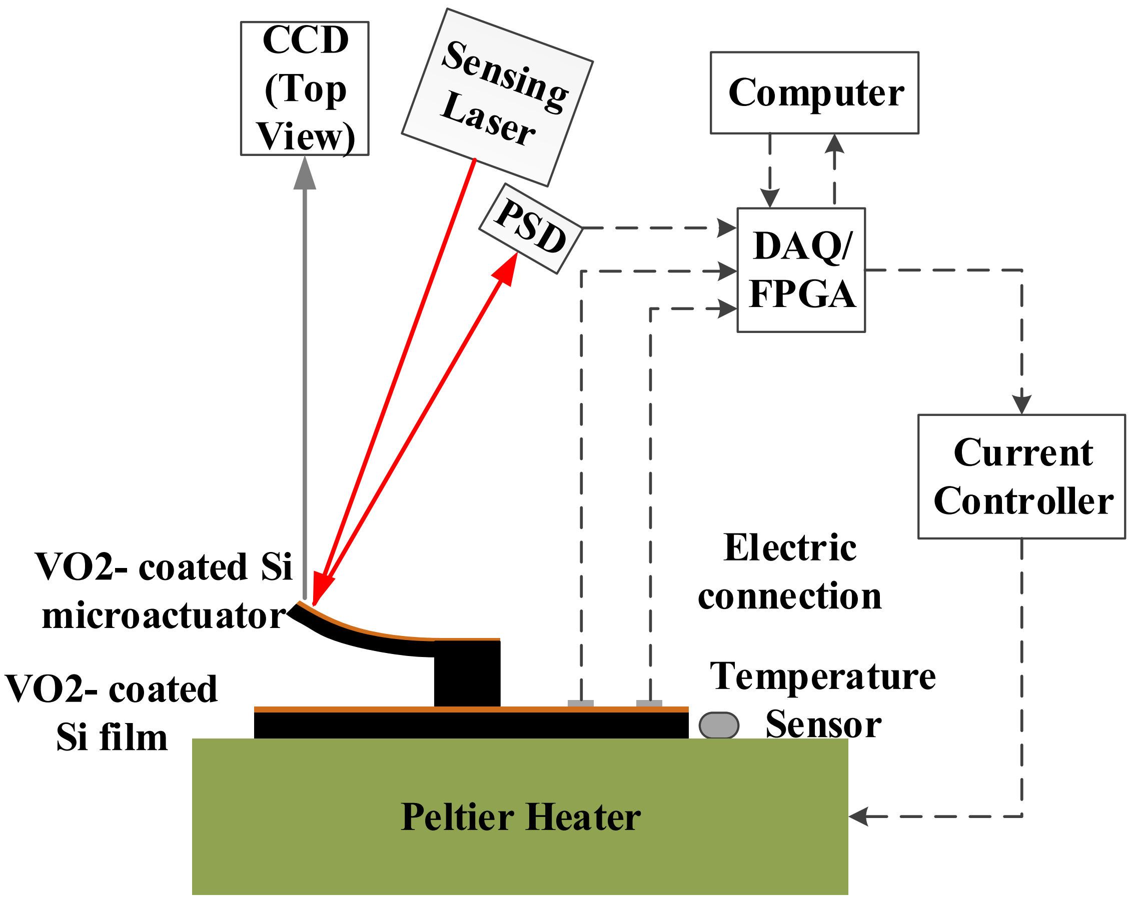

Figure 3.15: Schematic for the experimental setup used for deflection and resistance measurements as a function of temperature and the closed-loop control of self-sensed deflection. The micro-actuator, film and heater representations are cross-sectional views of the structures.

To measure the deflection of the device, a sensing laser ($\lambda = 808\,\text{nm}$, $0.5\,\text{mW}$) was focused on the tip of the micro-actuator and the reflected light was then focused on the active area of a position sensitive detector (PSD). A charged-coupled device (CCD) camera was used to aid in the alignment of the laser. The PSD output was a voltage proportional to the deflection of the micro-actuator, which was calibrated by sideview images of the cantilever at different deflection values. In particular, the calibration of the PSD reading was done by first assigning the initial deflection of the cantilever at 20 °C as 0 µm. Then the sample was heated to 85 °C, which resulted in the maximum deflection of the cantilever, 70 µm, as measured from the side view images of the cantilever. A Peltier heater was used to control the temperature of the sample. The temperature at the heater was measured with a platinum temperature sensor. A data acquisition card and field programmable gate array (DAQ/FPGA) was used to access the PSD output, the resistance of the VO_2 film, and the temperature sensor output. The DAQ/FPGA system was programmed to either: 1) control the temperature of the Peltier in closed loop in order to measure the deflection of the micro-actuator and the VO_2 resistance of the test piece simultaneously, or 2) control, using PID or robust controller, the deflection of the micro-actuator by self-sensing the deflection through resistance. For both cases the DAQ/FPGA controlled the magnitude of the current signal sent to the Peltier heater. All the variables were controlled and observed in a computer connected with the DAQ/FPGA system.

Figure 3.16 shows the major heating-cooling cycle of the micro-actuator deflection and film resistance as a function of temperature. The deflection in this thesis is defined as the tip displacement change relative to the initial position. A total deflection of 70 µm and a resistance drop of two orders of magnitude were measured during the VO_2 transition through a temperature span of 15 °C. Both variables were simultaneously measured, and by mapping deflection with resistance, it was observed that the hysteresis between the deflection and the resistance was significantly reduced, enabling the use of the resistance of the film in the test piece to estimate the deflection without the need of physically measuring its value.

The deflection-resistance mapping is shown in **Figure** 3.17-(a), which also includes a ninth-degree polynomial used to estimate the deflection in the experiments. This model was obtained from fitting the average of the heating and cooling curves and was used as the

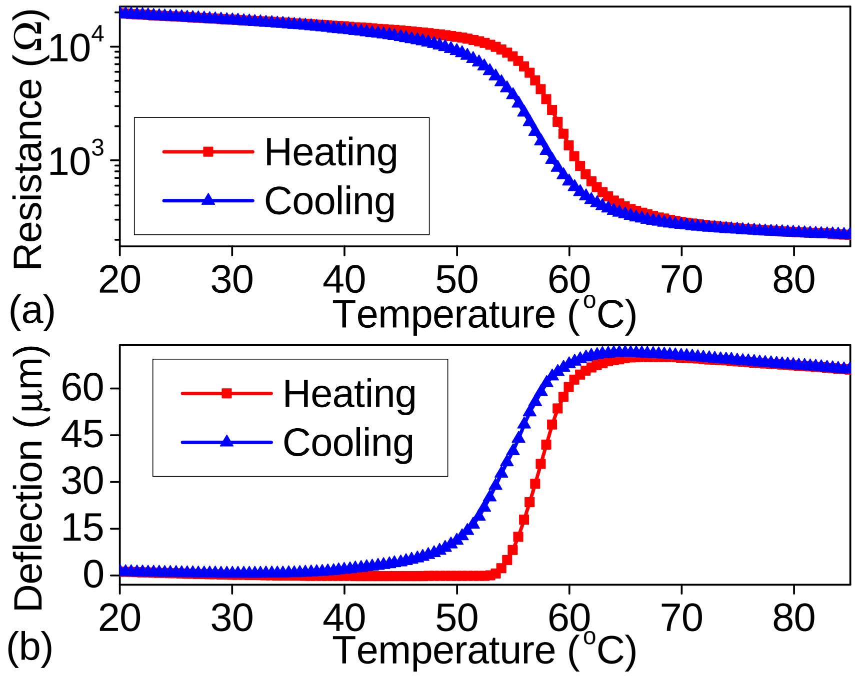

Figure 3.16: (a) VO_2 film resistance, and (b) VO_2-coated micro-actuator actual deflection as a function of temperature through a heating-cooling cycle (20 °C-85 °C). Both variables were simultaneously measured.

deflection sensing mechanism in the closed-loop deflection control experiments done in this work. The maximum errors between the heating/cooling curves and the self-sensing model are shown in **Figure** 3.17-(b). For a wide range of the resistance, the deflection estimation error was lower than 2 µm whereas slightly larger estimation error was found at the two ends. It is observed that some hysteresis remains. This is believed to be due to the slightly different energy requirements between the IMT and the SPT [27]. This hypothesis is supported by the fact that this difference in energy requirements has been found to be more pronounced at the onset of the phase transition, which would correspond to the higher resistance-low deflection region in **Figure** 3.17-(a). Hereinafter the estimated and measured deflection values will be addressed as self-sensed and actual deflections, respectively.

Two types of controllers will be considered and compared: 1) a PID controller, which only considers the error between the controlled variable (in this case self-sensed deflection) with the desired reference signal, and 2) a robust controller, which aside from considering the

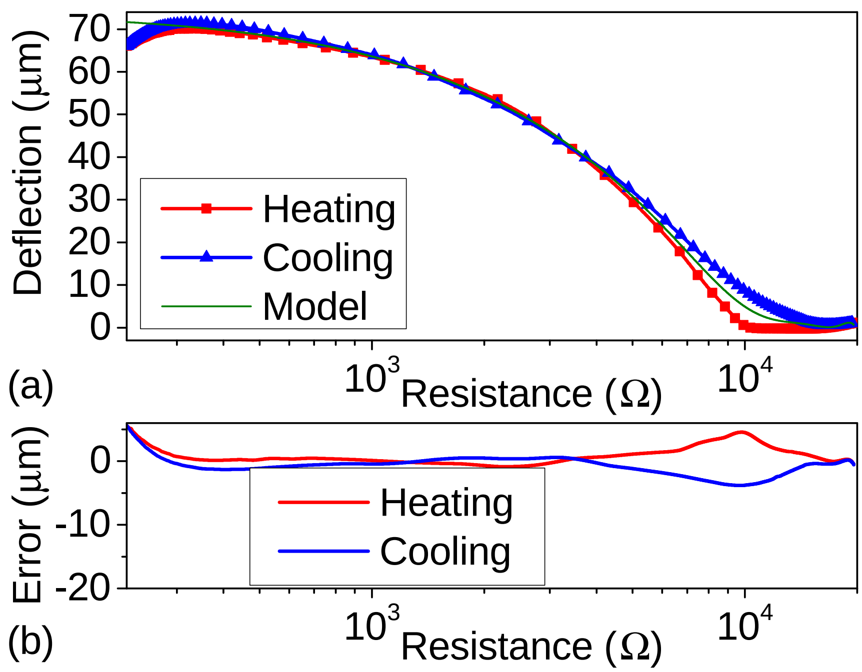

Figure 3.17: (a) VO_2-coated micro-actuator actual deflection as a function of VO_2 film resistance during the heating-cooling cycle. A polynomial function of degree 9 was used to model the deflection-resistance mapping. (b) Maximum model error obtained from the major heating and cooling curves.

error from the controlled variable, also accommodates the error brought by the self-sensing model, noises, and system uncertainties. The details on the system modeling and controller design can be found in [29].

For the following control experiments, the system was operated in closed-loop, where the designed controllers were used to control the actual deflection using only the resistance measurements. The block diagram shown in **Figure** 3.18 was used for this experiments. The variable y_{ref} is defined as the desired deflection output. The input of the controller is the deflection error defined as the difference between y_{ref} and the self-sensed deflection y_{self}. The controller output is the current I that goes to the Peltier, which produces temperature T. The VO_2 film resistance is defined as R, which is used by the self-sensing model to compute y_{self}.

Experiments with step reference inputs were designed so that the micro-actuator followed a set of three different setpoints, each with duration of 15 s, programmed in the DAQ/FPGA.

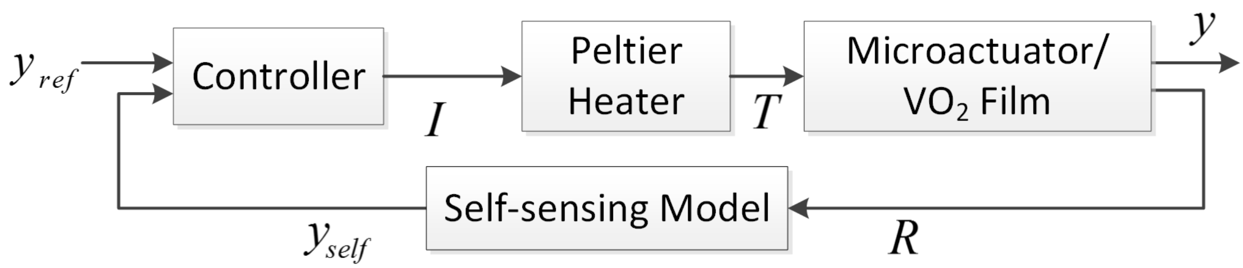

Figure 3.18: Block diagrams of the simplified physical closed-loop control system with self-sensing.

The goal of these experiments was to study the transient behavior and steady-state error of the robust controller and compare those to the performance of PID controller. **Figure** 3.19 show the experimental performance in terms of the actual deflection and self-sensed deflection. Although the controlled variable is the self-sensed deflection and a better steady-

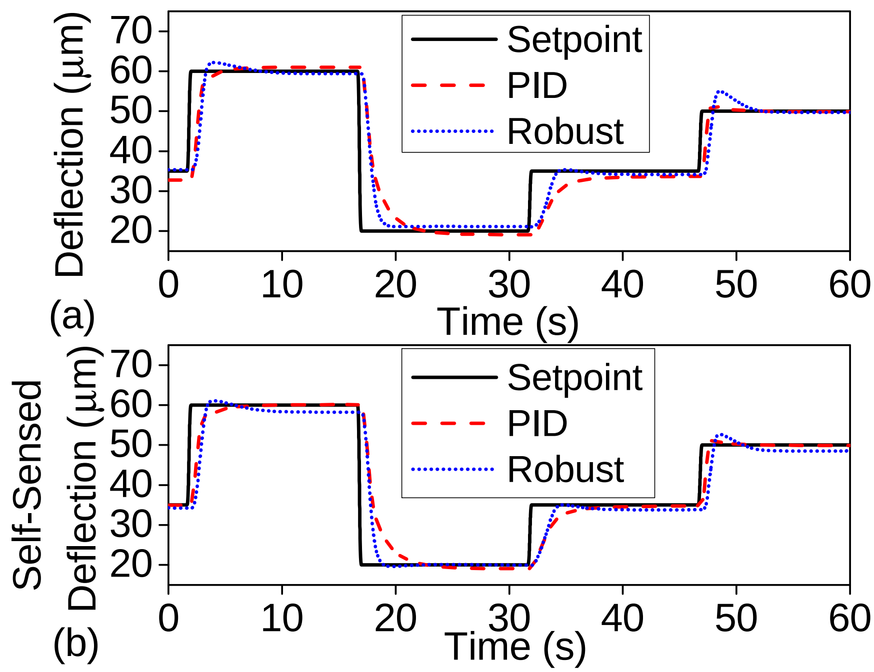

Figure 3.19: (a) Actual, and (b) self-sensed microactuator deflection under self-sensed, closed-loop PID and robust control through a series of step reference inputs.

state performance is observed in **Figure** 3.19-(b) for the PID, **Figure** 3.19-(a) shows that the actual steady-state deflection under the robust controller is closer to the setpoint for every step value, whereas it has a higher difference under the PID controller. The actual steady-state deflection errors and control efforts are shown in Fig. **Figure** 3.20-(a-b). Although the largest tracking error for both controllers is similar, the RMSE and average steady-state error under the robust controller are 3.66 % and 36 %, respectively, less than those of the PID. The advantages of the robust controller in terms of settling time over the PID controller can be noticed from **Figure** 3.19, although there is higher overshoot with the robust controller. In practice, the actual deflection performance is of relevance, thus only the actual deflection is provided for the remaining figures in this paper.

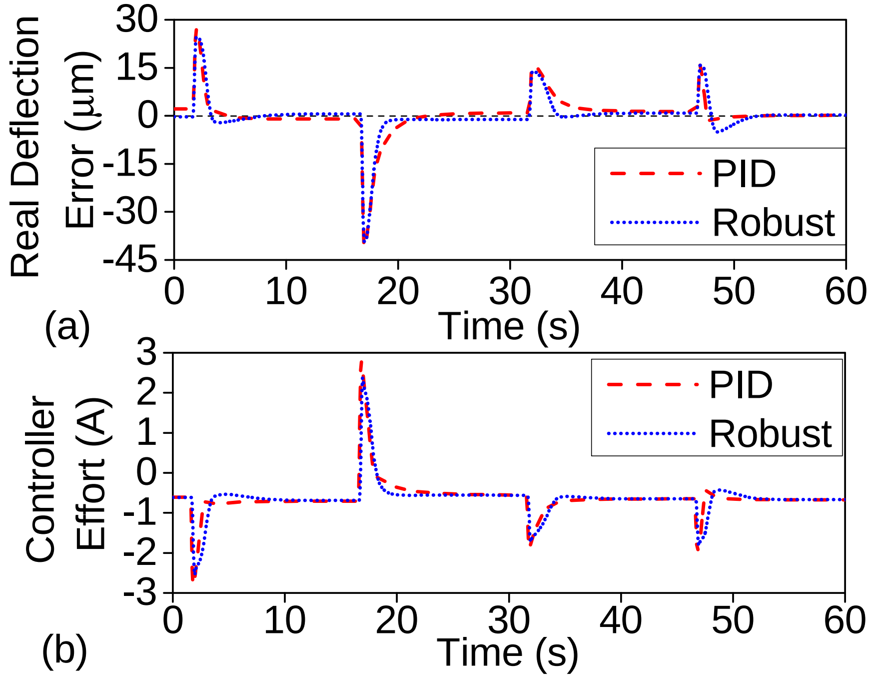

Figure 3.20: (a) Actual deflection error and (b) controller effort for the PID and robust control approaches through the step reference tracking experiment.

Experiments involving multi-sinusoidal reference inputs were carried out to study the performance of the micro-actuator under continuous input changes. For this experiment, the sum of three different sinusoidal waveforms with frequencies of 0.001, 0.005, and 0.01 Hz, maximum amplitude of 20 μm and an offset of 35 μm was chosen as the input signal. The different frequency components of the signal were used to study the deflection control at different frequency values. The amplitude and offset values were chosen in order to cover a wide actuation range throughout the hysteresis. **Figure** 3.21 shows the actual deflection of the micro-actuator as a function of time with PID and robust control. From the observed

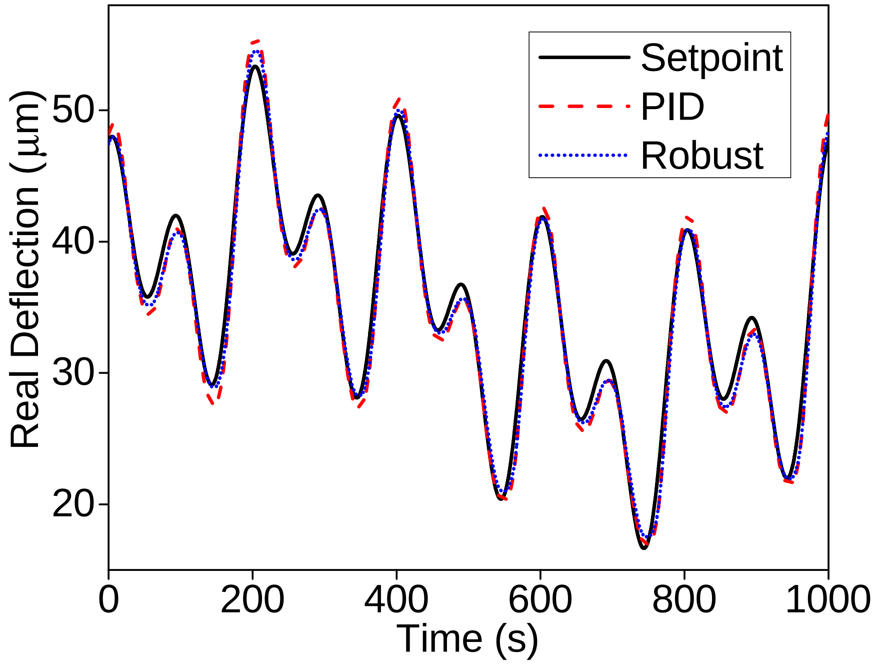

Figure 3.21: Microactuator deflection response to a multi-sinusoidal reference input under PID and robust control.

data, it is seen that the robust controller performance is better than that of the PID. This is more evident by looking at the tracking errors and control efforts under the two controllers, which are shown in**Figure** 3.22-(a) and **Figure** 3.22-(b), respectively. The robust controller has around 18 % less tracking RMSE and 1.8 % less control effort than the PID controller. The effectiveness of the robust controller in reducing the steady-state error of the actual deflection is again verified experimentally. These results suggest that self-sensing can be used to accurately control the VO_2 micro-actuators, although further miniaturization is required.

3.5 Summary

In this chapter, a comprehensive study on VO_2 applicability to smart material systems was performed. All the results from this section suggest that VO_2 micro-actuators are capable of

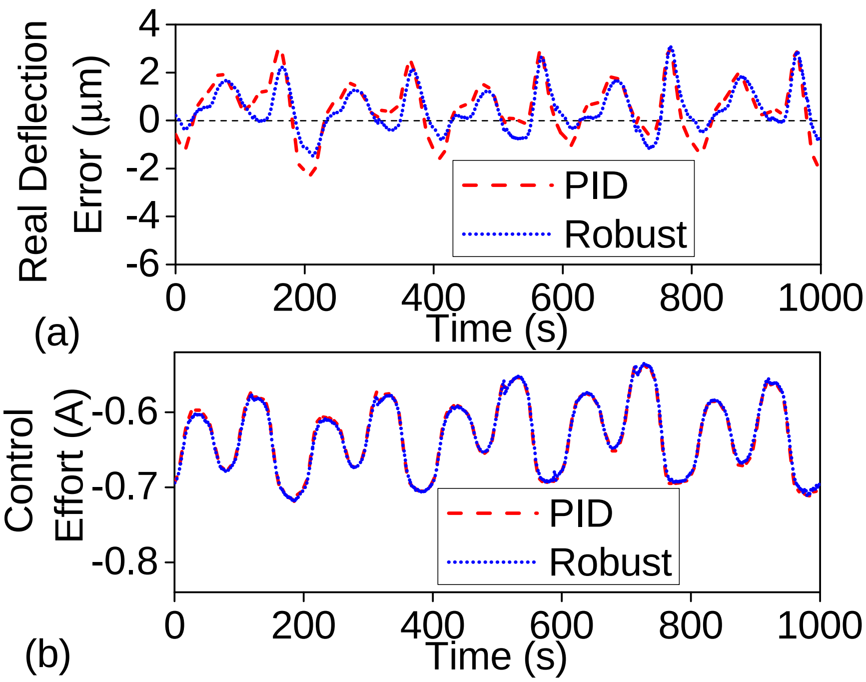

Figure 3.22: (a) Actual deflection error and (b) controller effort for the PID and robust control approaches in the multi-sinusoidal reference tracking experiment.

achieving very high displacements — with values comparable to the device length —, strain energy densities higher than $8 \times 10^5\,\mathrm{J\,m^{-3}}$, photo-thermal actuation responses higher than 100 Hz — which greatly depends on the device geometry. In addition, the use of self-sensing was proven through the successful estimation of micro-actuator deflection using resistance measurements, which reduces the deflection to resistance hysteresis and can be used to control the device. These capabilities can be combined by designing and fabricating a structure with monolithic integrated localized heater and self-sensing mechanism. The following chapter address the design and fabrication of the VO_2-based MEMS micro-actuator.

CHAPTER 4

DESIGN AND FABRICATION OF VANADIUM DIOXIDE MEMS ACTUATORS

In this chapter, the design, fabrication, and VO_2 deposition for the VO_2-based MEMS actuator used in the closed-loop control experiments using external sensing and integrated self-sensing are presented. The design specifications consists of a series of finite element method (FEM) simulations performed in order to determine the geometry needed to achieve a specific performance. In device fabrication, a detailed fabrication process of the micro-actuator is presented. Finally, the VO_2 PLD deposition used is explained.

4.1 Design Specifications

In order to achieve a desirable performance for micro-actuation, a series of design specifications are given. The micro-actuators should produce displacements higher than 50 µm, with a maximum power consumption of less than 10 mW and actuation speeds (bandwidth) higher than 20 Hz in order to compete with other thermal actuators. The electro-thermal actuation will be achieved by internal localized heaters fabricated along the device length with dimensions that meet the design specifications. In addition, a pair of vias will be created from the VO_2 to the Pt layer in order to create the electrical connections to the VO_2 along the structure length. This will be isolated from the heater connections and will be used as the self-sensing mechanism. **Figure** 4.1 shows a representation of the desired finalized device, with the VO_2 deposited on top.

VO_2-based MEMS micro-actuators can be optimized for deflection, bandwidth, and power consumption in many ways, such as varying the geometry of the device, the geometry of the heating element, and the thickness of the different layers. While decreasing the thickness of the layers improves the amount of deflection through the VO_2 transition, it also increases the amount of residual stress after fabrication, which greatly affects the device

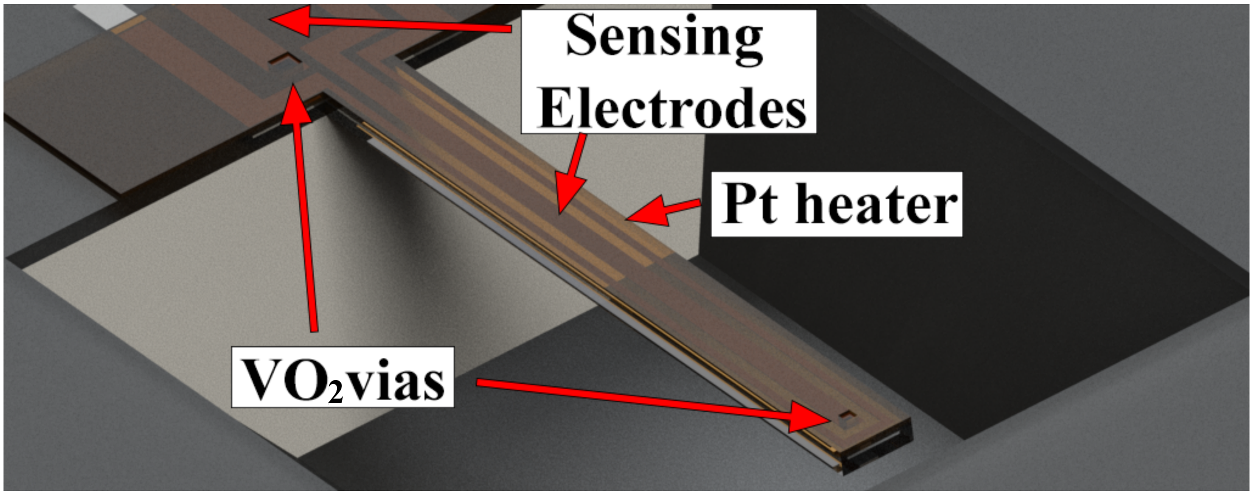

Figure 4.1: Rendered three dimensional image of the finalized micro-actuator, which shows the heater and VO_2 resistance measurement electrodes.

performance. Hence, this type of optimization is not pursued in this thesis. The geometry of the heater can be optimized to produce higher bandwidth and less power consumption at the cost of overall maximum deflection. This has been observed in previous experiments [25]. Since the device in this thesis requires the use of self-sensing through the length of the actuator, the heater geometry is constrained to a serpentine along the cantilever length. In terms of optimization by modifying device geometry, the length of the device is the optimization parameter pursued in this thesis analysis. While width can also be decreased to increase performance, for the present analysis it is constrained to 50 µm since decreasing it further decreases the self-sensing Pt electrode width resulting in possible self-heating.

To meet the required power specifications, a quasi-static electro-thermal FEM simulation was performed where different heater dimensions where tested. Since a total deflection of 80 µm is also required, the heater was designed throughout the length of the device, which would optimize deflection range. The width of the heater and self-sensing electrodes are 5 µm and 15 µm, respectively, with thickness of 200 nm. The electrodes are sandwiched between two SiO_2 layers 1 µm thick each and a 200 nm thick layer of VO_2 is drawn on top of the structure. The simulated geometry is shown in **Figure** 4.2 with consisted of a 550 µm long and 50 µm wide micro-cantilever with the specified layers and thicknesses.

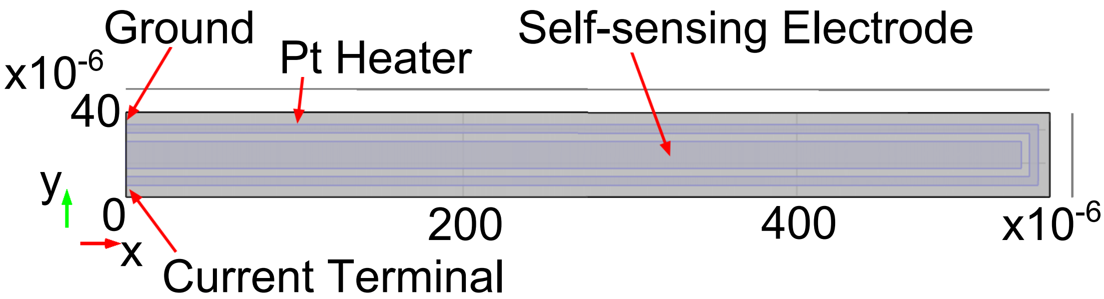

Figure 4.2: Top view of the simulated geometry.

Table 4.1 contains all the material thermal parameters used in the simulations. Common thermal properties were used for SiO_2, Pt and air, while for VO_2, values found in literature were adopted [102, 103]. The electrical conductivity of Pt was modeled as a function of temperature due to its highly temperature dependence [25], which can be approximated by $\sigma(T) = 8.9 \times 10^6 / (1 + 0.003729T)$. For the boundary conditions, one of the heater ends was set as ground while the other was set to have a constant current of 3.7 mA. Conductive heating through air was also considered in all directions and the anchor was assumed to be at 20 °C (room temperature). The resulting temperature distribution for the electro-thermal static actuation is shown in **Figure** 4.3. It is evident that this current input is more than necessary to induce the IMT and SPT of the VO_2 using this geometry. The measured Pt resistance under this temperature distribution is 160 Ω. This results in a power requirement of 2 mW, which is below the required value.

Table 4.1: Material parameters used in the electro-thermal and structural mechanics FEM simulations.

Parameters	Material			
	VO_2	Pt	SiO_2	Air
Heat Capacity C_p (J/(kg K))	700	133	730	1,005
Density ρ (kg/m^3)	4,670	21,450	2,650	1.18
Thermal Conductivity k (W/(m K))	4	71.6	1.4	0.025
Resistivity σ (S/m)	—	$\sigma(T)$	—	—
Young's Modulus E (GPa)	140	168	70	—
Poisson Ratio ν	0.33	0.38	0.17	—

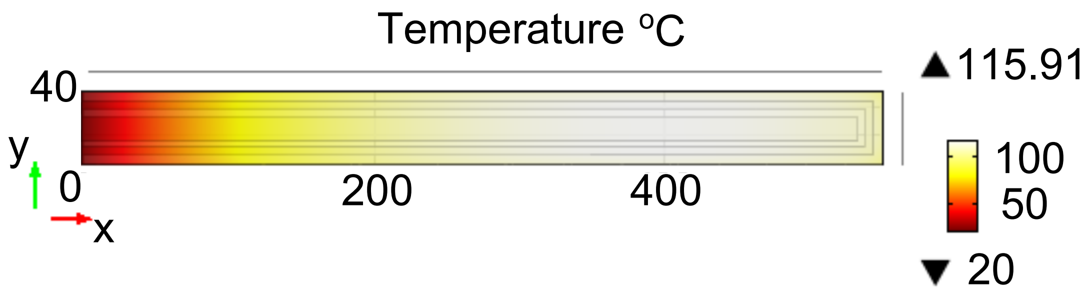

Figure 4.3: Temperature distribution obtained from the electro-thermal FEM simulation. The required power is 2 mW and the temperature is more than the required to induce the transition in VO_2.

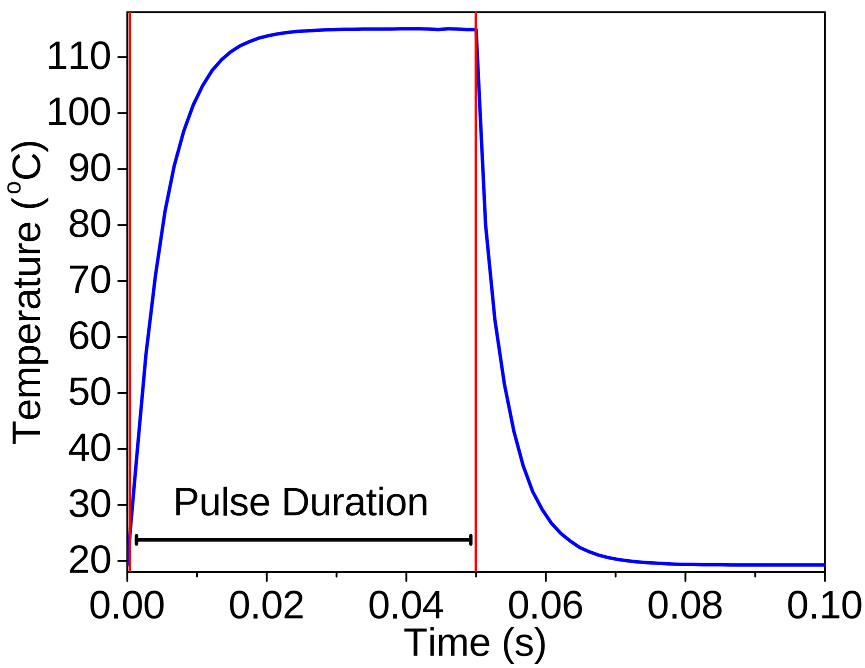

Figure 4.4: Temperature at the center of the free edge of the structure as a function of time during and after the current pulse.

It is known, from the photo-thermal experiments in **Section 3.3**, that the limiting mechanism for the dynamic performance on VO_2-coated micro-structures are the thermal dissipation through the anchor and the surrounding media. Thus, a time dependent electro-thermal FEM simulation was performed to determine the actuation speed of this design and ensure it meets the required 20 Hz cut-off frequency. The same geometry and boundary conditions from the static experiments with the exception of the input current, which now is a pulse function with duration of 100 ms at 50 % duty cycle and current "on" and "off" values of 3.7 mA and 0 mA, respectively. **Figure** 4.4 shows the temperature at the center of the free edge of the structure as a function of time that covers a pulse duration. This allows to see the heating and cooling transients of the structure. From the observed response a time constant — defined as the time it takes the temperature to reach 63 % of its step value — of 5.4 ms is observed, which results in a bandwidth of 30 Hz.

To ensure the device deflection will be greater than 50 µm, a solid mechanics static simulation is performed using the same geometry as before. A strain of 0.0032 is applied to the VO_2 layer, which was the value obtained in **Section 3.2** for fully actuated VO_2. The material parameters used in this simulation are shown in **Table 4.1**. The results under these conditions are shown in **Figure** 4.5 in which a deflection of 140 µm is obtained. This value is much greater than the desired specification. From the temperature distribution in **Figure** 4.3 it is noticed that not all the VO_2 will be fully actuated, which means that the value obtained from **Figure** 4.5 is an overestimate of the deflection. Nonetheless, more than 75 % of the cantilever length have temperatures above the transition temperature of VO_2, which is more than enough to meet the required specification. The overall deflection also depends on the residual stress of the structure after fabrication, which makes this estimation even harder. However, deflections higher than 50 µm have been obtained in structures with similar geometries [25].

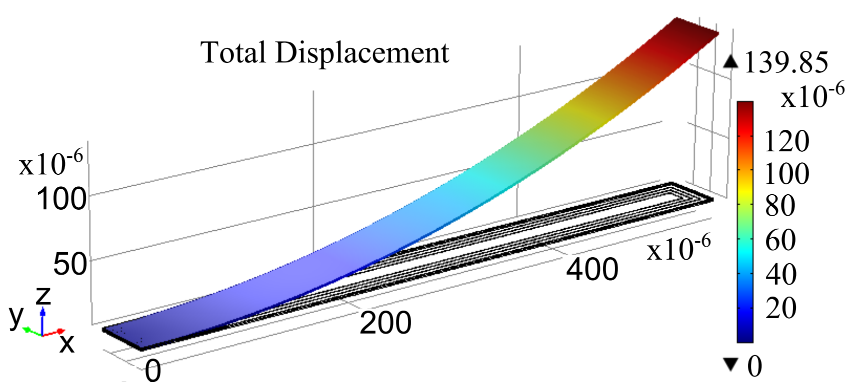

Figure 4.5: Deflection of the cantilever obtained from the structural mechanics simulation.

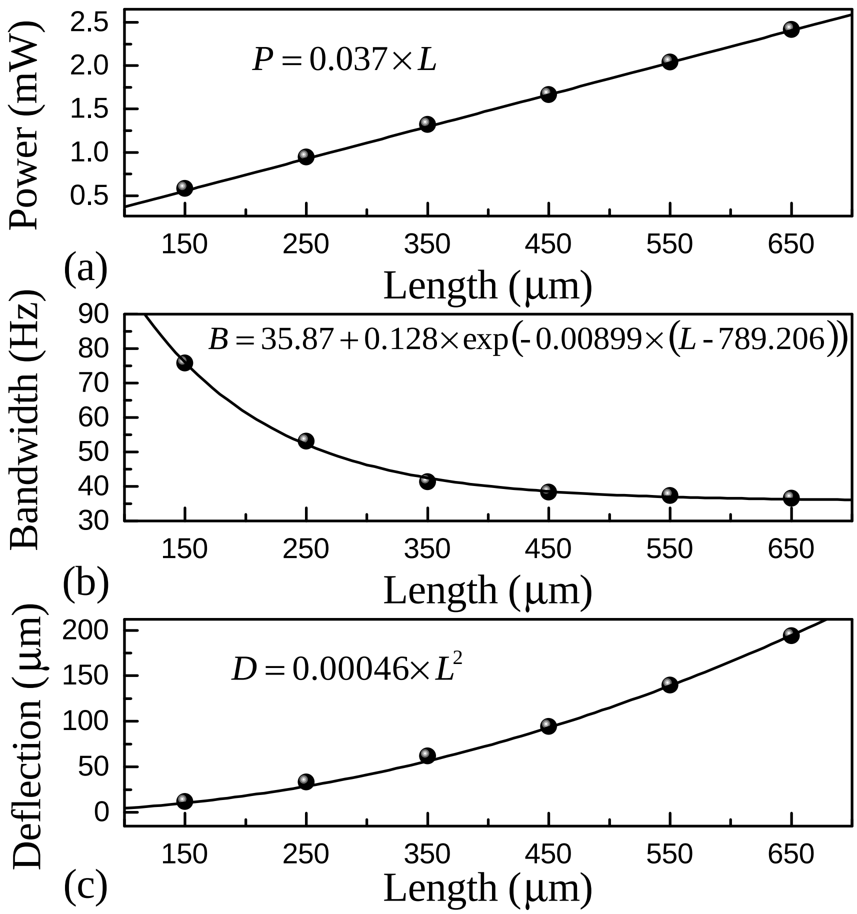

Figure 4.6: Simulation results for (a) the power consumption at constant maximum temperature, (b) temperature bandwidth, and (c) deflection at constant strain as a function of device length. The scattered points indicate the lengths at which the simulations were made.

Figure 4.6-(a-c) shows the power consumption, bandwidth, and deflection of the VO_2-based MEMS actuator used in this thesis as a function of device length. The power required to achieve a specific temperature increases linearly with length since thermal load increases. The bandwidth decreases exponentially with length reaching a limit value of approximately 35 Hz. The deflection of the micro-actuator increases nonlinearly as a function of length. Although this increase can be approximated by the equation in **Figure** 4.6-(c), a more accurate representation is given by the transcendental equation in **Equation** (3.1). Note that, while decreasing the length increases the bandwidth, the amount of deflection decreases as well. Hence, these devices can be optimized depending on the application and the required specifications following the design analysis employed in this thesis.

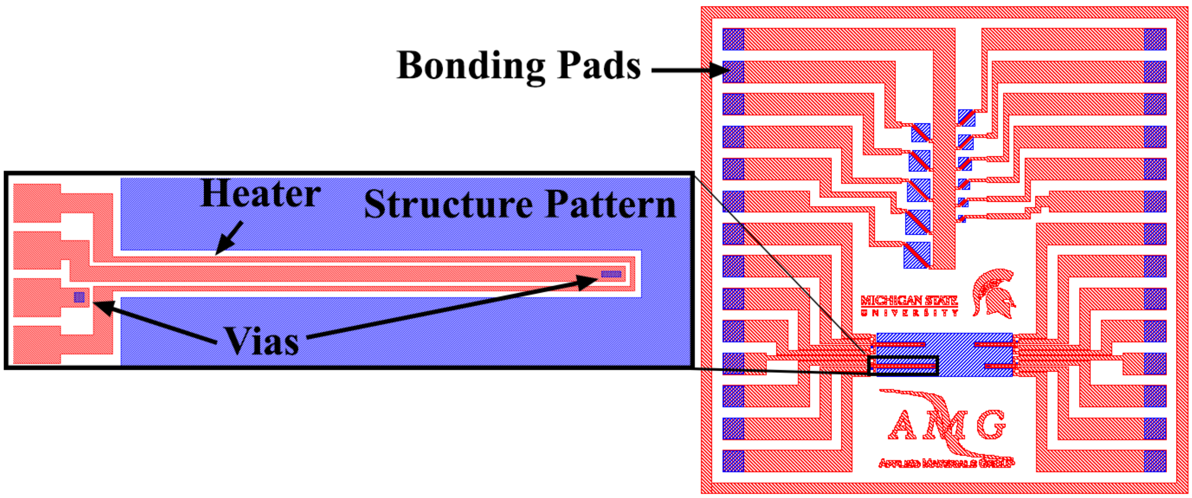

Figure 4.7: Masks used for the fabrication of the VO_2-based MEMS actuator.

4.2 Device Fabrication

After verifying, through the FEM simulations, that the design specifications meet the requirements, the masks and the fabrication process flow are developed. The design consists of a two step lithography process, which requires just two masks (shown in **Figure** 4.7). The first mask (red) is for metallization of the heater and self-sensing electrodes and the second mask (blue) is for creating the micro-actuator pattern and the vias to the self-sensing electrodes.

The VO_2-based MEMS actuator used in this work consisted of a titanium/platinum (Ti/Pt) electrode sandwiched between two layers of SiO_2 with a VO_2 layer on top of the device. A rendering of the fabrication process flow steps is shown in **Figure** 4.8 along with a description of each step. A 1 µm layer of SiO_2 is deposited on the polished side of a (100) Si wafer using low thermal oxide (LTO). After the SiO_2 deposition, the wafer is cleaned and prepared for lift-off using a two layer resist of LOR 5A and Shipley 1813.

A combination layer of Ti/Pt (500 Å/1500 Å) is deposited through thermal evaporation followed by a lift-off step using Remover PG and then cleaned using NanoStrip. The Ti layer is used for addition between the Pt and the SiO_2 layers. A second 1 µm SiO_2 layer is deposited on top of the patterned Pt using LTO. This oxide layer serves to electrically isolate the Pt and the VO_2 deposited on the final step. The wafer is then patterned with Shipley 1813 to create the micro-actuator pattern to be released, the wire bonding pads, and the vias that will expose the Pt to the VO_2 in the cantilever. Deep reative ion etching (DRIE) is used to etch the SiO_2 on the exposed areas until the Pt and Si are revealed. The wafer is partially diced into 0.25×0.25 inch dies and the MEMS actuators are then released using xenon difluoride (XeF_2). After performing the release step, a 200 nm VO_2 layer is deposited

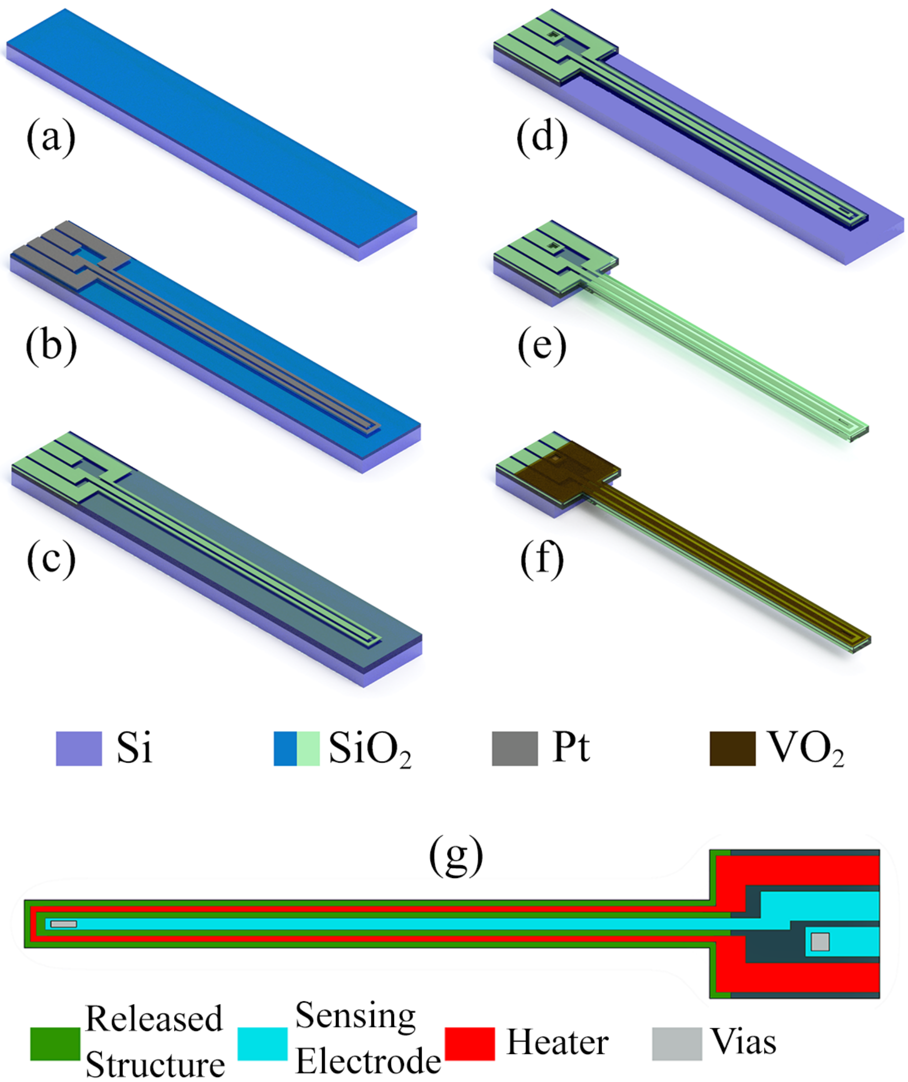

Figure 4.8: Fabrication process flow of the VO_2-MEMS-actuator. (a) Deposition of SiO_2 by LTO (first layer), (b) thermal evaporation of Pt and pattern by lift-off, (c) deposition of SiO_2 by LTO (second layer), (d) DRIE etching of SiO_2 for device pattern, (e) MEMS release by XeF_2 etching of Si, (f) Deposition of VO_2 by PLD.

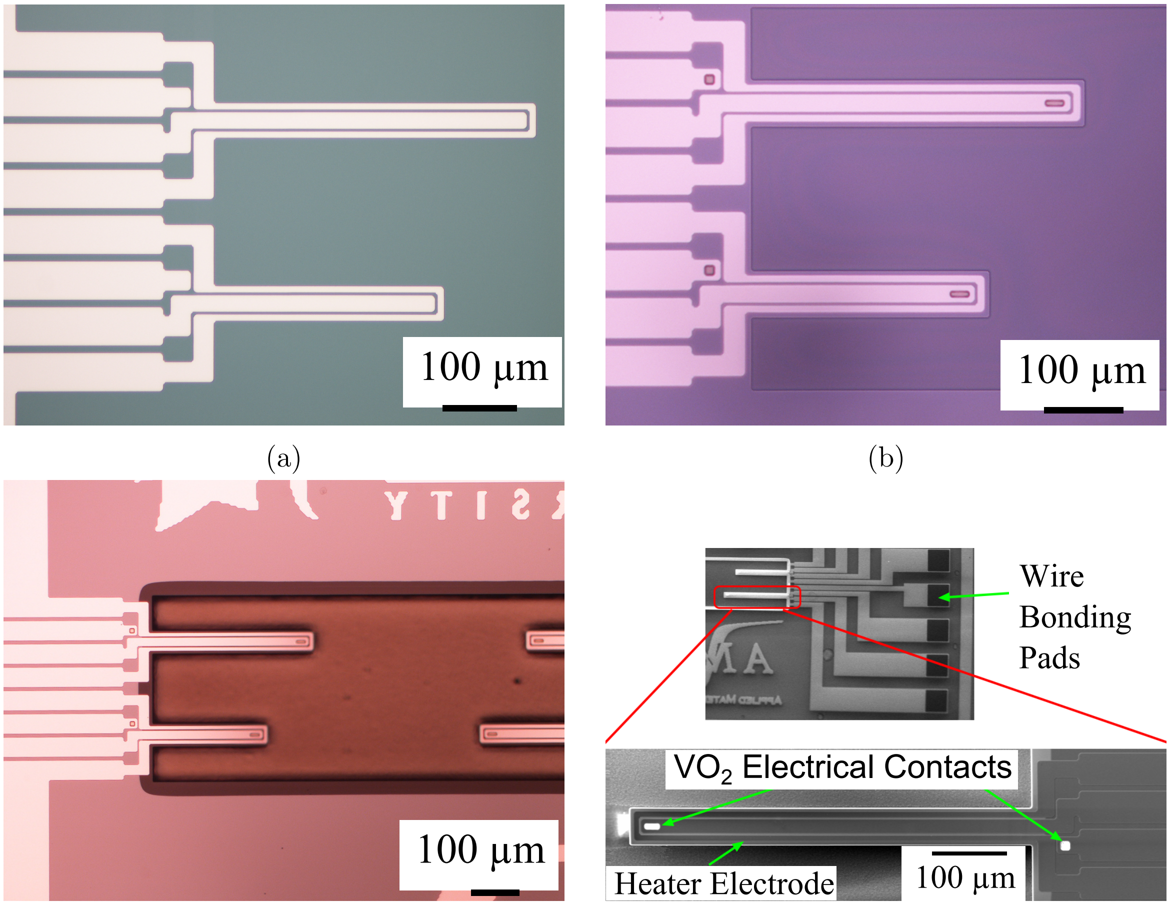

(a) (b) (c) (d)

Figure 4.9: Images of the fabrication process at different steps.

using pulsed laser deposition (PLD).

During the PLD deposition process, an individual die is placed on a rotating holder in order to ensure uniform thickness and temperature distribution through the deposition process. A shadow mask is placed directly on top of the die to protect the wire bonding pads from the VO_2 deposition. Before deposition, a background pressure of 5×10^{-6} Torr is reached. Then, a heater located at the back of the sample is controlled to a temperature of 550 °C under an oxygen atmospheric pressure of 15 mTorr. A krypton fluoride (KrF) excimer laser is then focused on a rotating metallic vanadium target with an energy of 350 mW and a repetition rate of 10 Hz. The deposition lasts for 30 min and its followed by another 30 min of annealing under same conditions. The finalized device consists of a 550 µm long and 50 µm wide micro-cantilever with Pt trace dimensions of 8 µm for the heater and 18 µm for the VO_2 resistance measurement electrodes. After deposition the die is placed on a integrated circuit (IC) package and wire bonded to create the electrical contacts to the Pt heater and the VO_2. **Figure** 4.9 shows microscope and SEM images of the MEMS fabrication at different stages.

4.3 Summary

In this chapter a detailed design methodology for the VO_2 MEMS actuator was presented. The design consisted of a series of FEM simulations that were performed to verify that the proposed actuator geometry met the desired performance specifications. The masks used for the fabrication of the device and a detailed fabrication process were presented along with images of the fabrication at different stages. In the next chapter, detailed characterization, modeling and closed-loop control of the device are presented.

CHAPTER 5
CLOSED-LOOP CONTROL

Through the successful integration of heaters in the fabrication of VO_2-based actuators, research groups have achieved low power actuation, fast response times, and large operational ranges through the electro-thermally driven transition [24, 25]. Nonetheless, open-loop actuation hinders the use of VO_2 MEMS actuators for micro-positioning and other applications requiring accurate movements due to their high sensitivity to their stimuli. In addition, the high sensitivity of VO_2-based actuators to temperature fluctuations represents a major challenge when implementing such devices in actual applications with non-controlled environments. The work presented in this chapter shows the characterization and testing of the first closed-loop controlled VO_2 MEMS-based actuator using the fabricated structure detailed in **Chapter 4**.

5.1 Measurement Setup

In order to characterize the device and perform the control experiments, the chip holding the micro-actuator was placed in an integrated circuit (IC) package and the electrical pads to the Pt heater and the VO_2 connections were wire bonded. The IC package was then placed on a custom-made PCB board, which contained the electrical traces to access the device. **Figure** 5.1-(a) shows the schematic representation of the measurement setup used for characterizing and controlling the actuator. A charge-coupled device (CCD) camera was used for aligning a near infrared laser diode ($\lambda = 808\,\mathrm{nm}$) with the tip of the actuator. The reflected light from the laser was focused into the active area of a position sensitive detector (PSD) (Hamamatsu S3270) whose output voltage (V_d) is proportional to the incident light from the laser. The voltage was connected to a field programmable gate array (FPGA) and a data acquisition (DAQ) system, in order to monitor the deflection of the actuator.

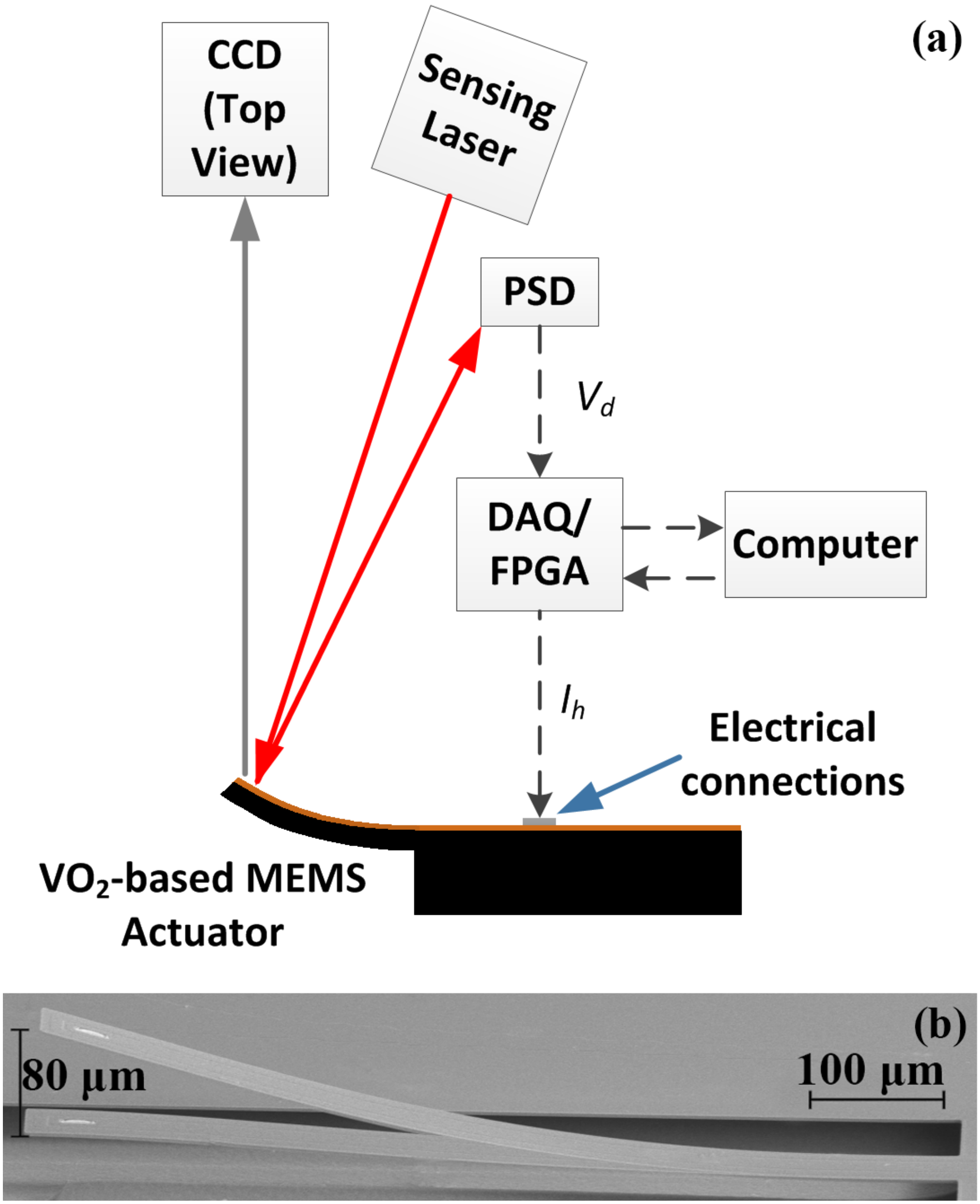

Figure 5.1: (a) Measurement setup for performing the characterization and control experiments on the actuator, and (b) Sideview of superimposed SEM images of the VO_2-MEMS-based micro-actuator at both actuation limits.

In the FPGA/DAQ, V_d was converted to the device deflection by performing a linear fit of the relationship between tip displacement and V_d at various Pt heater current values. The output of the FPGA/DAQ was connected to the integrated Pt heater in order to drive the actuator through Joule heating by supplying a current (I_h). The FPGA/DAQ was programmed to actuate the device in open or closed-loop and was used to obtain all the measurements shown in this work. A computer was used to interface with the FPGA/DAQ, change setpoint values, and extract the data.

5.2 Device Characterization

The measurement setup shown in **Figure** 5.1 was used to characterize the actuator in terms of quasi-static tip response, frequency response, transient response, creep, repeatability, and rate dependence. This characterization is essential, not only to obtain crucial information for the controller design, but also, to understand the working principles of the micro-actuator and how it can be optimized to achieve desired performance specifications.

5.2.1 Quasi-static Analysis

For obtaining the tip displacement as a function of current, an increasing-decreasing staircase current sweep, from 0 to 4.7 mA in steps of 0.3 mA, was applied to the integrated heater to electro-thermally drive the actuator. Each setpoint duration was set to 10 s (4 s of wait time, which were used to ensure the deflection reached steady-state, and 6 s of hold time, during which the deflection signal was averaged). **Figure** 5.2 shows the tip displacement as a function of current through the Pt heater. A similar behavior to that of previous experiments is observed, which is dominated by a non-monotonic hysteresis [14, 25, 26, 31].

The maximum observed deflection for the increasing current direction was found to be approximately 82 µm, which was different than the 80 µm observed in the SEM images due to the viewing angle. A larger deflection of approximately 95 µm was observed through the

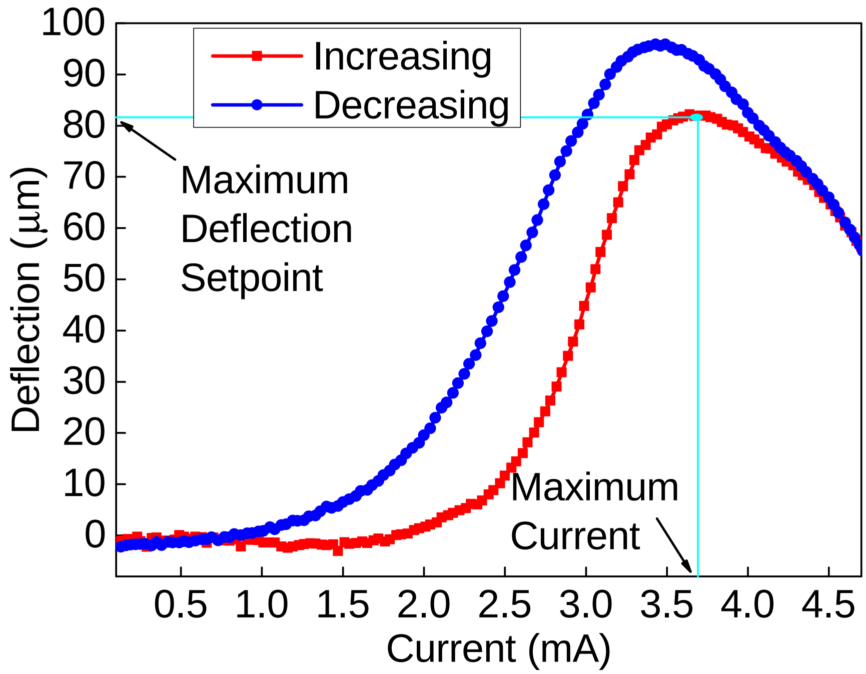

Figure 5.2: Tip displacement of the VO_2-MEMS-actuator as a function of current applied to the Pt heater.

current decreasing direction. The maximum controllable deflection chosen in this work was 82 μm due to the difficulties in controlling non-monotonic curves with a simple PID. At this maximum deflection the current and voltage were 3.64 mA and 1.28 V, respectively, resulting in a heater resistance value of 353.33 Ω and a power dissipation of 4.5 mW. It is important to note that the resistance value calculated here includes the Pt trace to and from the heater, although the trace resistance is smaller due to its larger geometries.

5.2.2 Frequency Response

The frequency response of the micro-actuator was obtained by applying a frequency varying sinusoidal current signal with adjustable offset and amplitude to the Pt heater while measuring the deflection amplitude. An offset and amplitude values of 2.75 mA and 0.75 mA were chosen, respectively, since the region of interest to be controlled is during the VO_2 film transition and these values result in the highest deflection gain (see **Figure** 5.2).

Figure 5.3 shows the gain of the micro-actuator, defined here as µm/mA, as a function of frequency. The behavior of the frequency response resembles that of a first order transfer function with a maximum magnitude of 45.5 µm/mA at low frequencies, with an experimental cut-off frequency (f_{ce}) of 42.7 Hz (268 rad/s), where f_{ce} is defined as the frequency where the magnitude is 0.707 times of the magnitude at DC. A plot of the model fitted with the experimental data is also shown in **Figure** 5.3 and will be explained in detail in the following section.

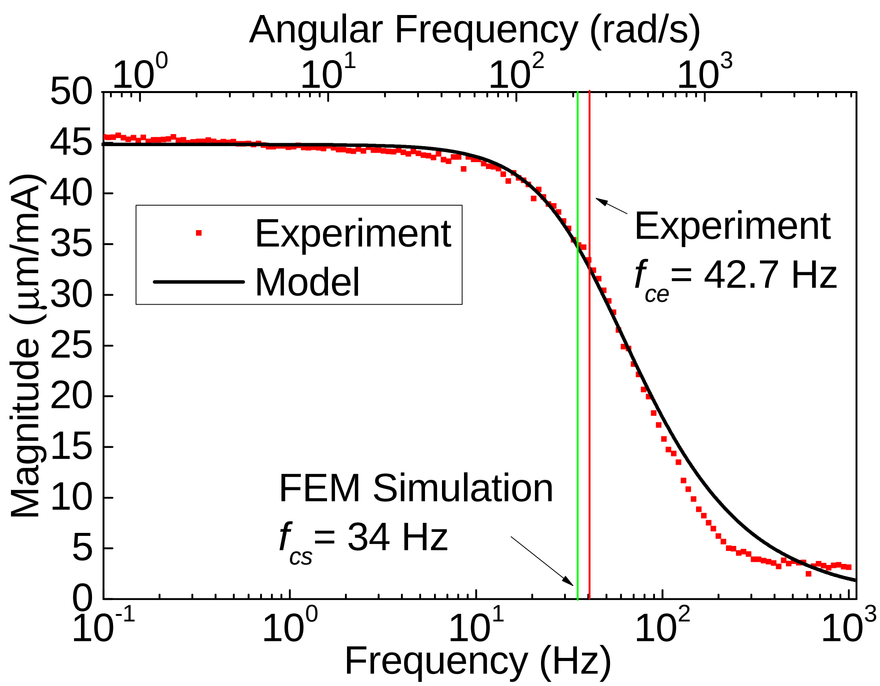

Figure 5.3: Experimental and fitted data of the deflection frequency response of the VO_2-based MEMS actuator.

To determine the mechanism limiting the performance of the actuator, an electro-thermal time-dependent FEM simulation was performed using COMSOL Multiphysics. The material parameters for heat capacity at constant pressure (C_p), density (ρ), thermal conductivity (k), and electrical conductivity (σ) used in the simulation are summarized in **Table 4.1**. Common thermal properties were used for SiO_2, Pt and air, while for VO_2, values found in literature were adopted [102,103]. The electrical conductivity of Pt was modeled as a function of temperature due to its highly temperature dependence [25], which can be approximated by $\sigma(T) = 8.9 \times 10^6 / (1 + 0.003729T)$. Using the geometry of the micro-actuator described previously, the results revealed a simulated cut-off frequency (f_{cs}) of 34 Hz, which is relatively close to f_{ce}. Thus, the mechanism limiting the performance of the micro-actuator in this work is the thermal dissipation through the device anchor and surrounding media, which is in accordance with previous work [25, 28].

5.2.3 Time Response

Another important experiment that reveals dynamic characteristics of the device is the time response of the micro-actuator. For this experiment, current steps were given to the heater while the tip deflection of the device was being monitored. The sampling rate for this experiment was 20 kHz, which is much larger than f_{ce}. The measured deflection throughout a series of current steps is shown in **Figure** 5.4. From the insets, the time constants associated with the increasing and decreasing steps were calculated to be 3.5 ms and 3.7 ms, respectively. Although their values are very similar, the differences may be due to the different system boundary conditions in both cases — there is no active cooling in the device — and the asymmetry of the deflection hysteresis. Similar behavior have been observed in [28].

Another observed feature from **Figure** 5.4 is the slow steady-state transient and, although one can think of it as being a result of material creep, it only seems to happen during cooling steps. Creep is known to be a temperature dependent process, increasing with increasing temperature, which is the opposite of what is observed in this experiment. A consequence of creep is permanent performance degradation [108] due to dislocations and material fatigue, which is not observed to happen for the VO_2-based MEMS actuator studied in this work. In a previous work, the authors did not find evidence of creep nor differences between heating and cooling in VO_2-coated Si cantilevers [26]. The actuation mechanism used in [26] was orders of magnitude slower than the thermal transients in the micro-device, which made the differences between heating and cooling transients unnoticeable. In this work, the micro-actuator thermal transients dominate the time response of the device, and

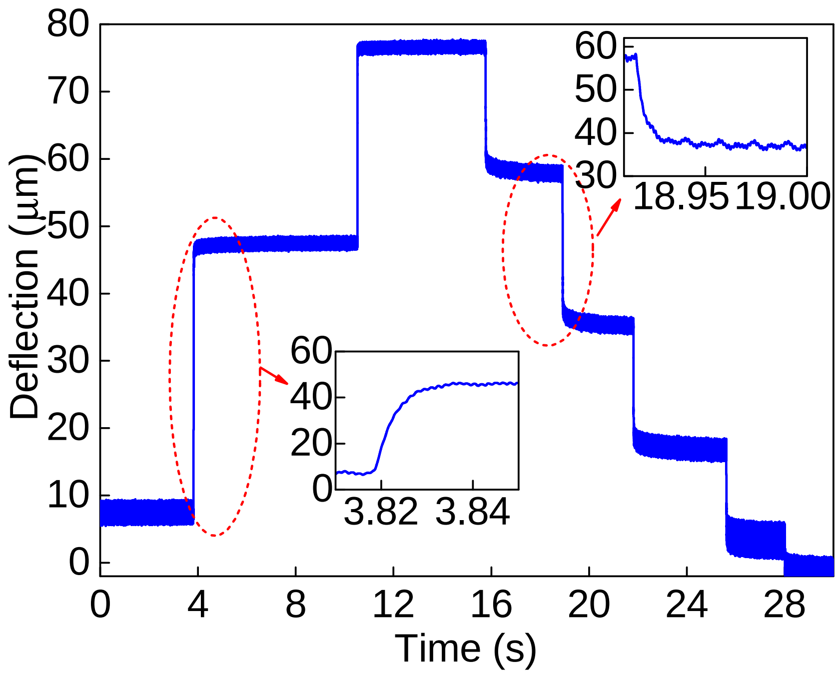

Figure 5.4: Deflection time response of the micro-actuator through a series of current steps. Two inset figures showing increasing (heating) and decreasing (cooling) steps were added to the figure for visualizing their differences.

thus, the differences between heating and cooling boundary conditions are more evident. This evidence suggests that the observed slow cooling transients might be due to differences in boundary conditions between heating and cooling rather than material creep.

5.2.4 Reliability

Reliability is a measure of similarity between two separate measurements under same conditions and measurement setup, which accounts for variations in measurement setup and device performance. The latter includes fatiguing, fracture, and degradation of the micro-actuator, while the former is related to vibrations and environmental disturbances. For achieving accurate control of the micro-actuator, it is important that both, measurement setup and the device performance, are repeatable and reliable.

To show the reliability of the VO_2-based MEMS actuator, a quasi-static deflection measurement was taken five days after all the measurements in this work were completed and

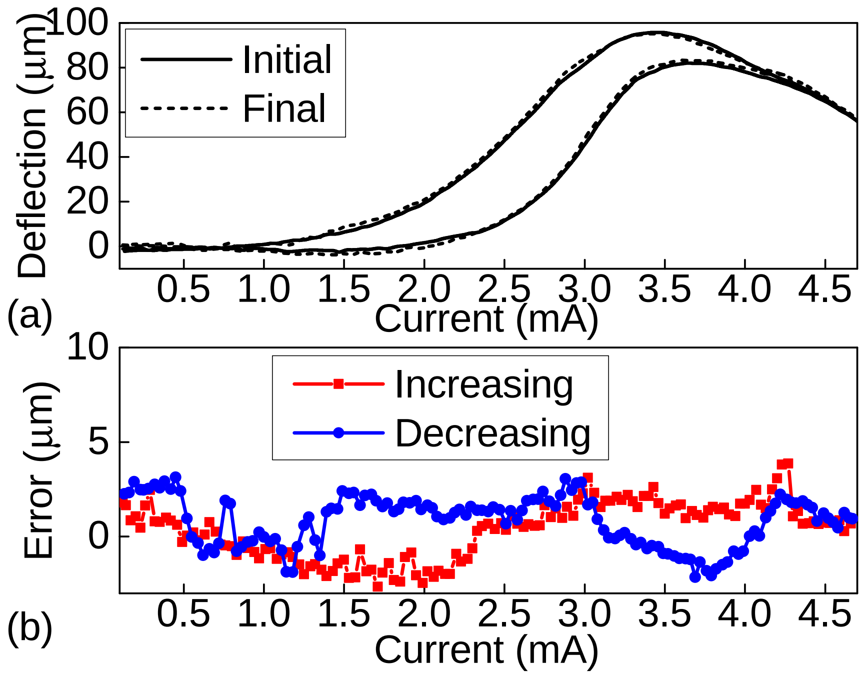

Figure 5.5: Reliability test results for the VO_2-based MEMS actuator. (a) Quasi-static deflection as a function of current before and after all the experiments. (b) Error between both curves for the increasing and decreasing current sweeps.

after the device was pulsed in open-loop for hundreds of thousands of cycles. **Figure** 5.5-(a) shows this quasi-static result along with the data of the experiment in **Figure** 5.2. **Figure** 5.5-(b) shows the error between the two quasi-static sweeps for both increasing and decreasing current plots. The error for the increasing sweep is between 3.8 and $-2.75\,\mu m$ with an average of $0.69\,\mu m$, and for the decreasing sweep is between 3.2 and $-2.25\,\mu m$ with an average of $1.2\,\mu m$. Both graphs are almost identical with differences probably due to random vibrations or other environmental noises, which shows that the VO_2-based MEMS actuator and the measurement setup can produce reliable and repeatable results even after hundreds of thousands of cycles with no noticeable degradation.

5.2.5 Rate Dependency

Rate-dependent hysteresis is produced by a phase lag between input and output signals as a result of the system dynamics. This phase lag in conjunction with the memory effect due to the hysteresis produces a change in the input-output relationship, which strongly depends on the frequency of the input. Although this mechanism has been observed in the past in micro-actuators [109–111], it has never been observed in VO_2-based actuators.

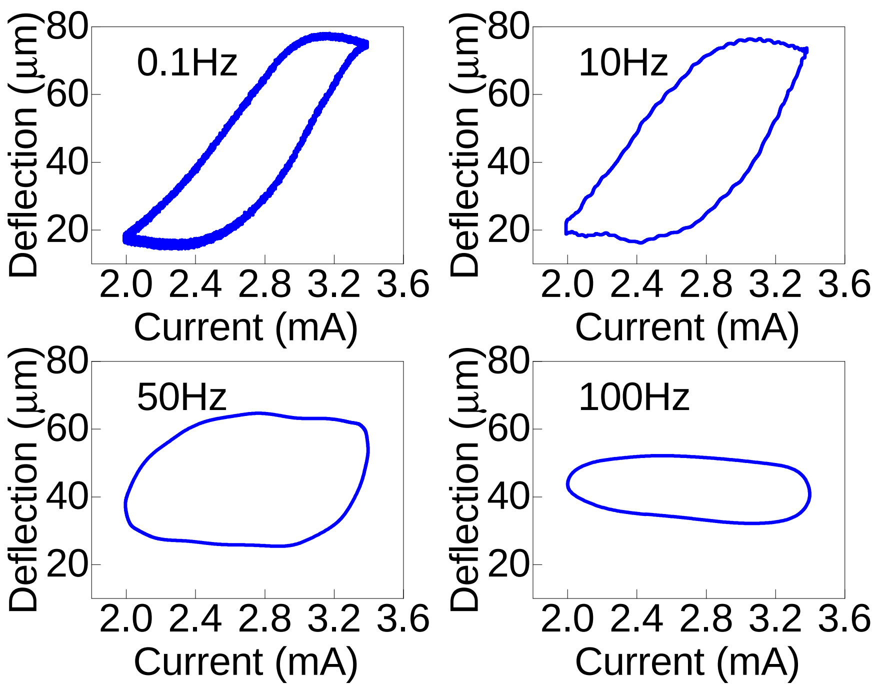

Figure 5.6: Deflection as a function of sinusoidal current input at different frequencies. The shape of the hysteresis is dependent on the actuation frequency showing the rate dependency of the micro-actuator.

To study this effect in the device used in this work, a sinusoidal current input was applied to the Pt heater in the actuator with amplitude of 0.68 mA and offset of 2.68 mA at different frequencies while measuring its deflection. The results for some of the frequencies are shown in **Figure** 5.6. The response at low frequencies (0.1 Hz) is similar to the quasi-static experiment results, but, as the frequency is increased, the output-input relationship starts changing. At 10 Hz the hysteresis is significantly wider although its amplitude seems unaffected, and at 50 Hz the amplitude has already decreased almost half of its original value while the hysteresis becomes even wider. From here and up to 100 Hz the amplitude continues to decrease while the hysteresis shape completely shifts to the other side — at low frequencies higher currents produced higher deflections while at higher frequencies lower currents produced higher deflections.

Hysteretic nonlinear models and control schemes, such as hysteresis compensation, would increase modeling accuracy, but, due to the complicated system dynamics and hysteresis behavior shown, this approach would be highly computationally intensive. In addition, the observed rate dependency must be considered in closed-loop control if incorporating hysteresis compensation schemes, which requires an even increased level of modeling and computational complexity. The control schemes needed to incorporate these effects would be outside the scope of the computationally efficient modeling and control techniques proposed in this work, which is aimed at demonstrating closed-loop control of VO_2-based MEMS actuators using PID control.

5.3 Modeling

Using the results obtained from the device quasi-static and dynamic characterizations, and after demonstrating device and setup reliability, the device can be modeled and controlled. Rather than utilizing complex modeling and control schemes, the proposed approach in this work is to show that VO_2-based MEMS actuators can be accurately controlled through a simple, yet effective PID controller.

5.3.1 Thermal Domain

The micro-actuator model in this work consists of a first-order transfer function representing the electro-mechanical component, which is derived from the experimental results in **Figure** 5.3, plus a second-order transfer function representing air drag and damped resonance, which is derived theoretically and validated through a FEM simulation. From the experimental results on frequency response as shown in **Figure** 5.3, it was observed that the micro-actuator can be modeled by a first order transfer function with a cut-off frequency determined by the thermal dynamics in the device. The general expression for a first order transfer function is:

$$A_{th}(s) = \frac{A_0}{\tau s + 1}, \tag{5.1}$$

where A_0 is the DC gain and τ is the time constant of the micro-actuator. In this work the gain at 0.1 Hz was assumed as the DC gain since it was orders of magnitude below f_c. The gain and time constant resulting from the fitted transfer function model in **Equation** (5.1) were 44.8 µm/mA and 3.8 ms, respectively. The plot shown in **Figure** 5.3 is the magnitude of the deflection, which is derived from **Equation** (5.1). The accuracy of the thermo-mechanical model can be seen in **Figure** 5.3, where it is plotted along with the obtained experimental data.

5.3.2 Mechanical Domain

To consider the effect of air damping and damped resonant frequency in the micro-actuator, a similar analytical procedure to the one done in [28] is employed, where the normalized transfer function of a damped harmonic oscillator is defined as:

$$A_{drag}(s) = \frac{\frac{k_{eff}}{m_{eff}+\beta_a}}{s^2 + \frac{\beta_v}{m_{eff}+\beta_a}s + \frac{k_{eff}}{m_{eff}+\beta_a}}, \tag{5.2}$$

where k_{eff} is the effective spring constant of the device obtained from [112, 113], m_{eff} is the effective mass ($m_{eff} = 33/144m$) where m is the actual cantilever mass calculated from the densities and volume of the materials, and β_a and β_v are the acceleration and velocity drag coefficients, respectively. These coefficients are defined as [114]:

$$\beta_v = 6\pi\eta R_s \left(1 + R_s\sqrt{\frac{\rho\omega}{2\eta}}\right), \tag{5.3}$$

$$\beta_a = \frac{2}{3}\pi\rho R_s^3 \left(1 + \frac{9}{2R_s}\sqrt{\frac{2\eta}{\rho\omega}}\right), \tag{5.4}$$

where ρ and η are the density and dynamic viscosity of the medium surrounding the micro-actuator, which in this case is air, R_s is the radius of the sphere used to model the micro-actuator following the procedure detailed in [115], and ω is the angular frequency. All of

Table 5.1: Derived values for modeling micro-actuator dynamics.

Parameter	Value
A_0 (µm/mA)	44.8
τ (ms)	3.8
R_s (µm)	95.5
k_{eff} (N/m)	0.0606
m_{eff} (kg)	3.25×10^{-11}

the material parameters used for the calculations are shown in **Table 4.1** and the derived coefficients are shown in **Table 5.1**. Although β_v and β_a are a function of ω, **Equation** (5.2) can be approximated by another second-order transfer function ($\hat{A}_{drag}(s)$) with coefficients obtained through a parameter fitting in order to approximate $A_{drag}(s)$ effectively with coefficients independent of ω. Here, $\hat{A}_{drag}(s)$ results in:

$$\hat{A}_{drag}(s) = \frac{\omega_n^2}{s^2 + 2\zeta\omega_n s + \omega_n^2}, \tag{5.5}$$

where ω_n is defined as the natural frequency of the micro-actuator, and ζ is defined as the damping ratio. The obtained values from the model fitting were $\omega_n = 39\,898.2\,\mathrm{rad/s}$ and $\zeta = 0.05$. To study the accuracy of the approximated model, the magnitude of **Equation** (5.2) and **Equation** (5.5) were compared where a maximum error of 0.1 % was observed through a frequency range from 0.1 Hz to 100 kHz. To further validate the approximated model, a natural frequency of 41 202 rad/s was obtained from a FEM eigenfrequency simulation of the micro-actuator using the material parameters in **Table 4.1**. The error between the analytically calculated angular frequency to that obtained from the simulation is 5 %. **Equation** (5.1) and **Equation** (5.5) can be multiplied to obtain the overall transfer function of the VO_2-based MEMS micro-actuator and substituting all of the parameters in the resulting transfer function yields:

$$A_{MA}(s) = \frac{1.8767 \times 10^{13}}{(s + 263.2)\left(s + 1.995 \times 10^3 \pm \jmath 3.985 \times 10^4\right)}, \tag{5.6}$$

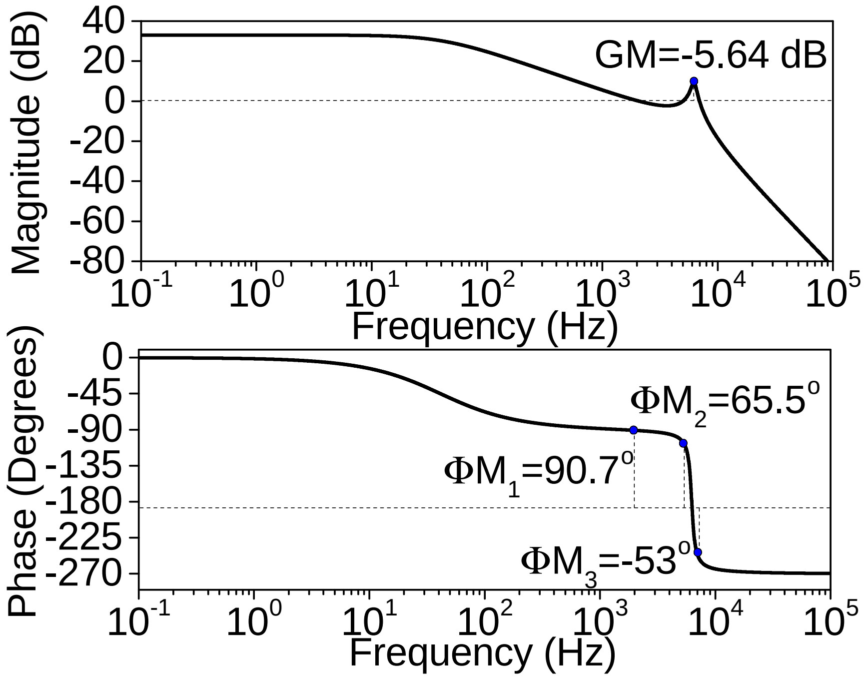

Figure 5.7: Bode plot for the simulated model of the VO_2-based MEMS micro-actuator under open-loop. The gain margin (GM) and phase margins (ΦM) are shown.

Figure 5.7 shows the bode plot (magnitude and phase) of the micro-actuator transfer function in **Equation** (5.6). The resulting system has a gain margin $GM = -5.64\,\mathrm{dB}$, which clearly states that the system would be closed-loop unstable for any proportional gain greater than 0.34. This limit is observed experimentally, although it shows at a slightly lower gain, probably due to the approximations used in the model. The system also has multiple crossover frequencies that result in three phase margins of $\Phi M = 90.7°$, $65.5°$, and $-53°$. Using this approximated model, which consisted of the experimentally identified thermo-mechanical model and the theoretically derived air drag and harmonic model, a PID controller can be designed and implemented for closed-loop control of the micro-actuator.

5.4 Controller Design

The closed-loop control diagram of the VO_2-based MEMS actuator is shown in **Figure** 5.8, where $G(s)$ is the transfer function of the micro-actuator dynamics, $K(s)$ is the transfer function of the controller used in this work, and f is the linear conversion from deflection setpoint to voltage (the inverse of f is the calibration result used to obtain the deflection using the voltage of the PSD in all experiments). The variable y_{ref} is the reference signal in micrometers, which is converted to a reference voltage $v_{ref}(t)$. The error e is the difference between v_{ref} and the output voltage of the PSD v. The current I_h is the same as defined before, but in this case is controlled by $K(s)$, whose goal is to minimize e ultimately controlling the VO_2 actuator deflection y while meeting specific performance requirements.

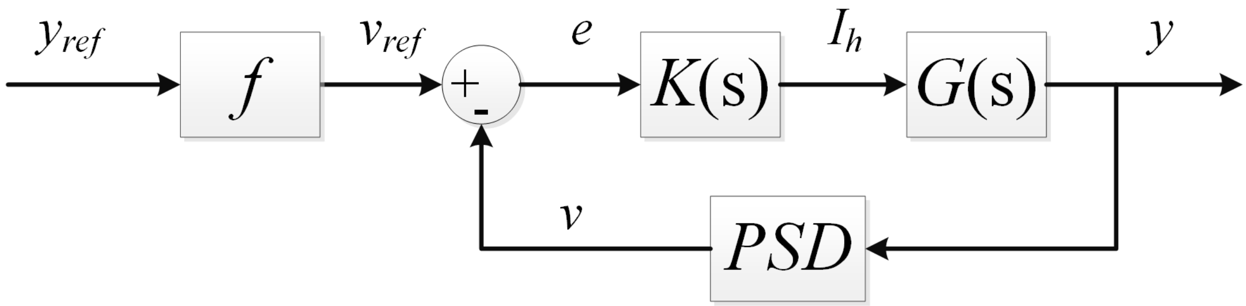

Figure 5.8: Closed-loop deflection control diagram for the VO_2-based MEMS actuator.

5.4.1 Design Specifications

The transfer function of the PID control derived through the Laplace transform is defined as:

$$K(s) = K_p + \frac{K_i}{s} + K_d s, \tag{5.7}$$

where K_p, K_i, and K_d are the proportional, integral and derivative gains of the controller, respectively. The values of these gains are chosen as to obtain a desired system performance in terms of frequency and transient response while ensuring zero steady-state error. In the process of obtaining the gains in this work it was noticed that the micro-actuator closed-loop response showed steady-state oscillations with frequency and amplitude strongly dependent on the controller gains. This effect has been observed in the past for hysteretic systems controlled in closed-loop and has been attributed to limit cycles produced by the hysteresis

Table 5.2: PID controller gains for the two controller designs.

Gain	PID_1	PID_2
K_p	0.105	0.28
K_i	11.66	93.31
K_d	1.05×10^{-4}	1.05×10^{-4}

[116–118]. Another observation is that the amplitude and frequency of limit cycles increase with increasing K_p [116], which is in accordance with what is observed in this work. As mentioned in [116], it is difficult to determine the effect of the controller gains in the limit cycle behavior through an analytical study, and thus, an experimental approach is used in order to determine a set of controller gains that reduce the limit cycles while accurately controlling the micro-actuator.

In this work, two PID controllers (PID_1 and PID_2), with bandwidths more than half a decade apart, are designed, implemented and compared. Bandwidths of $f_{c1} = 70\,\text{Hz}$ and $f_{c2} = 500\,\text{Hz}$ are chosen in order to stay well below the resonant frequency while achieving relatively fast actuation transients. In addition, a maximum overshoot of $1\,\%$ is required, which traduces to a phase margin of 173° for both controllers. This overshoot limit is chosen to show the applicability of this technology to micro-manipulation, where large deviations from the setpoint are undesirable. The gains for the resulting controllers are shown in **Table 5.2** and the controllers transfer functions are given by:

$$K_1(s) = \frac{1.05 \times 10^{-4}\,(s + 872.7)\,(s + 127.3)}{s}, \tag{5.8}$$

$$K_2(s) = \frac{1.05 \times 10^{-4}\,(s + 2276)\,(s + 390.4)}{s}. \tag{5.9}$$

5.4.2 Simulation

The resulting closed-loop transfer functions for the system in **Figure** 5.7 using both controllers are shown in **Figure** 5.9. It is observed that for the system with $K_1(s)$ the bandwidth and phase margin are 72 Hz and 173°, respectively, while for $K_2(s)$ these values are 496 Hz and 168.7°. These results show that both controllers meet the design requirements and will be used to study the VO_2-based MEMS actuator performance under closed-loop control. For implementing the closed-loop controller a sampling time of 10 μs was used, which is sufficient enough to ensure complete signal reconstruction.

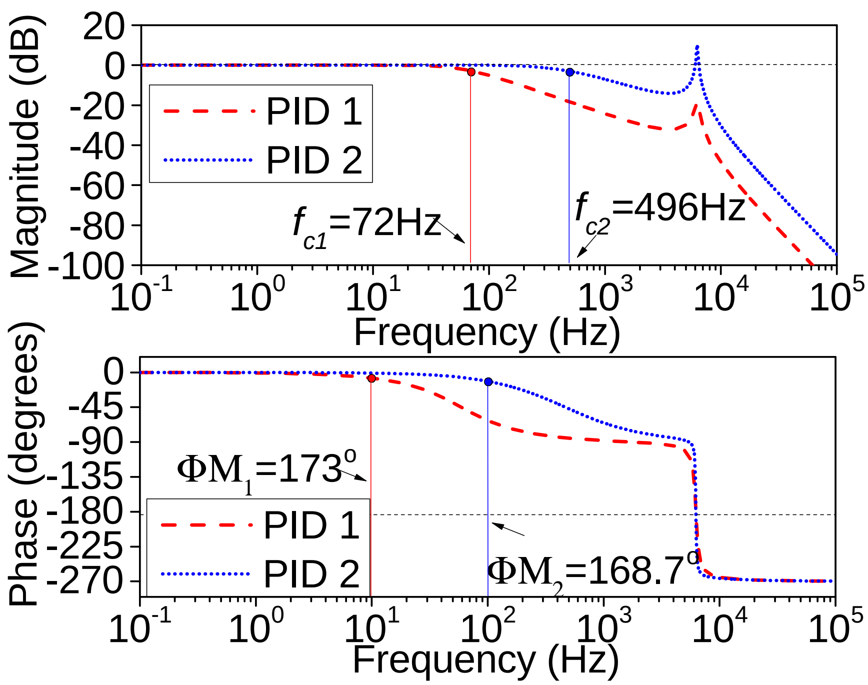

Figure 5.9: Closed-loop bode plots for the system in **Figure** 5.7 using the two PID controllers.

5.5 Results

To determine the performance of the PID controllers designed in the previous section, a series of tracking experiments are performed. A step reference tracking experiment is used to study the transient characteristics of the closed-loop system and the effect of the controller gains in the limit cycles. Another experiment is performed in order to study the tracking performance of the system under sinusoidal-modulated reference signal at different frequencies. Finally, a comparison between open-loop and closed-loop control of the micro-actuator under temperature disturbance is done to demonstrate the need of accurate closed-loop control.

5.5.1 Step Reference Response

In this experiment, a total of six increasing and decreasing steps were applied to the input of the system in order to study the transient and steady-state performance of the micro-actuator. Each step size was 21 µm with duration of 0.5 s and the total controlled range was 65 µm. **Figure** 5.10-(a) shows the setpoint and measured deflection of the micro-actuator as a function of time under PID_1. It is observed that the deflection of the device follows the desired deflection path effectively and the deflection is maintained during steady-state. The inset in **Figure** 5.10-(a) shows the transient of the deflection signal, characterized by a time constant of 2.42 ms, which is close to the 2.2 ms approximated from the model and simulated controller. In addition, no overshoot was observed in the signal as require by the design specifications.

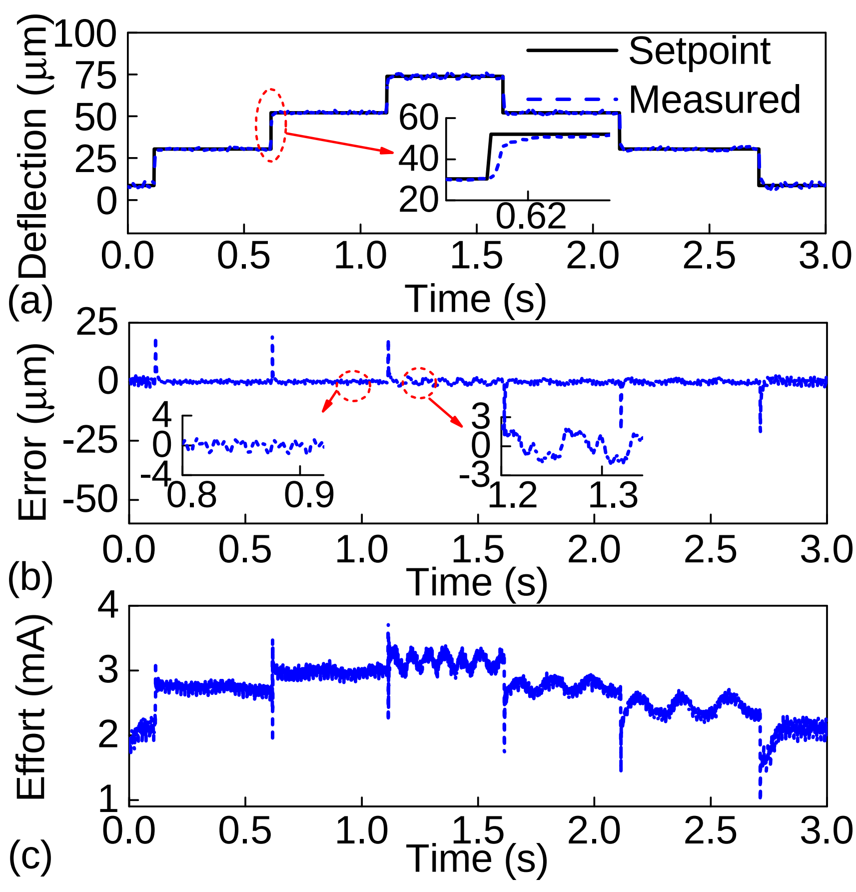

Figure 5.10: Results for the micro-actuator under PID_1 control. (a) Deflection, (b) deflection error, and (c) controller effort of the step reference tracking experiment.

The error of the signal, in µm, is shown in **Figure** 5.10-(b) where the average steady-state error observed was zero, due to the integral part of the PID. The insets on this plot show evidence of the steady-state limit cycles produced by the hysteresis. It is observed that the peak-peak error is setpoint-dependent with a maximum of 3.8 µm. In addition to the error amplitude, the error frequency is also observed to be setpoint-dependent. These dependencies with setpoint values are thought to be due to the non-monotonic and asymmetric hysteresis observed in **Figure** 5.2, which changes the shape of the resulting limit cycles. These effects can also be noticed in the control effort shown in **Figure** 5.10-(c) where an interesting feature is the difference in effort amplitude and frequency between increasing and decreasing setpoints for the same deflection value.

Figure 5.11 shows the step reference tracking results using PID_2. The first difference to notice between the deflection performance in **Figure** 5.11-(a) and **Figure** 5.10-(a) is the noisier signal of the former, which is produced by the higher bandwidth (higher K_p) obtained with PID_2. The second difference is the faster transient times obtained with PID_2, which results in a time constant of 0.34 ms, although higher transient oscillations are observed since K_p in this controller is closer to the stability maximum. A third difference for PID_2 is the amplitude and frequency of the steady-state oscillations observed in the deflection error in **Figure** 5.11-(b).

Although the average steady-state error is zero, similar to the results with PID_1, the maximum peak-peak error is 5.75 µm, which is 1.5× larger than with PID_2. In addition, the frequencies of these oscillations seem to have increased with PID_2. These results are in agreement with previous observations were the frequency and amplitude of the steady-state limit cycles increase with increasing K_p [116]. The effect of the higher gains is also observed in the controller effort in **Figure** 5.11-(c), which is substantially higher than with PID_1. These results show that closed-loop control of VO_2-based MEMS actuators can achieve fast transient responses while minimizing deflection overshoot and average steady-state error. Depending on the performance specifications, different controllers can be designed and implemented to

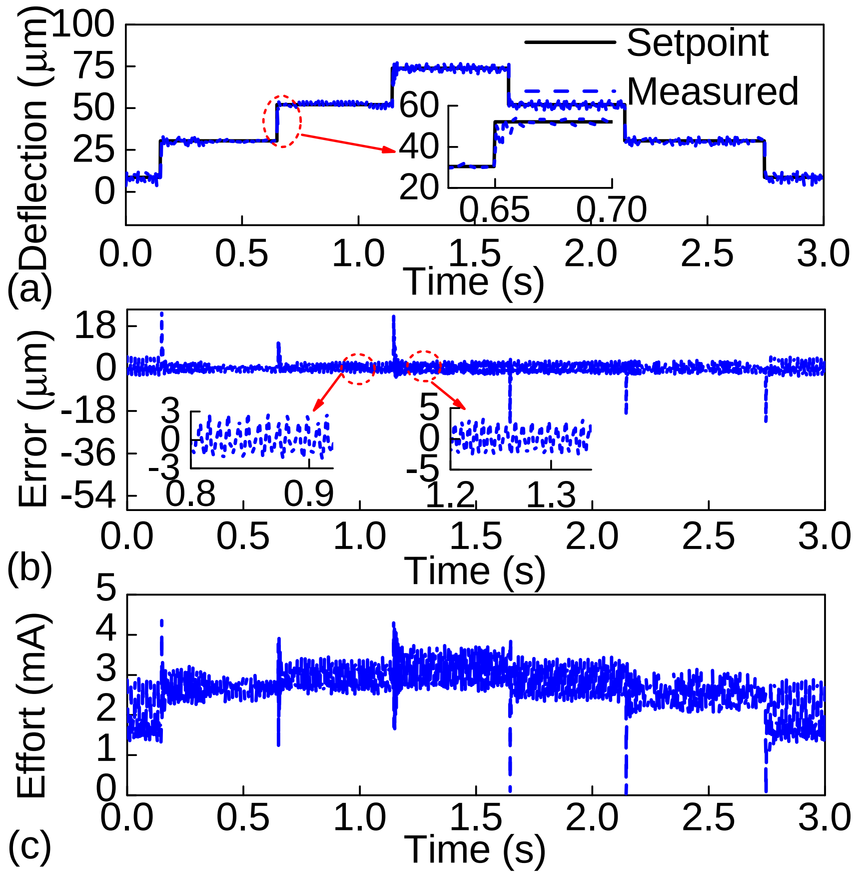

Figure 5.11: Results for the micro-actuator under PID_2 control. (a) Deflection, (b) deflection error, and (c) controller effort of the step reference tracking experiment.

take advantage of the large displacements produced by these actuators.

5.5.2 Sinusoidal Tracking Response

In some cases, micro-actuators are operated under time varying reference inputs, such as sinusoidal signals. To study the frequency performance of the micro-actuator under PID control using using both controllers designed in this work, the frequency of a sinusoidal reference input is varied across a large deflection range while the deflection is been monitored. The amplitude and offset of the reference signal are 25 µm and 35 µm, respectively. **Figure** 5.12 shows the results obtained in this experiment using PID_1 up to a frequency of 10 Hz at which the response has a phase lag of approximately 8.3°. This phase lag is in agreement with the model and PID predictions observed in the bode plots in **Figure** 5.9. The results also

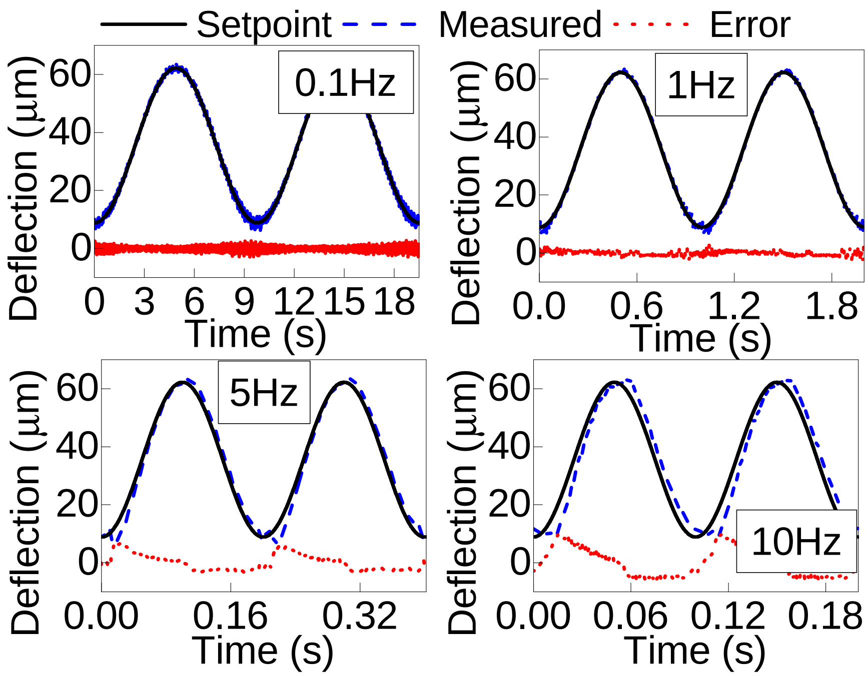

Figure 5.12: Sinusoidal reference tracking results at different frequencies for the micro-actuator under PID_1 control.

show the effective control of the micro-actuator throughout the frequencies studied. One observable trend is that the error at the sinusoidal peaks tends to increase for increasing frequencies. This might be due, not only to the phase lag, but also to the non-monotonic deflection, as can be seen from the measured deflection signals near the sinusoidal peaks.

Figure 5.13 shows the results of the sinusoidal tracking experiment with the PID_2 controller. These results show a better performance of the micro-actuator at higher frequencies, which results in smaller errors, while higher errors are observed at lower frequencies, possibly due to the higher proportional gain. The deflection of the micro-actuator accurately tracks the desired deflection up to 50 Hz with almost no phase lag. These results are again validated by the frequency response of the simulated system and controller in **Figure** 5.9. Similar to the response under PID_1, the non-monotonic behavior of the micro-actuator is noticeable at the sinusoidal peaks.

In order to compare both results in terms of deflection error, the root-mean-square error

(RMSE) is calculated. The RMSE in this work is defined by:

$$RMSE = \sqrt{\frac{\sum_{n=1}^{N} e\,(n)^2}{N}} \tag{5.10}$$

where e is the error calculated from the difference of desired and measured deflection, and N is the number of elements in e. **Figure** 5.14 shows the RMSE as a function of frequency calculated from the sinusoidal tracking experiments for the system under PID$_1$ and PID$_2$ control. At low frequencies the RMSE under PID$_1$ is significantly lower than the RMSE under PID$_2$, but as the frequency is increased, the RMSE under PID$_1$ increases exponentially whereas the RMSE under PID$_2$ has a much gradual linear slope. This effect is likely due to the higher bandwidth of PID$_2$, although the larger RMSE observed for PID$_2$ at lower frequencies might be due to the higher amplitude for the limit cycles in this case.

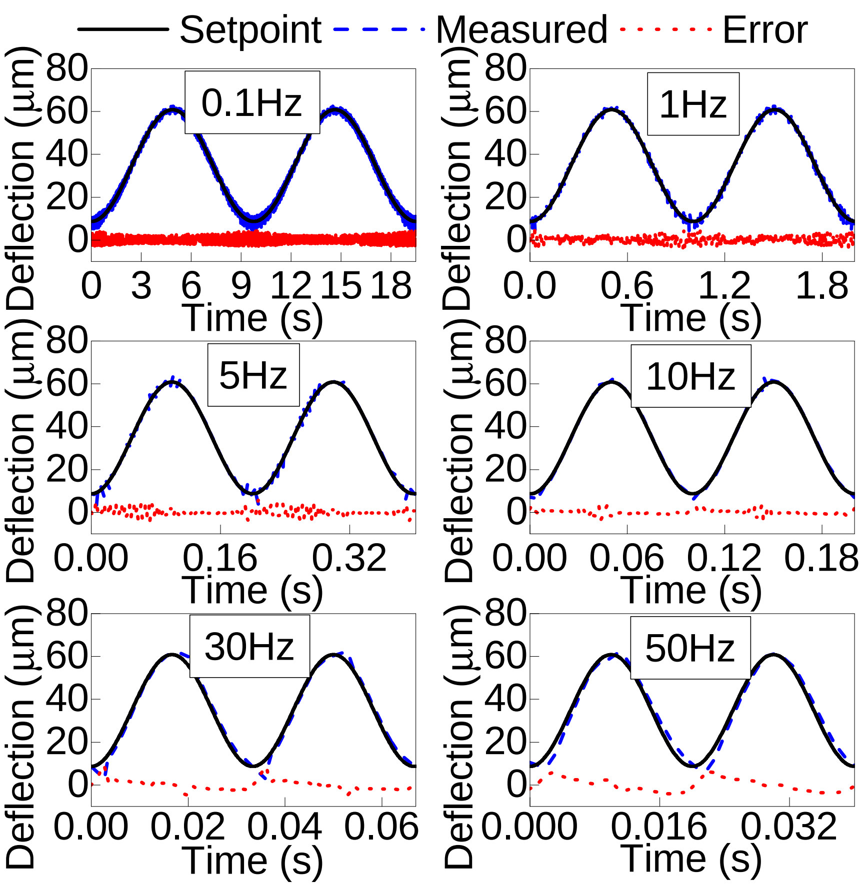

Figure 5.13: Sinusoidal reference tracking results at different frequencies for the micro-actuator under PID$_2$ control.

5.5.3 Open- vs Closed-loop Control

In this experiment, a Peltier heater was placed directly underneath the microactuator chip in order to simulate temperature disturbances. The temperature was controlled in closed-loop and temperature steps where given to the Peltier while the deflection of the micro-actuator, the current passing through the Pt integrated heater and the temperature at the sample were being monitored. **Figure** 5.15-(a-c) shows the deflection, heater current and temperature as a function of time with the micro-actuator under open-loop — constant current — and closed-loop control — constant deflection reference of 35 µm. Note that for the closed-loop control the PID_1 controller was used. The results show an evident superiority of closed-loop for controlling the deflection in temperature variant environments. Through the 20 °C temperature change, the deflection under open-loop underwent a change of 45 µm, which is undesirable for real-life applications. By using closed-loop control, the system was able to maintain the 35 µm deflection throughout the complete temperature disturbance range.

To further show the capabilities of the closed-loop controlled micro-actuator, a sinusoidal

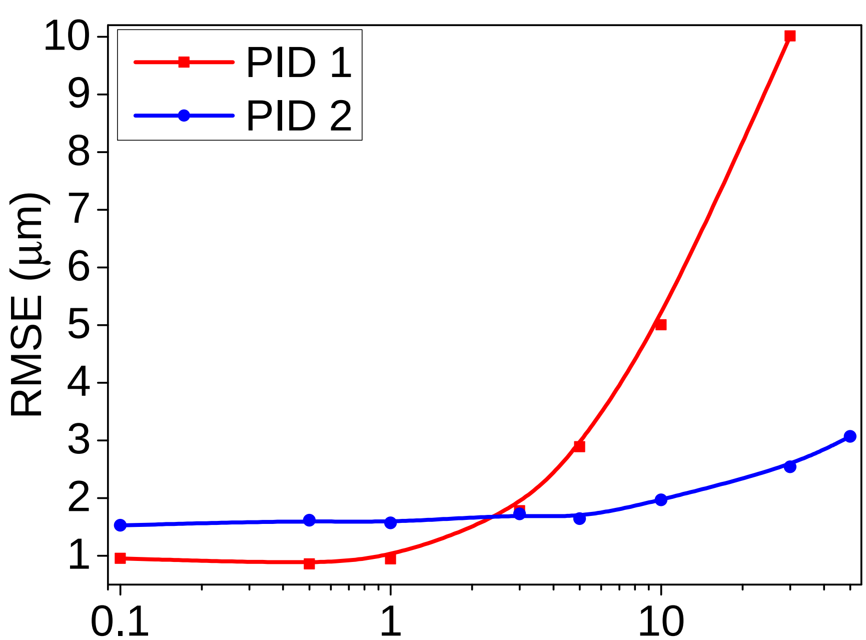

Figure 5.14: RMSE as a function of frequency obtained from the sinusoidal reference tracking experiment under PID_1 and PID_2 control.

tracking reference input with a frequency of 0.1 Hz was applied to the system while the sample temperature was varied. **Figure** 5.16-(a-c) show the effectiveness of the control system throughout the complete actuation range even with a temperature disturbance of more than 15 °C. As long as the sample temperature does not exceed the temperature required to maintain the micro-actuator at a desired deflection, the controller would supply the required current to maintain such deflection.

5.6 Summary

In this chapter, the characterization and implementation of a closed-loop system comprising a VO_2-based MEMS actuator with an integrated heater have been developed in order to

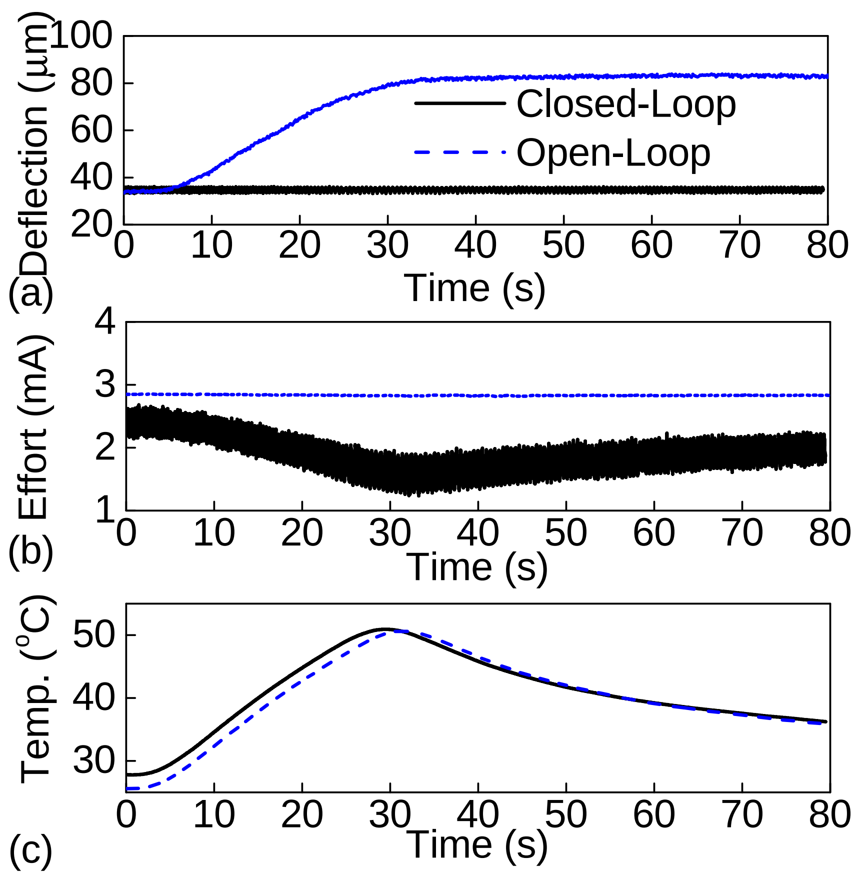

Figure 5.15: Open-loop vs closed-loop control. (a) Micro-actuator deflection, (b) Pt heater current, and (c) temperature measured during the temperature dependent experiment.

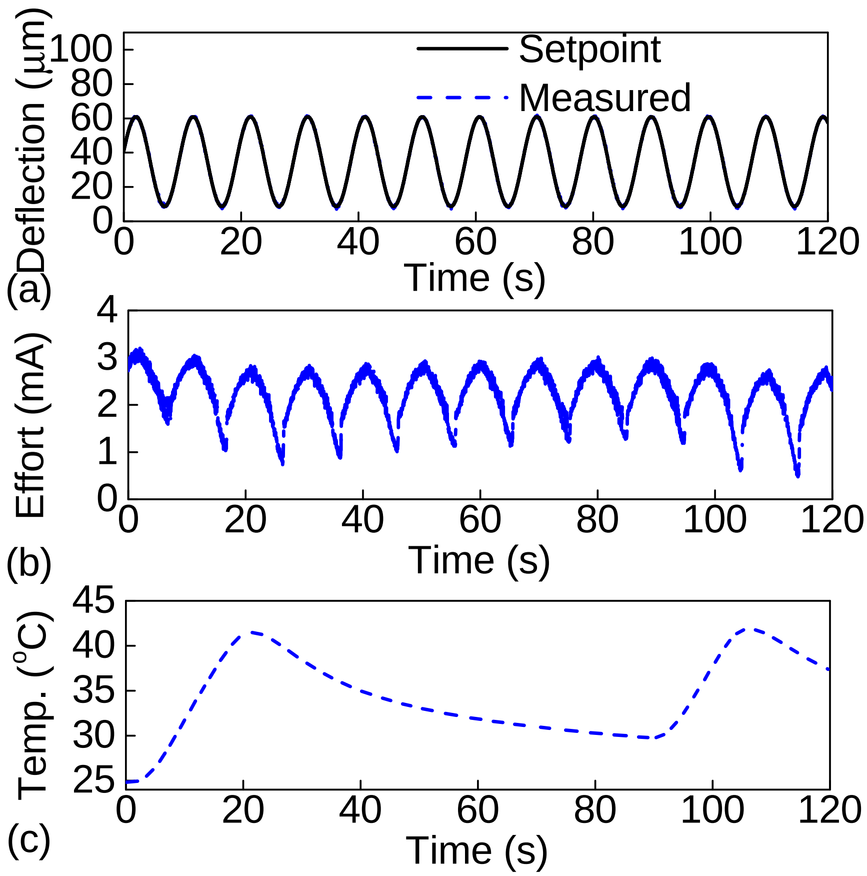

Figure 5.16: Closed-loop control of sinusoidal reference tracking at 0.1 Hz under temperature disturbance. The different plots show the (a) Micro-actuator deflection, (b) Pt heater current, and (c) temperature measured during the experiment.

accurately control the large deflections produced by these devices through the use of Joule heating. A comprehensive characterization and modeling of the micro-actuator was performed and used to tune two PID controllers whose performance were compared through step reference, and sinusoidal reference tracking experiments. Finally, a temperature disturbance experiment was performed in order to show the advantages of closed-loop control over open-loop actuation. All of these results showed that VO_2-based MEMS actuators can be used for highly precise micro-manipulation and micro-positioning applications in temperature varying environments while achieving fast actuation, no overshoot and minimizing the deflection error.

CHAPTER 6
SELF-SENSING FEEDBACK

The work in this chapter shows a closed-loop controlled MEMS-based actuator with an integrated heater and sensor, which uses a self-sensing approach that drastically reduces the measurement hysteresis throughout the complete actuation range. Self-sensing is achieved by estimating the actual deflection through a resistance-to-deflection Boltzmann model obtained after a parameter fitting using simultaneous *in situ* VO_2 resistance and deflection measurements. The estimated deflection is then used in feedback with a proportional-integral (PI) controller in order to accurately control the MEMS actuator. For this experiment, a different sample from the one used in the experiments in **Chapter 5**. Hence, there are some differences in the characterization parameters, such as maximum tip displacement, open-loop cut-off frequency, and gains.

6.1 Measurement Setup

The IC package containing the VO_2-MEMS actuator fabricated in **Chapter 4** is placed on the measurement setup shown in **Figure** 6.1 in order to perform the simultaneous *in situ* VO_2 resistance and deflection measurements used in the characterization and control of the device using self-sensing. For deflection measurements, a sensing laser ($\lambda = 808\,\mathrm{nm}$) is focused at the tip of the cantilever and the reflected light is aimed at a position sensitive detector (PSD). The output of the PSD is a voltage (V_d) proportional to the position of the incident light in the active area. Using side view images from a charge-couple device (CCD) camera at different actuation values, V_d is calibrated to actual deflection (D_r). For VO_2 resistance measurements, a constant current of $15\,\mu\mathrm{A}$ is applied to the VO_2 through the two middle Pt electrodes (green dashed lines) while the voltage is being measured. This current value is chosen to avoid self-heating of the VO_2 while obtaining high signal-to-noise

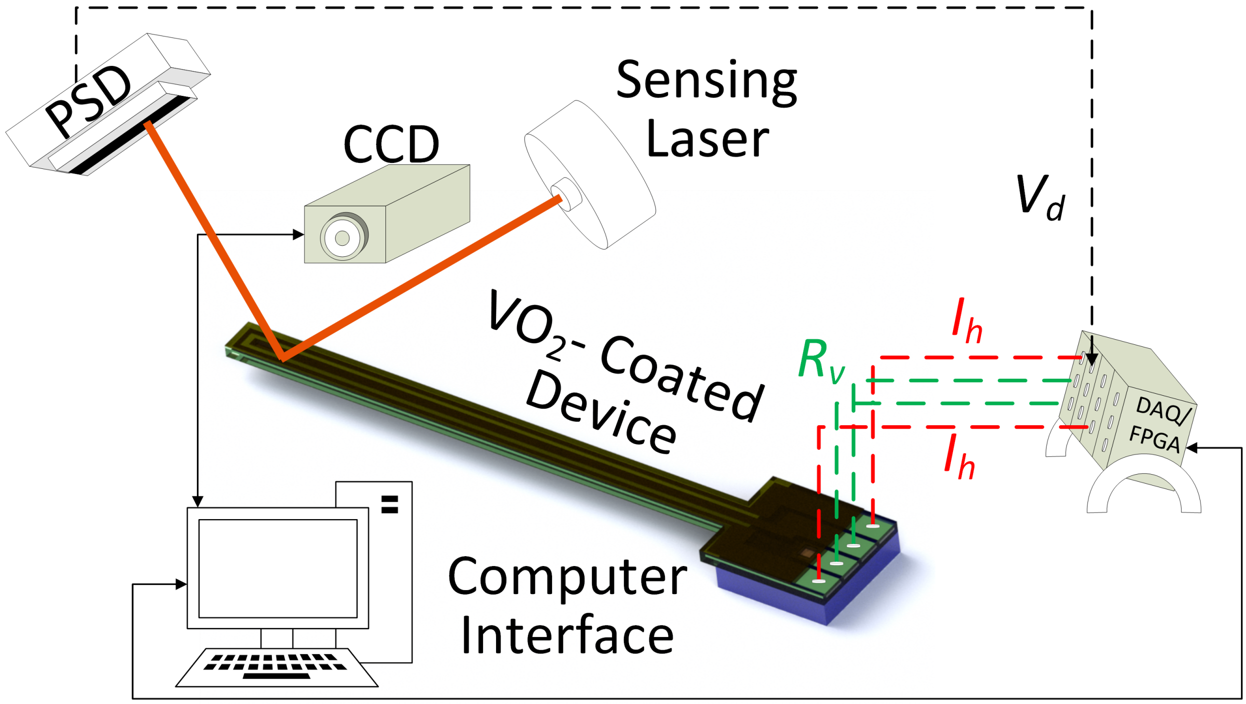

Figure 6.1: Measurement setup for performing the characterization and control experiments on the actuator. The setup is capable of *in situ* resistance and deflection measurements.

ratio. This was verified by measuring the deflection of the actuator with and without the sensing current. Since both deflection values were the same, it was concluded there was no self-heating of the VO_2. By using Ohm's Law, the VO_2 resistance (R_v) is then calculated. A data acquisition system and field programmable gate array (DAQ/FPGA) supplies the actuation signal (I_h) to the Pt heater (red dashed lines) and measures the corresponding voltage input signals and converts them to R_v and D_r. The DAQ/FPGA can be configured to operate either in open- or closed-loop using a computer interface.

6.2 Simultaneous *in situ* Resistance and Deflection Characterization

The electro-mechanical measurement setup in **Figure** 6.1 it used to perform simultaneous *in situ* resistance and deflection measurements of the VO_2 MEMS actuator. Quasi-static

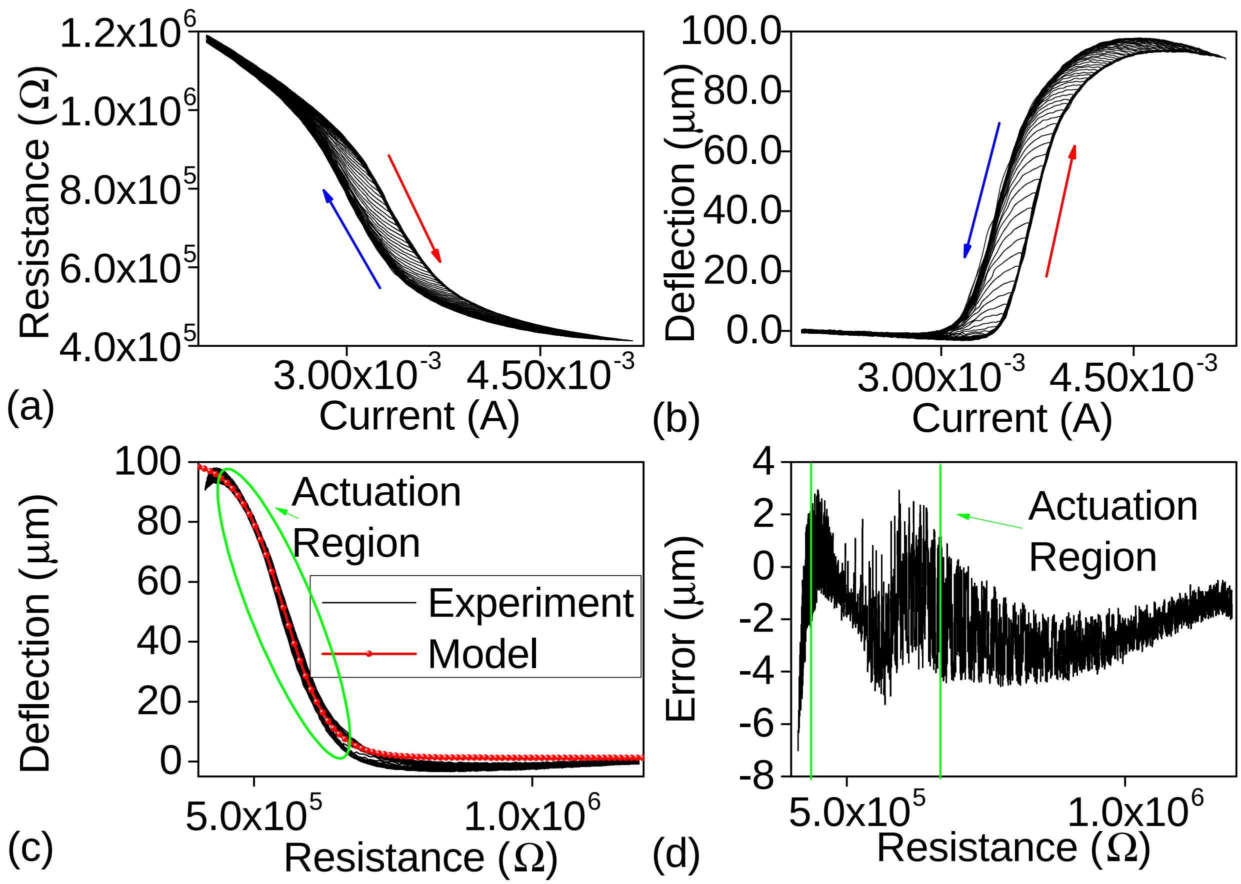

Figure 6.2: Quasi-static results for self-sensing model. (a) VO_2 resistance and (b) MEMS actuator deflection as a function of heater current. (c) MEMS actuator deflection as a function of VO_2 resistance and Boltzmann model used with the corresponding parameters. (d) Self-sensing modeling error as a function of VO_2 resistance.

and dynamic response analysis are performed in order to determine the self-sensing model and the PID controller gains. The procedure adopted in this section is similar to the one in **Section 5.2** with the added resistance measurements.

6.2.1 Quasi-static Analysis

The measurement setup is used to obtain quasi-static simultaneous R_v and D_r curves as a function of I_h, which are shown in **Figure** 6.2-(a-b). For this experiment, a series of decreasing first order reversal curves are obtained in order to cover the hysteresis minor loops. The current range for the complete experiment is from 1.8 to 5.2 mA in steps of

30 µA. To ensure R_v and D_r have reached steady state values, a wait time of 4 s is selected between each current setpoint. The VO_2 resistance shows the typical nonlinear hysteretic behavior observed in similar deposited films on SiO_2 with a maximum resistance change of $8 \times 10^5\,\Omega$ [25]. The deflection range obtained with the actuator is 95 µm, which is obtained through less than 1 mA change in I_h. There are two competing mechanisms that affect the deflection of the device: the structural phase transition of the VO_2 layer and the differential thermal expansion. The former is responsible for the large positive change in deflection from 3 to 4.5 mA, while the latter is responsible for the small negative changes at both ends. This nonmonotonic behavior has been observed in the past and a detailed discussion is given in [14, 31] and in **Section 3.1**.

6.2.2 Frequency Response

The setup in **Figure** 6.1 is used to obtain the open-loop magnitude frequency response of the micro-actuator under a sinusoidal input signal. The input frequency is varied from 0.1 to 200 Hz with a constant magnitude and offset of 0.4 mA and 3.6 mA, respectively. This values are chosen in order to include large part of the transition region in the deflection (see **Figure** 6.2-(b)). **Figure** 6.3 shows the I_h to D_r and the I_h to R_v gains as a function of frequency for the micro-actuator. The cut-off frequencies for both signals are very close to each other, which is expected since the dynamics in these types of thermally-actuated devices is dominated by thermal dissipation through the anchor and the surrounding media [25].

6.3 Modeling

Using the results from the quasi-static and frequency response experiments, the micro-actuator and the self-sensing models can be determined. A transfer function that fits the experimental resistance dynamic data is found. For self-sensing, the goal is to find a simple and effective non-hysteretic resistance-to-deflection model for implementation in an FPGA

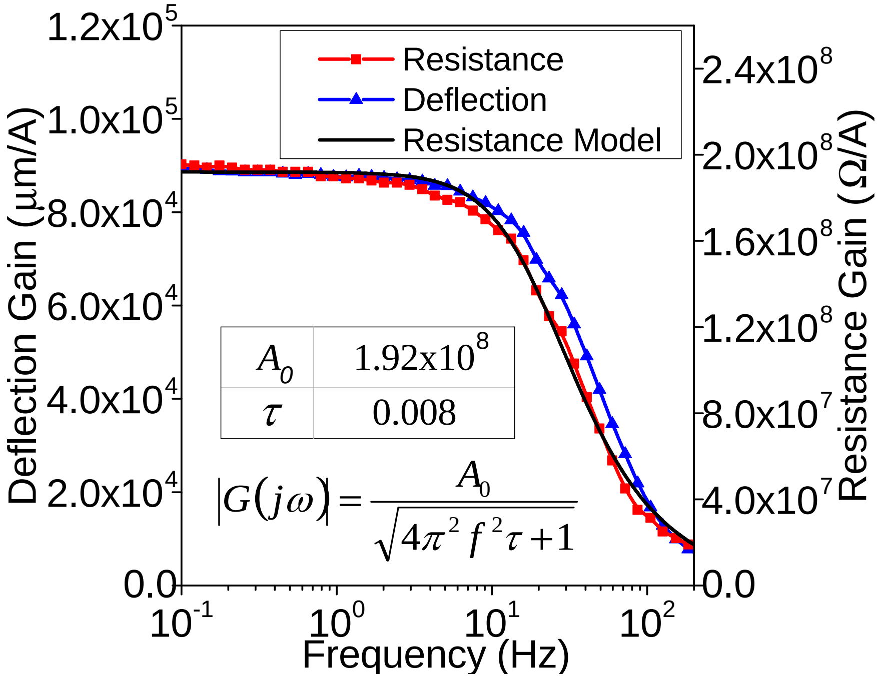

Figure 6.3: VO_2 resistance and deflection gains as a function of frequency under open-loop sinusoidal actuation obtained experimentally. The resistance gain is also modeled by a first-order transfer function with parameters shown in the inset table.

system.

6.3.1 Self-sensing Static Model

Figure 6.2-(c) shows the self-sensing relationship between deflection and VO_2 resistance for the same experimental data. The hysteresis is greatly reduced due to the highly coupled mechanisms responsible for the electrical — product of the insulator-to-metal transition (IMT) [20] — and the mechanical changes — resulting from the structural phase transition (SPT) [22] — in the VO_2. During the transition, the crystal structure changes and the vanadium ions are reordered, which causes a change in the VO_2 bandgap. This produces a strain change in a highly oriented VO_2 film. A Boltzmann function is then used to model the self-sensing relationship. The Boltzmann function is defined by

$$\hat{D}_r = \frac{A_1 - A_2}{1 + \exp\left(R_v - x_0\right)/dx} + A_2, \tag{6.1}$$

where A_1, A_2, x_0 and dx are the model parameters, which are obtained through a nonlinear model fit using a conjugated gradient method, and $\hat{D}_r$ is the estimated deflection. The model parameters obtained from the fitting are $A_1 = 100.72$, $A_2 = 1.2264$, $x_0 = 553170$, and $x_0 = 40840$. Note that the operational region is defined as the region through which the positive deflection (VO_2 transition) occurs in the actuator. **Figure** 6.2-(d) shows the error between the experimental data and the model in **Equation** (6.1). The maximum absolute error produced by the self-sensing model is 5 µm with an average error of −1.1 µm, throughout the complete actuation range of 95 µm. These results show that **Equation** (6.1) can accurately estimate D_r and can be used as the feedback signal to control the device deflection.

6.3.2 Actuator Resistance Dynamics

Both frequency responses, resistance and deflection, resemble the behavior of a first-order system. Since drag and internal mechanic dynamic effects are known to take place at much higher frequencies — more than an order of magnitude higher than the thermal cut-off frequency (see **Section 5.3.2** — they were not studied in this work. Since $\hat{D}_r$ will be used instead of D_r for control, the resistance gain is modeled by a first-order transfer function defined here as:

$$G(s) = \frac{A_0}{\tau s + 1}, \tag{6.2}$$

where A_0 is the resistance DC gain, and τ is the time constant of the system. Notice that the transfer function in this experiment is defined differently than in **Section 5.3.1**. In order to find the parameters for the system using the experimental results, the magnitude of **Equation** (6.2) is calculated by finding $|G(j\omega)|$ and then fitted with the data. Note that $\omega = 2\pi f$ where f is the frequency in Hz. The resulting model is also shown in **Figure** 6.3.

6.4 Controller Design

The self-sensing and dynamic system models are now used to determine a set of PI gains that will result in an accurate and controlled D_r using $\hat{D}_r$. **Figure** 6.4-(a) shows the high-level block diagram representation of the micro-actuator system. The controller uses $\hat{D}_r$ (calculated from the self-sensing model using R_v) and the reference deflection value D_{ref} to supply I_h (the control signal) in order to drive the VO_2-MEMS device. Note that D_r is only used to validate the performance of the self-sensing closed-loop system. An expanded view of the self-sensing closed-loop system is shown in **Figure** 6.4-(b), where e is the error between D_{ref} and $\hat{D}_r$, $K(s)$ is the PI controller transfer function, $G(s)$ is the resistance transfer function from **Equation** (6.2) and $\hat{D}_v(R_v)$ is the self-sensing model from **Equation**

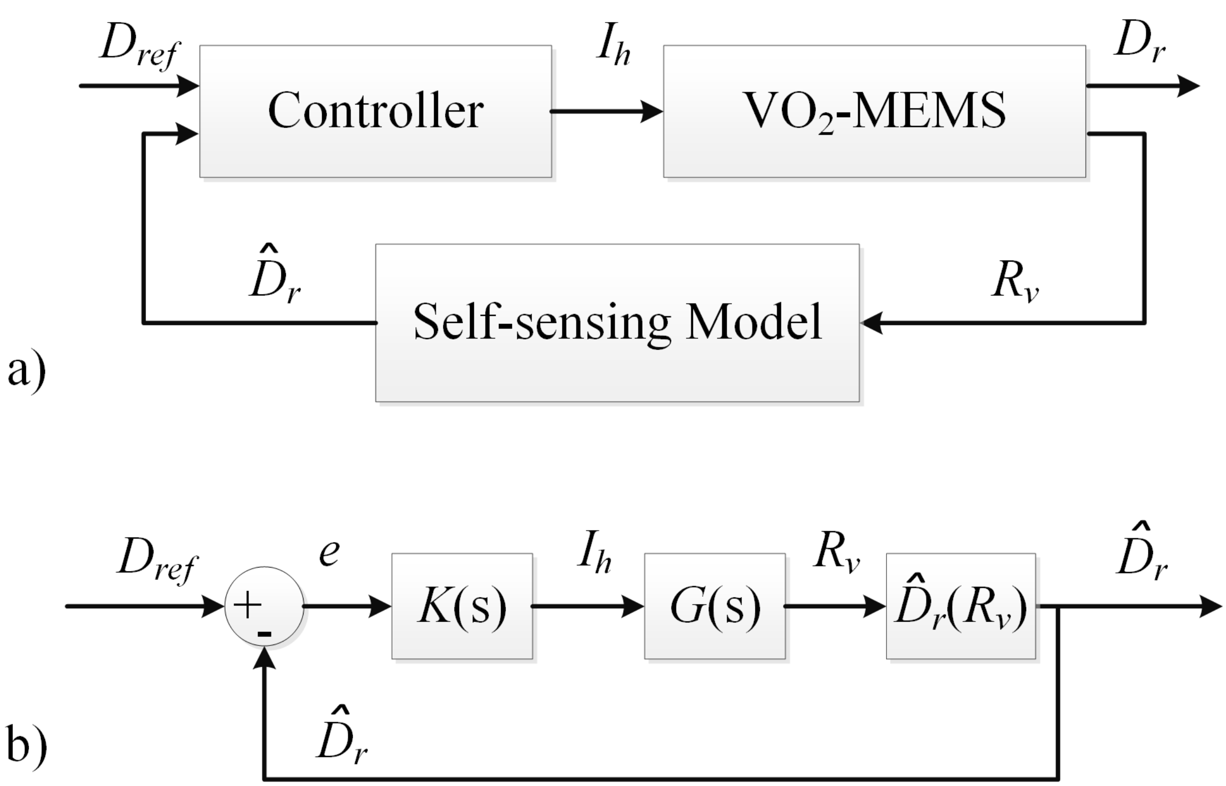

Figure 6.4: (a) Simplified high-level and (b) expanded dynamic closed-loop block diagrams of the VO_2-MEMS actuator using self-sensing.

(6.1). $K(s)$ is defined as

$$K(s) = K_p + \frac{K_i}{s}, \tag{6.3}$$

where K_p and K_i are the proportional and integral gains, respectively. Note that **Equation** (6.3) is **Equation** (5.7) without the derivative gain. Since the deflection and resistance open-loop responses have very similar performance in terms of cut-off frequency, a controller designed to compensate $\hat{D}_r$ should also compensate D_r with similar closed-loop performance. Hence, **Equation** (6.3) was designed to control the system in **Figure** 6.4-(b) in order to achieve a bandwidth (BW) of at least 40 Hz (which is double the open-loop bandwidth), and a percent overshoot of less than 10 % (which traduces to a phase margin (ΦM) of less than 121°). The obtained gains based on these specifications are $K_p = 0.07$ and $K_i = 87.5$ and the simulated performance of the closed-loop system using these gains is shown in **Figure** 6.5-(a-b).

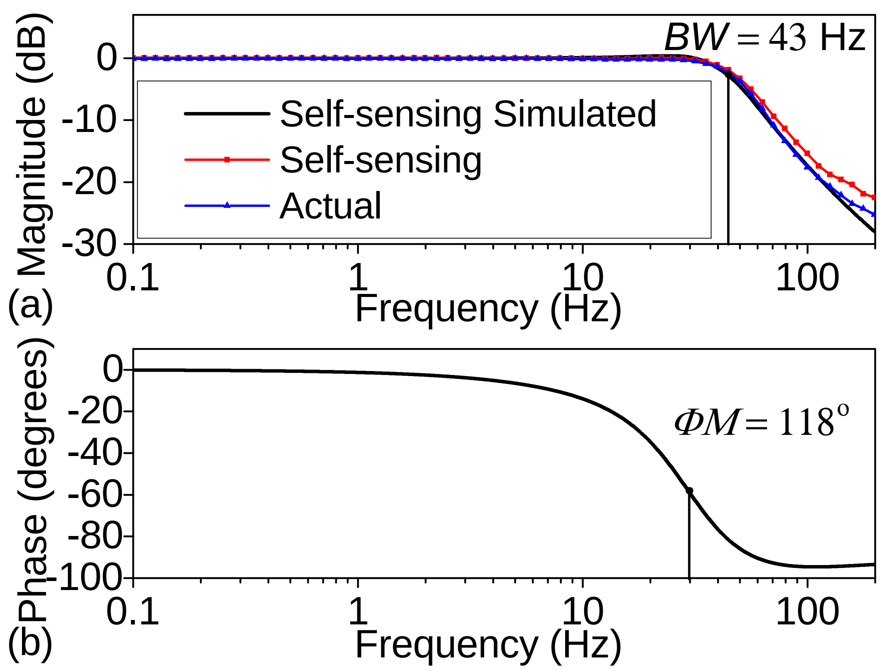

Figure 6.5: Experimental and simulated (a) magnitude and (b) phase as a function of frequency of the closed-loop controlled VO_2-based MEMS actuator.

6.5 Results

To test the performance of the micro-actuator system, a series of reference tracking experiments are performed. First, the closed-loop frequency response is obtained experimentally by applying a sinusoidal reference signal with varying frequency. Second, a step reference input response is performed in order to obtain the transient performance of the system and study the overall system accuracy. More emphasis is given to the actual deflection (D_r) in the result discussions since, in practice, its performance is of most value. However, the estimated deflection ($\hat{D}_r$) is also included to show the effectiveness of the self-sensing feedback method.

6.5.1 Closed-loop Frequency Response

To experimentally obtain the closed-loop frequency response of the micro-actuator, D_{ref} was chosen as a sinusoidal wave of varying frequency from 0.1 to 200 Hz with a magnitude and offset of 30 µm and 45 µm, respectively. **Figure** 6.5-(a) shows the magnitude gain in decibels of the closed-loop system for the mentioned input conditions. Both self-sensed and actual deflection gains follow the simulated results closely with a BW of 43 Hz.

The effectiveness of the self-sensing model is also verified by the unnoticeable difference between the self-sensing and actual deflection performances before the ΦM (0 dB) frequency of 30 Hz. The maximum difference between D_r and $\hat{D}_r$ is 0.255 dB or 1.8 µm through the deflection range of 60 µm tested in this experiment. In addition, maximum actual and self-sensing errors to that of the setpoint are 0.19 dB (1.32 µm) and 0.015 dB (0.1 µm), respectively.

To further show the frequency and time dependent performance of the micro-actuator, some of the deflection sinusoidal responses used to obtain the results in **Figure** 6.5-(a) as a function of time at different frequencies are shown in **Figure** 6.6. One noticeable trend is the increased difference between the actual and setpoint deflection values right after the

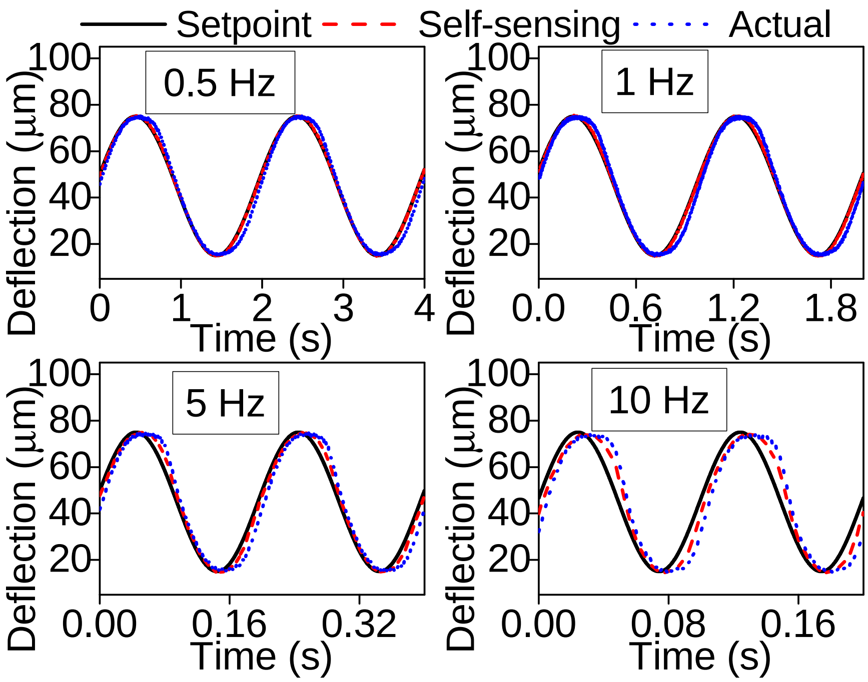

Figure 6.6: Sinusoidal time dependent deflection response for the self-sensing and actual values at different frequencies.

maximum and minimum setpoint peaks. Hence, it is difficult to obtain a measure of the phase difference, since the phase value varies when calculated at different locations within a period. For example, at 10 Hz the phase difference is 22° if calculated at the sinusoidal offset value or 30° if calculated at the maximum value. One plausible explanation is the asymmetry of the hysteretic curve. The actuation region for this particular frequency response experiment — which is smaller than the actuation region used for the quasi-static experiments shown in **Figure** 6.2-(c) — includes a hysteretic region that is non-symmetric. This non-symmetry (which is not modeled by **Equation** (6.1)) changes the shape of the limiting cycles in the actuation region; causing pronounced differences between the estimated and actual deflection when cycling between setpoint peaks. This has been observed in a previous sinusoidal control experiment performed by the authors, where the actual deflection was directly controlled [29].

6.5.2 Step Reference Response

D_{ref} was chosen as two sequences of varying step inputs with duration of 200 ms each in order to study the transient and steady-state errors of the closed-loop controlled VO_2-MEMS actuator. The first sequence was designed to cover one stable hysteresis loop (increasing and then decreasing staircase cycle), while the second sequence was designed to study the performance throughout the hysteresis (arbitrary increasing and decreasing steps). The results for the first and second sequences are shown in **Figure** 6.7-(a-b), respectively. Both figures also show inset plots of some step regions in order to show transient behavior.

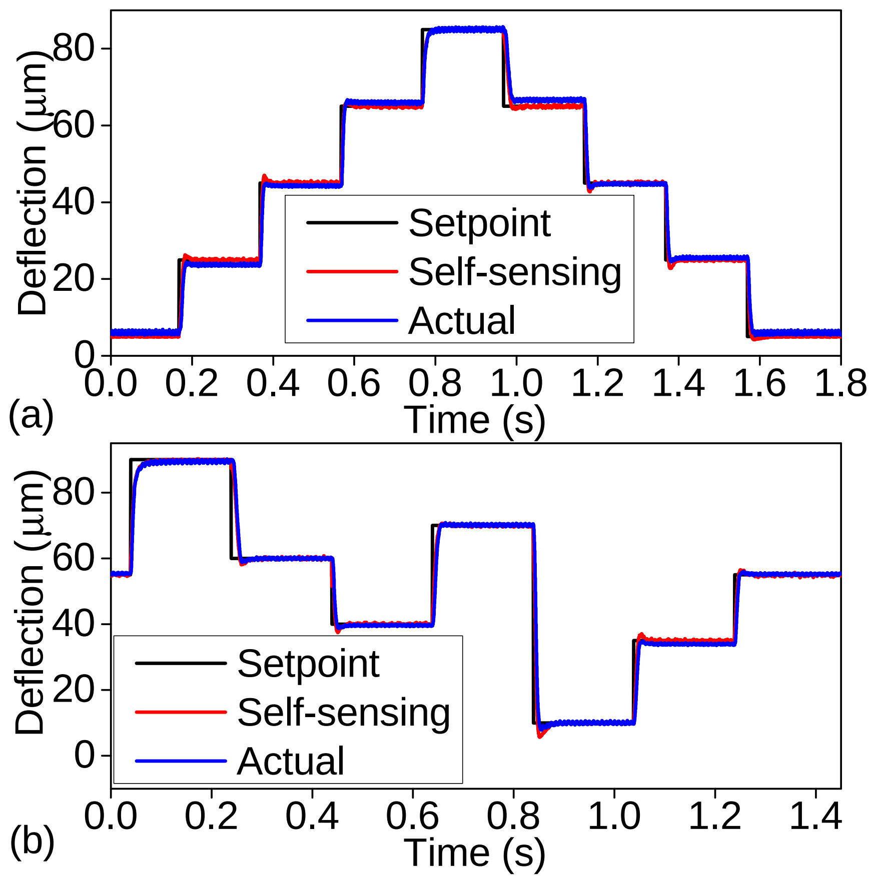

Figure 6.7: Step reference input results for the (a) increasing-decreasing loop and (b) arbitrary steps experiments.

The effectiveness and accuracy of the self-sensing feedback micro-actuator is evident. An average D_r steady-state error of 1.15 µm is found from all the different steps in both sequences with average system accuracy of ±430 nm. The maximum steady-state error is

1.88 µm from all the setpoint values tested. Rise times — defined here as time taken by D_r to change from 10 to 90 % of the step value — ranging from 5 to 12 ms are obtained with maximum percent overshoot of 8.4 %. These results are in good agreement with the closed-loop performance specifications and show that self-sensing can be used to accurately and effectively control the deflection of VO_2-based MEMS actuators.

6.6 Summary

In this chapter, a closed-loop controlled VO_2-based MEMS actuator with monolithically integrated heater and deflection sensing has been designed and implemented. The VO_2 resistance was used as the sensing element due to the strong correlation between resistance and deflection, and because of the hysteresis reduction effect recently discovered when measuring multiple VO_2 properties. A simple, yet effective, Boltzmann function was used to model the resistance-to-deflection relationship to obtain an estimated deflection value. The resistance and deflection dynamic responses were used to design a PI compensator that accurately controlled the actual deflection using the estimated deflection value as the feedback signal. Sinusoidal and step input tracking experiments were performed in order to show the performance of the micro-actuator in terms of frequency response, transient response and steady-state error.

CHAPTER 7
SELF-HEATING CONTROL

VO_2-based MEMS actuators can be further miniaturized and studied by inducing the actuation through the heating of the VO_2 film itself, instead of having additional heating components. This technique is usually referred to as self-heating. In this chapter, the actuation of the same VO_2-based MEMS actuators shown in **Figure** 4.8 is achieved by voltage and current controlled techniques. Since the actuation in these devices is produced by Joule heating — an effect inherently unstable in MIT materials if controlled by voltage — current-controlled actuation of MIT materials is desired [119–121]. Nonetheless, the voltage controlled actuation is also studied in this thesis for comparison purposes.

7.1 Measurement Setup

The setup used for the experiments done in this chapter is shown in **Figure** 7.1 and its operation is similar to the one in **Figure** 6.1 except that there are no connections made to the Pt heater and that it includes a signal conditioning circuit. In this setup V_j represents the $j - th$ output of the circuit and V_{in} is the input voltage to the circuit, which can be controlled using a PI or varied manually. This supplies the required voltage or current to the VO_2 resistance (R_v). In the voltage-controlled experiments, the circuit shown in **Figure** 7.2 was used, which consisted of a load dependent voltage-controlled actuation. The resistance in series with the R_v ($100\,\mathrm{k\Omega}$ total) is used to limit the current through the VO_2, while the voltage divider is used to limit the voltage going to the DAQ/FPGA (V_1). The voltage amplifier is used to amplify the voltage supplied by the FPGA (V_{in}) and produce Joule heating of the VO_2 resistor. The voltage-controlled by the circuit is dependent on the VO_2 resistance, which decreases abruptly during the transition as the voltage is increased. This results in actuation instability. In Joule heating process (resistive heating), the temperature

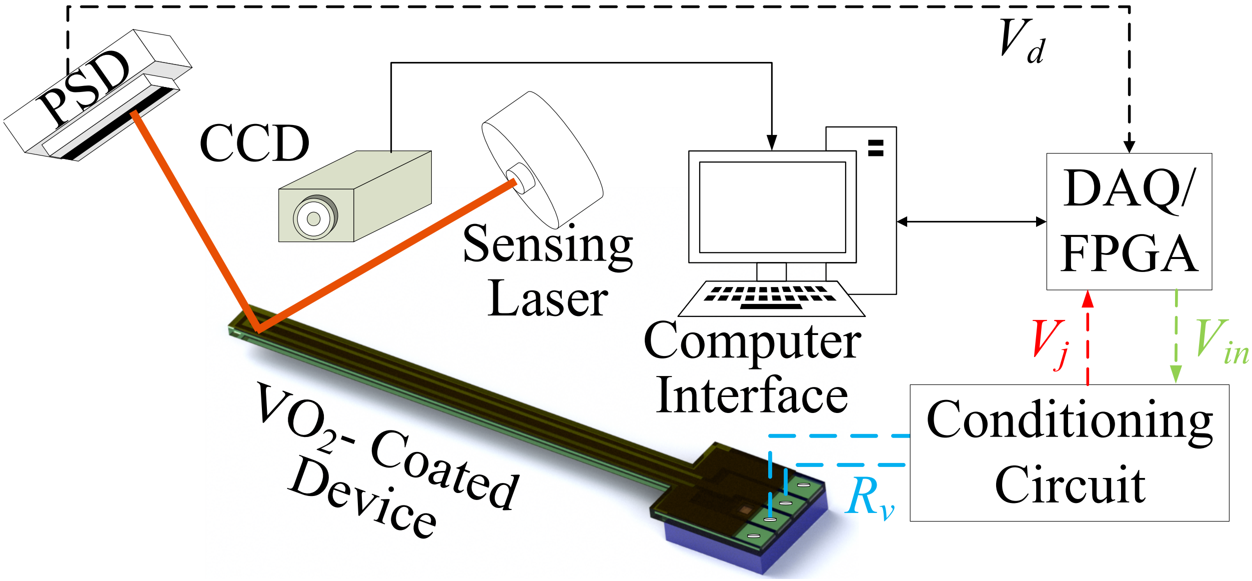

Figure 7.1: Measurement setup used for performing the self-heating quasi-static and dynamic characterization using voltage or current-controlled actuation of the VO_2.

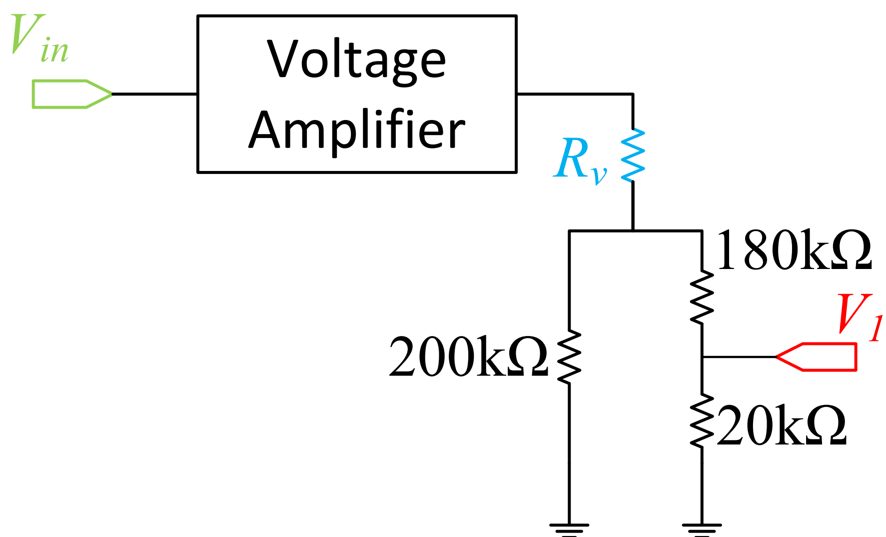

Figure 7.2: Schematic of the compensating circuit used in the voltage-controlled experiments. The inputs and outputs colors correspond to those in the setup schematic in **Figure** 7.1.

is directly related to the power dissipated (P) by the resistor, which in turn is very sensitive to the current I ($P = I^2R$). As the the voltage is increased and the temperature is increased due to Joule heating, the VO_2 resistance drops abruptly, which causes a sudden increase in current ($I = V/R$). This abrupt change in current translates into a sudden increase in power, which then produces an increase in temperature and a drastic drop in resistance.

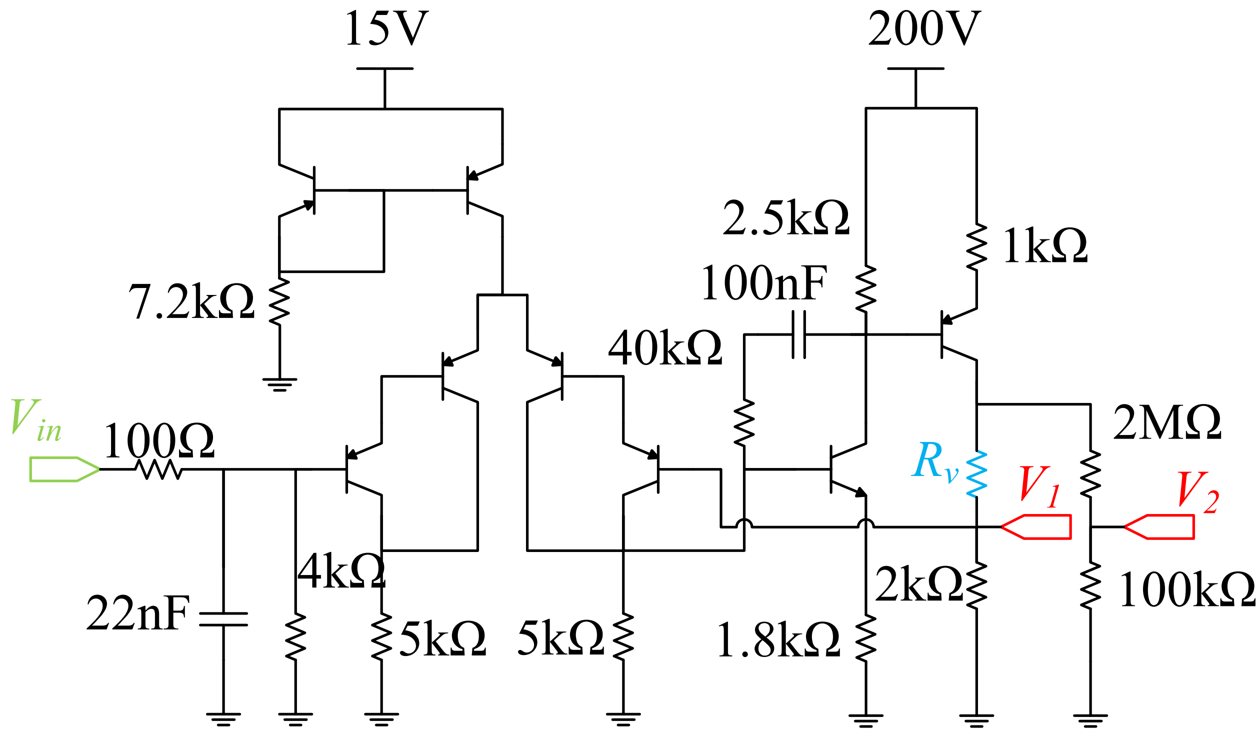

Figure 7.3: Schematic of the compensating circuit used in the current-controlled experiments.

This unstable cycle is repeated until equilibrium is reached. This has been observed in other studies where VO_2 is used as an electronic switch [119]. Other materials, such as titanium dioxide (TiO_2) have been successfully operated using current-controlled sources [120]. If the current is controlled (instead of the voltage) there is no actuation instability, which allows continuous operation throughout the transition. To this end, the closed-loop voltage-to-current converter shown in **Figure** 7.3 is used for the current-controlled actuation of the VO_2-based MEMS actuator in closed-loop.

7.2 Self-heating Open-loop Characterization

Using the setup described in **Figure** 7.1, the voltage and current-controlled experiments are performed. The voltage-controlled experiments confirmed that self-sensing using self-heating of the VO_2 is not possible (at least for the current device design) and that current control is needed in order to achieve stable VO_2 actuation.

7.2.1 Voltage-controlled Actuation

Figure 7.4-(a-b) shows the quasi-static actuation of the VO_2-based MEMS actuator in terms of its deflection and resistance change. The curves are obtained by measuring deflection and resistance through a series of increasing-decreasing voltage cycles in steps of 2 V. It is observed that approximately 35 V is the lowest voltage where a deflection value can be measured. Any voltage below this would result in instability due to the VO_2 resistance change across the IMT. It is also observed that for the voltage range of $35 - 95$ V the resistance change is almost linear — the VO_2 resistance measured is almost completely in its metallic state — while a significant amount of the deflection change is still observed. This is a result of the pronounced difference in transition voltage between the mechanical and electrical domains in this experiment, which hinders the use of self-sensing for hysteresis reduction for this device design (see **Figure** 7.5). Although the reason for the difference in transitions is currently unknown, it is thought to be related to formation of a filament or conduction channel resulting from the IMT of the VO_2. The filamentary behavior of VO_2

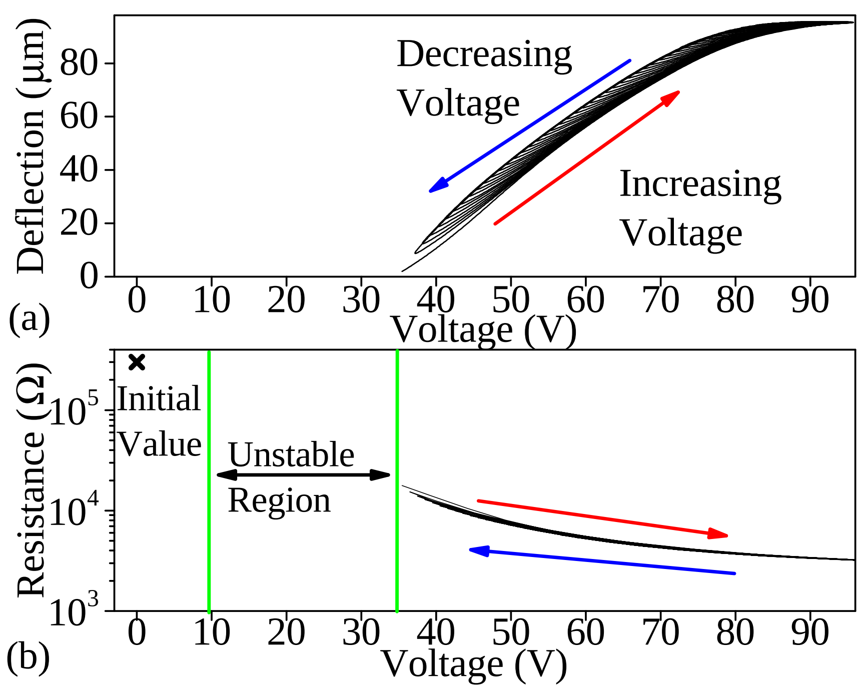

Figure 7.4: Quasi-static deflection (a) and resistance (b) as a function of supplied voltage for the voltage-controlled experiments.

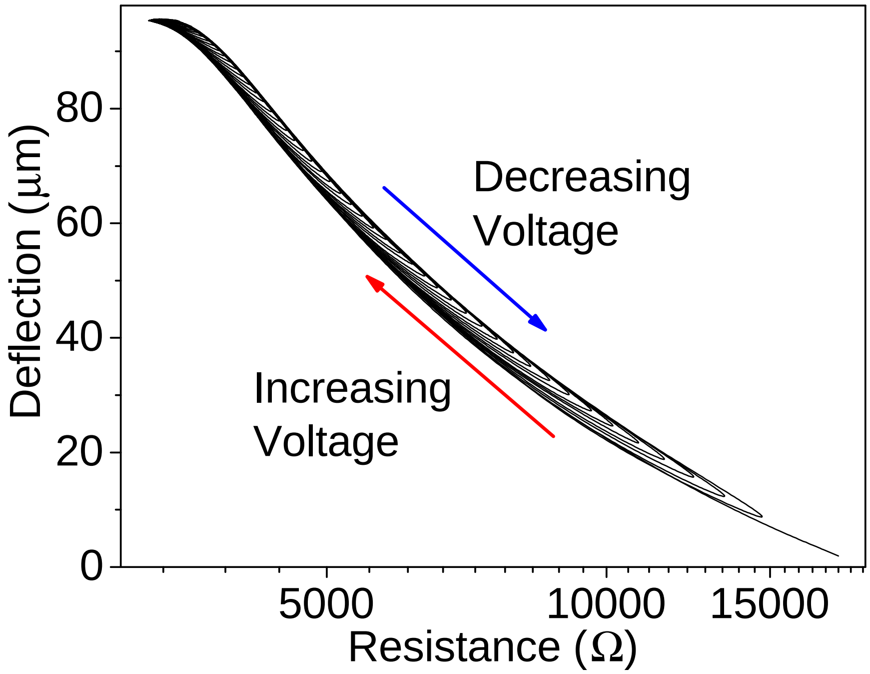

Figure 7.5: Deflection of the VO_2 actuator as a function of VO_2 resistance using self-heating of the VO_2. Note that the hysteresis is not reduced due to the differences in mechanical and electrical transition voltages.

has been observed in other self-heating experiments [122].

7.2.2 Current-controlled Actuation

To eliminate the instability produced by the self-heating of the VO_2 through the IMT, the voltage-to-current converter in **Figure** 7.3 is used as the conditioning circuit hereinafter. A series of experiments are performed using the current-controlled actuation in order to characterize the self-heating actuation in terms of quasi-static and dynamic response, develop a dynamic model for control design purposes, and implement closed-loop deflection control using self-heating.

For this experiment, the current through the VO_2 is varied from 200 μA to 1.4 mA and back to 200 μA in steps of 25 μA while the deflection is measured. To ensure steady-state deflection values were reached, the deflection measurement is performed after 1 s from reaching the steady-state current setpoint value. **Figure** 7.6 shows the deflection as a function of

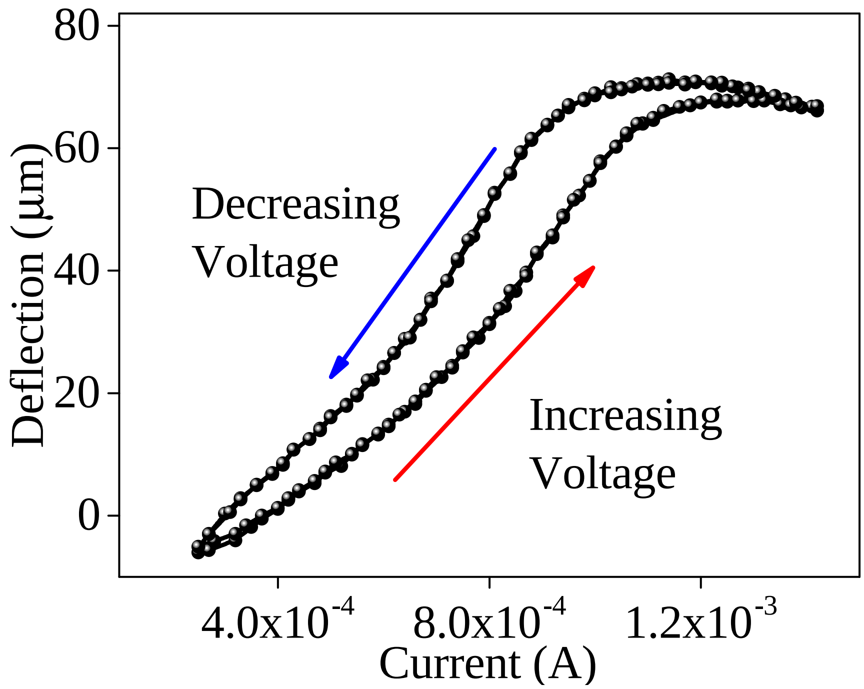

Figure 7.6: Deflection of the VO_2-based MEMS actuator as a function of current through the VO_2.

current through the VO_2 for this experiment.

The observed hysteretic curve resembles the ones from previous experiments except for the behavior at low currents, where it seems the observed hysteresis is an inner loop of the major hysteresis curve. However, it was experimentally observed through side view images that there were no difference between the deflection at 200 µA and zero — obtained by turning off the conditioning circuit. A maximum deflection change of more than 70 µm is observed, which is produced by a current of 1.4 mA and a VO_2 resistance of 5.5 kΩ resulting on a power consumption of 8.8 mW. This power value is a twice the one obtained in the experiments from **Chapter 5**, when the actuation was done by heating the Pt (instead of the VO_2).

The frequency response of the micro-actuator is measured in order to study its dynamical performance and limits. In this experiment, the current-to-deflection gain of the micro-actuator is obtained for a time-varying sinusoidal input current within a frequency range of 0.1 Hz to 1 kHz.The offset and amplitude of the sinusoidal signal are 0.8 mA and 0.1 mA,

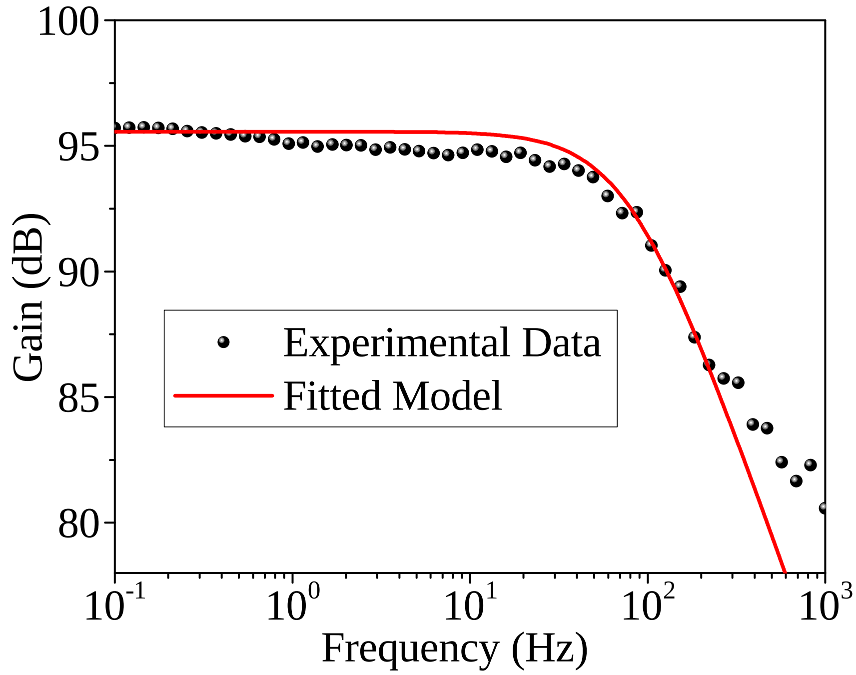

Figure 7.7: Open-loop frequency response of the VO_2-based MEMS actuator using self-heating.

respectively. **Figure** 7.7 shows the micro-actuator gain in decibels, which shows a 3 dB cut-off frequency of approximately 65 Hz. Similarly to the results obtained in the experiments in **Chapter 5**, the observed behavior is only limited by the thermal dissipation through the cantilever for the frequency range studied.

7.3 Modeling and Controller Design

The experimental data obtained in the device characterization can be used to find an approximate dynamic self-heating model for the micro-actuator. This model can then be used to develop a PID controller for accurate deflection control. **Figure** 7.7 also shows a plot of the first-order transfer function model fitted with the experimental data. Similarly to the experiments in **Chapter 6**, the model used is given by **Equation** (6.2) with the exception that A_0 and τ are now approximately $60\,000\,\mu\mathrm{m\,A^{-1}}$ and $0.002\,\mathrm{s\,rad^{-1}}$, respectively. These parameters are found using a least squared method to solve the magnitude of **Equation** (6.2) given by $20 \log (|G(j\omega)|)$ and fitted with the experimental data. Note that other mechanical dynamics such as internal and external damping are ignored since they occur at much higher frequencies.

The block diagram for the closed-loop system using self-heating is shown in **Figure** 7.8, which is a slight variation from the one in **Figure** 5.8. Here, $CC(s)$ represents the transfer function of the current compensating circuit, which can be modeled by a first order transfer function with time constant equal to $1.6 \times 10^{-6}\,\mathrm{s\,rad^{-1}}$ and DC gain of $5.6 \times 10^{-4}\,\mathrm{A\,V^{-1}}$. The PI controller ($K(s)$), which is given by **Equation** (6.3), is designed in order for the system to have a bandwidth of 200 Hz with a maximum percent overshoot of 15 %. Using these device specifications the gains of the PI controller are calculated to be $K_p = 0.9$ and $K_i = 750$. The simulated closed-loop frequency response of the VO_2-based MEMS actuator using self-heating is shown in **Figure** 7.8.

7.4 Results

A series of tracking experiments are completed in order to show the performance of the closed-loop system of **Figure** 5.8. First, a closed-loop frequency response experiment is done to compare simulation and experimental results and determine the bandwidth of the system. Second, a sinusoidal tracking response is performed to show time varying system performance. Finally, an input reference tracking experiment is done in order to study deflection transients and steady-state tracking errors. These three experiments are discussed in the following sub-sections.

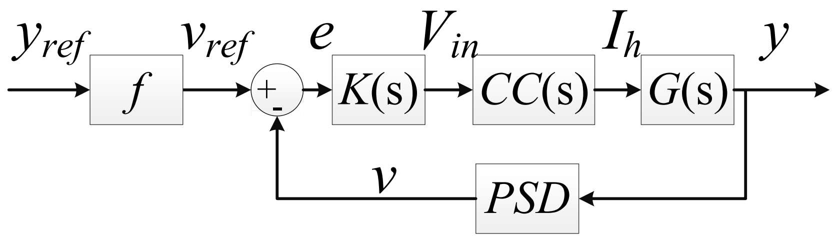

Figure 7.8: Block diagram of the closed-loop VO_2-based MEMS micro-actuator.

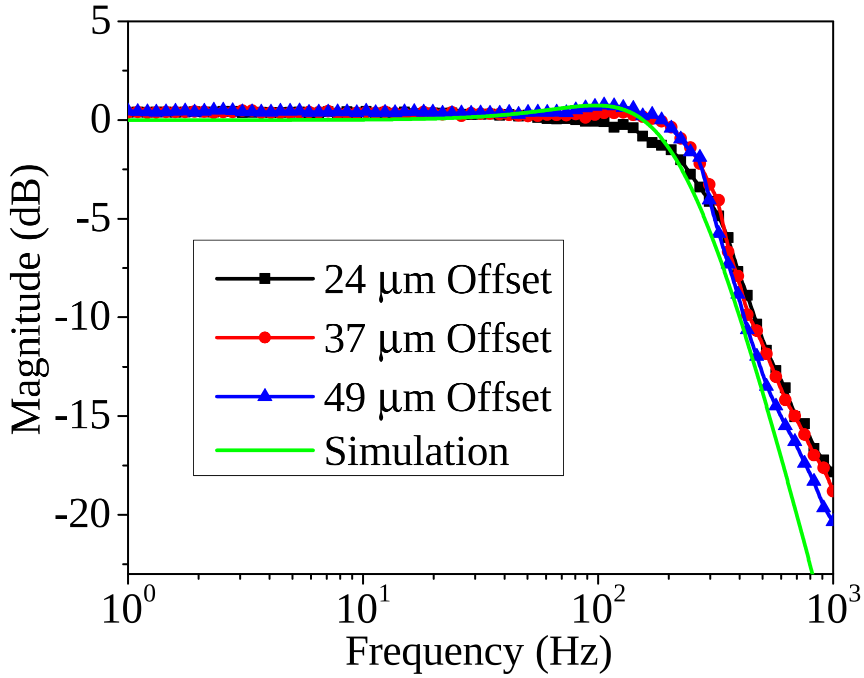

Figure 7.9: Simulated and experimental closed-loop frequency response of the VO_2-based MEMS actuator using self-heating. The three offset labels correspond to sinusoidal signals with different reference offsets, but with same amplitude.

7.4.1 Closed-loop Frequency Response

Three different sinusoidal signals with different reference offsets (24, 37, and 49 µm), but same amplitude are used as the input reference signal in three separate experiments. The frequency of each signal is varied from 1 Hz to 1 kHz while the output-input gain is measured. **Figure** 7.9 shows the experimental results obtained with the three different offsets in addition to the simulated response.

It is observed that the response of all the experimental curves are similar with slight differences product of the hysteresis nonlinearity. The bandwidth of all three signals is relatively close to the simulated curve with a value of approximately 300 Hz. This shows that the deflection of the self-heated micro-actuator can be accurately tracked with a gain of 0 dB up to frequencies close to 100 Hz across the complete actuation range. While this experiment reveals frequency-dependent magnitude and bandwidth performance, time-dependent sinusoidal tracking experiment at different frequencies reveals transient and lag performance under continuously changing setpoint [30, 32].

7.4.2 Sinusoidal Tracking Response

In this experiment a sinusoidal input with offset and magnitude of 37 µm and 14 µm is used while the deflection of the micro-actuator is measured as a function of time. These values were chosen to cover a wide range of the hysteresis. However, different values may produce slightly different response performance due to the hysteresis non-linearity. **Figure** 7.10 shows the sinusoidal time responses as a function for four different actuation frequencies of 5, 10, 50, and 100 Hz. At the two lowest frequency values, effective tracking performance is observed with relatively small lag. For the two higher frequencies, a more noticeable lag effect is observed although it is not constant for all setpoint values, which is attributed to strong hysteretic asymmetry observed. This behavior is similar to the one observed in the Joule heating control experiments discussed in **Chapter 5**, which hinders the experimental phase lag calculations.

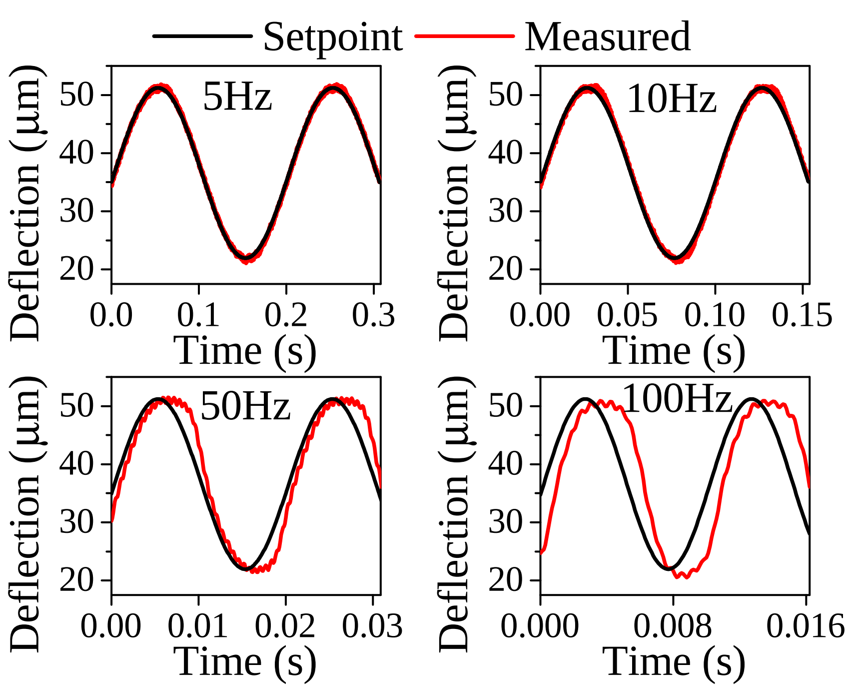

Figure 7.10: Sinusoidal tracking response of the VO_2-based MEMS actuator using self-heating under four different frequencies.

7.4.3 Step Reference Response

To obtain the tracking performance under step input response across the VO_2 transition, two separate input sequences are employed. The first one is aimed at studying the performance of input steps through a hysteresis loop, while the second one is intended to study the performance inside the hysteresis with randomly selected setpoints. The duration of each setpoint in both experiments is 0.2 s, which is more than required for the micro-actuator to reach steady-state values [30]. This allows to monitor the transient signals of each setpoint which is used to determine rise/fall times, overshoot, and steady-state error.

Figure 7.11-(a-b) shows the step input response of the VO_2 micro-actuator to both input sequences using self-heating. The effectiveness of deflection control is evident resulting in a performance that accurately follows the desired behavior. While the average steady-state error for all setpoints in both sequences is zero micrometers, the average accuracy of the system is ±0.7 µm with maximum of ±0.8 µm. The maximum observed percent overshoot

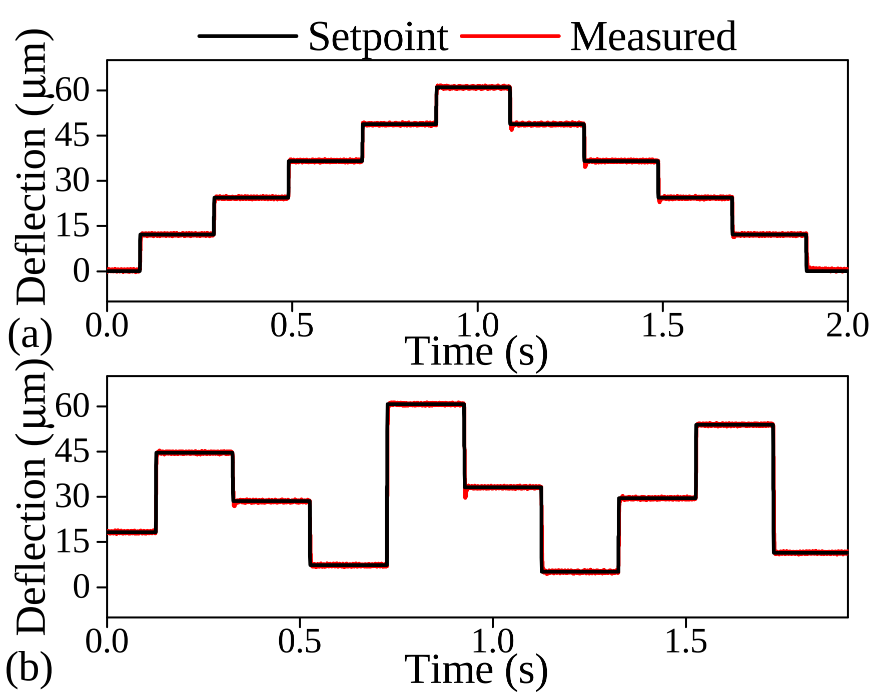

Figure 7.11: Step input tracking response of the VO_2-based MEMS actuator using self-heating under for two different sequences: an increasing-decreasing hysteresis loop (a) and randomly selected inputs inside the hysteresis (b).

is 12.5 %, which is mainly observed when the setpoint is decreased. Maximum rise time of 2 ms is obtained with minimum of 0.5 ms. The rise/fall times are defined as the time it takes the deflection to go from 10 % to 90 % of the setpoint value.

7.5 Summary

Voltage-controlled and current-controlled self-heating of the VO_2 were used to drive the MEMS micro-actuators. It was found that the present device design is not able to produce strongly correlated resistance and deflection measurements, and hence, self-sensing is not possible. Current-controlled actuation was found to be the most stable of the two self-heating methods and was used to characterize the device in terms of quasi-static and dynamic analysis. A dynamic model was derived from the experimental data and used to design a PI controller that accurately controlled the self-heated VO_2-based MEMS actuator. A series of tracking experiments were performed to determine the effectiveness, accuracy and performance of the micro-actuator in terms of steady-state error, overshoot, and response times.

CHAPTER 8
SUMMARY

8.1 Summary of Contributions

In this work, the development of an accurately controlled VO_2-based MEMS actuator with integrated heaters and self-sensing technique is presented. A preliminary set of studies that involved the characterization of VO_2-based devices in terms of total tip displacement across the transition, dynamic displacements using photo-thermal actuation, strain energy density calculations, and the proof-of-concept of self-sensing in VO_2 are performed. The results obtained from these studies suggest that VO_2 micro-actuators possess advantages over other thermal actuation technologies, such as multi-layered structures and SMAs, in terms of strain energy density and repeatability. Based on this performance, a VO_2-based MEMS actuator is proposed that allowed for electro-thermal actuation and self-sensing of the device deflection through VO_2 resistance measurements. A detailed design and fabrication process, which involves the use of FEM simulations, masks design, and clean-room fabrication, is presented. After fabrication, a comprehensive device characterization is performed, which provides information for modeling and controller design and implementation. A series of experiments for determining steady-state, tracking, and frequency response closed-loop performance are realized using external sensing and self-sensing. A self-heating actuation technique is also studied, in which the voltage and current through the VO_2 are controlled in order to precisely control the device deflection.

8.2 List of Problems Solved in this Thesis

This work addresses the following:

1. Characterize VO_2 actuators in terms of total deflection strain energy density, overall

quasi-static displacement, photo-thermal actuation and self-sensing.

2. Design and fabricate a VO_2-based MEMS actuator with integrated VO_2 resistance measurement in the device, which enables simultaneous *in situ* resistance and deflection measurements.

3. Characterize thoroughly the VO_2 MEMS actuator in terms of quasi-static response, frequency and time domains, reliability, and rate dependency.

4. Perform analytical and numerical micro-actuator thermal and mechanical modeling for use in controller design and results validation.

5. Study the closed-loop actuator performance through a series of reference tracking experiments, which includes closed-loop frequency response, and step and sinusoidal reference tracking.

6. Demonstrate VO_2 cross-property hysteresis reduction across the complete actuation range using the resistance-deflection relationship.

7. Demonstrate self-sensing feedback and self-heating control in the VO_2-based MEMS actuator.

BIBLIOGRAPHY

BIBLIOGRAPHY

[1] B. Kim, M. G. Lee, Y. P. Lee, Y. Kim, and G. Lee, “An earthworm-like micro robot using shape memory alloy actuator,” *Sensors and Actuators A: Physical*, vol. 125, no. 2, pp. 429–437, 2006.

[2] O. C. Jeong and S. S. Yang, “Fabrication of a thermopneumatic microactuator with a corrugated p plus silicon diaphragm,” *Sensors and Actuators A: Physical*, vol. 80, no. 1, pp. 62–67, 2000.

[3] M. C. LeMieux, M. E. McConney, Y.-H. Lin, S. Singamaneni, H. Jiang, T. J. Bunning, and V. V. Tsukruk, “Polymeric nanolayers as actuators for ultrasensitive thermal bimorphs,” *Nano Letters*, vol. 6, no. 4, pp. 730–734, 2006.

[4] E. Enikov, S. Kedar, and K. Lazarov, “Analytical model for analysis and design of V-shaped thermal microactuators,” *Microelectromechanical Systems, Journal of*, vol. 14, no. 4, pp. 788–798, 2005.

[5] J. Grade, H. Jerman, and T. Kenny, “Design of large deflection electrostatic actuators,” *Microelectromechanical Systems, Journal of*, vol. 12, no. 3, pp. 335–343, 2003.

[6] P. H. Pham, D. V. Dao, L. B. Dang, and S. Sugiyama, “Single mask, simple structure micro rotational motor driven by electrostatic comb-drive actuators,” *Journal of Micromechanics and Microengineering*, vol. 22, no. 1, pp. 015 008–1–015 008–7, 2012.

[7] M. Mita, M. Arai, S. Tensaka, D. Kobayashi, and H. Fujita, “A micromachined impact microactuator driven by electrostatic force,” *Microelectromechanical Systems, Journal of*, vol. 12, no. 1, pp. 37–41, 2003.

[8] J. Juuti, K. KordÃąs, R. Lonnakko, V.-P. Moilanen, and S. LeppÃďvuori, “Mechanically amplified large displacement piezoelectric actuators,” *Sensors and Actuators A: Physical*, vol. 120, no. 1, pp. 225–231, 2005.

[9] B. Gaihre, G. Alici, G. M. Spinks, and J. Cairney, “Pushing the limits for microactuators based on electroactive polymers,” *Microelectromechanical Systems, Journal of*, vol. 21, no. 3, pp. 574–585, 2012.

[10] Y. Q. Fu, J. K. Luo, S. E. Ong, S. Zhang, A. J. Flewitt, and W. I. Milne, “A shape memory microcage of TiNi/DLC films for biological applications,” *Journal of Micromechanics and Microengineering*, vol. 18, no. 3, pp. 035 026–1–035 026–8, 2008.

[11] R. Messenger, Q. Aten, T. McLain, and L. Howell, “Piezoresistive feedback control of a MEMS thermal actuator,” *Microelectromechanical Systems, Journal of*, vol. 18, no. 6, pp. 1267–1278, 2009.

[12] L. Lin, A. Pisano, and R. Howe, “A micro strain gauge with mechanical amplifier,” *Microelectromechanical Systems, Journal of*, vol. 6, no. 4, pp. 313–321, 1997.

[13] M. Suster, J. Guo, N. Chaimanonart, W. Ko, and D. Young, "A high-performance MEMS capacitive strain sensing system," *Microelectromechanical Systems, Journal of*, vol. 15, no. 5, pp. 1069–1077, 2006.

[14] A. Rúa, F. E. Fernández, and N. Sepúlveda, "Bending in VO_2-coated microcantilevers suitable for thermally activated actuators," *Journal of Applied Physics*, vol. 107, no. 7, pp. 074 506–1–074 506–4, 2010.

[15] N. Sepúlveda, J. Lu, D. Aslam, and J. P. Sullivan, "High-performance polycrystalline diamond micro- and nanoresonators," *Microelectromechanical Systems, Journal of*, vol. 17, no. 2, pp. 473–482, 2008.

[16] F. Amiot and J. P. Roger, "Nomarski imaging interferometry to measure the displacement field of micro-electro-mechanical systems," *Applied Optics*, vol. 45, no. 30, pp. 7800–7810, 2006.

[17] C.-C. Lan and C.-H. Fan, "An accurate self-sensing method for the control of shape memory alloy actuated flexures," *Sensors and Actuators A: Physical*, vol. 163, no. 1, pp. 323–332, 2010.

[18] M. Rakotondrabe, "Bouc-wen modeling and inverse multiplicative structure to compensate hysteresis nonlinearity in piezoelectric actuators," *Automation Science and Engineering, IEEE Transactions on*, vol. 8, no. 2, pp. 428–431, 2011.

[19] P. Krulevitch, A. Lee, P. Ramsey, J. Trevino, J. Hamilton, and M. Northrup, "Thin film shape memory alloy microactuators," *Microelectromechanical Systems, Journal of*, vol. 5, no. 4, pp. 270–282, 1996.

[20] F. Morin, "Oxides which show a metal-to-insulator transition at the neel temperature," *Physical Review Letters*, vol. 3, no. 1, pp. 34–36, 1959.

[21] J. Barker, A. S., H. W. Verleur, and H. J. Guggenheim, "Infrared optical properties of vanadium dioxide above and below the transition temperature," *Physical Review Letters*, vol. 17, no. 26, pp. 1286–1289, 1966.

[22] A. Cavalleri, T. Dekorsy, H. H. W. Chong, J. C. Kieffer, and R. W. Schoenlein, "Evidence for a structurally-driven insulator-to-metal transition in VO_2: A view from the ultrafast timescale," *Physical Review B*, vol. 70, pp. 161 102–1–161 102–4, 2004.

[23] J. Cao, W. Fan, Q. Zhou, E. Sheu, A. Liu, C. Barrett, and J. Wu, "Colossal thermal-mechanical actuation via phase transition in single-crystal VO_2 microcantilevers," *Journal of Applied Physics*, vol. 108, no. 8, pp. 083 538–1–083 538–4, 2010.

[24] K. Wang, C. Cheng, E. Cardona, J. Guan, K. Liu, and J. Wu, "Performance limits of microactuation with vanadium dioxide as a solid engine," *ACS Nano*, vol. 7, no. 3, pp. 2266–2272, 2013.

[25] R. Cabrera, E. Merced, and N. Sepúlveda, "Performance of electro-thermally driven VO_2-based MEMS actuators," *Microelectromechanical Systems, Journal of*, 2013, 10.1109/JMEMS.2013.2271774.

[26] J. Zhang, E. Merced, N. Sepúlveda, and X. Tan, "Modeling and inverse compensation of nonmonotonic hysteresis in VO_2-coated microactuators," *Mechatronics, IEEE/ASME Transactions on*, 2013, 10.1109/TMECH.2013.2250989.

[27] J. Nag, R. F. Haglund, E. Andrew Payzant, and K. L. More, "Non-congruence of thermally driven structural and electronic transitions in VO_2," *Journal of Applied Physics*, vol. 112, no. 10, pp. 103 532–1–103 532–7, 2012.

[28] E. Merced, N. Dávila, D. Torres, R. Cabrera, F. E. Fernández, and N. Sepúlveda, "Photothermal actuation of VO_2:Cr-coated microcantilevers in air and aqueous media," *Smart Materials and Structures*, vol. 21, no. 10, pp. 105 009–1–105 009–9, 2012.

[29] E. Merced, J. Zhang, X. Tan, and N. Sepúlveda, "Robust control of VO_2-coated microbenders using self-sensing feedback," *Mechatronics, IEEE/ASME Transactions on*, 2013, 10.1109/TMECH.2013.2289375.

[30] E. Merced, X. Tan, and N. Sepúlveda, "Closed-loop tracking of large displacements in electro-thermally actuated VO_2-based mems," *Microelectromechanical Systems, Journal of*, 2014, 10.1109/JMEMS.2014.2304694.

[31] E. Merced, X. Tan, and N. SepÃžlveda, "Strain energy density of VO_2-based microactuators," *Sensors and Actuators A: Physical*, vol. 196, pp. 30–37, 2013.

[32] E. Merced, X. Tan, and N. Sepúlveda, "An electro-thermally actuated VO_2-based MEMS using self-sensing feedback control," *Microelectromechanical Systems, Journal of*, 2014, To Appear.

[33] J. Wright, Y.-C. Tai, and S.-C. Chang, "A large-force, fully-integrated MEMS magnetic actuator," in *Solid State Sensors and Actuators, International Conference on*, vol. 2, 1997, pp. 793–796.

[34] C. H. Ko, J. J. Yang, and J. C. Chiou, "Efficient magnetic microactuator with an enclosed magnetic core," *Journal of Microlithography, Microfabrication and Microsystems*, vol. 1, pp. 144–149, 2002.

[35] R. Legtenberg, A. W. Groeneveld, and M. Elwenspoek, "Comb-drive actuators for large displacements," *Journal of Micromechanics and Microengineering*, vol. 6, no. 3, pp. 320–329, 1996.

[36] E. J. García and J. J. Sniegowski, "Surface micromachined microengine," *Sensors and Actuators A: Physical*, vol. 48, no. 3, pp. 203–214, 1995.

[37] D. J. Bell, T. J. Lu, N. A. Fleck, and S. M. Spearing, "MEMS actuators and sensors: observations on their performance and selection for purpose," *Journal of Micromechanics and Microengineering*, vol. 15, no. 7, pp. S153–S164, 2005.

[38] T. Akiyama, D. Collard, and H. Fujita, "Scratch drive actuator with mechanical links for self-assembly of three-dimensional MEMS," *Microelectromechanical Systems, Journal of*, vol. 6, no. 1, pp. 10–17, 1997.

[39] J. Suh, C. Storment, and G. T. A. Kovacs, “Characterization of multi-segment organic thermal actuators,” in *Solid-State Sensors and Actuators, International Conference on*, vol. 2, 1995, pp. 333–336.

[40] A. Atre, “Analysis of out-of-plane thermal microactuators,” *Journal of Micromechanics and Microengineering*, vol. 16, no. 2, pp. 205–213, 2006.

[41] G. Alici, V. Devaud, P. Renaud, and G. Spinks, “Conducting polymer microactuators operating in air,” *Journal of Micromechanics and Microengineering*, vol. 19, no. 2, pp. 025 017–1–025 017–9, 2009.

[42] Z. Chen and X. Tan, “Monolithic fabrication of ionic polymerâĂŞmetal composite actuators capable of complex deformation,” *Sensors and Actuators A: Physical*, vol. 157, no. 2, pp. 246–257, 2010.

[43] N. Conway and S.-G. Kim, “Large-strain, piezoelectric, in-plane micro-actuator,” in *Micro Electro Mechanical Systems, International Conference on. (MEMS)*, 2004, pp. 454–457.

[44] N. J. Graf and M. T. Browser, “A soft-polymer piezoelectric bimorph cantilever-actuated peristaltic micropump,” *Lab Chip*, vol. 8, no. 10, p. 1664âĂŞ1670, 2008.

[45] J. Kalb, Q. Guo, X. Zhang, Y. Li, C. Sow, and C. V. Thompson, “Phase-change materials in optically triggered microactuators,” *Microelectromechanical Systems, Journal of*, vol. 17, no. 5, pp. 1094–1103, Oct 2008.

[46] J. Ouyang and Y. Zhu, “Z-shaped MEMS thermal actuators: Piezoresistive self-sensing and preliminary results for feedback control,” *Microelectromechanical Systems, Journal of*, vol. 21, no. 3, pp. 596–604, 2012.

[47] A. Kawamata, Y. Kadota, H. Hosaka, and T. Morita, “Self-sensing piezoelectric actuator using permittivity detection,” *Ferroelectrics*, vol. 368, no. 1, pp. 194–201, 2008.

[48] B. Koo, X. Zhang, J. Dong, S. Salapaka, and P. Ferreira, “A 2 degree-of-freedom SOI-MEMS translation stage with closed-loop positioning,” *Microelectromechanical Systems, Journal of*, vol. 21, no. 1, pp. 13–22, 2012.

[49] B. Cagdaser and B. Boser, “Low-voltage electrostatic actuation with inherent position feedback,” *Microelectromechanical Systems, Journal of*, vol. 21, no. 5, pp. 1187–1196, 2012.

[50] S. Towfighian, A. Seleim, E. M. Abdel-Rahman, and G. R. Heppler, “A large-stroke electrostatic micro-actuator,” *Journal of Micromechanics and Microengineering*, vol. 21, no. 7, pp. 075 023–1–075 023–12, 2011.

[51] Y. Zhu, A. Bazaei, S. O. R. Moheimani, and M. Yuce, “Design, modeling, and control of a micromachined nanopositioner with integrated electrothermal actuation and sensing,” *Microelectromechanical Systems, Journal of*, vol. 20, no. 3, pp. 711–719, 2011.

[52] B. Borovic, F. Lewis, D. Agonafer, E. S. Kolesar, M. Hossain, and D. Popa, "Method for determining a dynamical state-space model for control of thermal MEMS devices," *Microelectromechanical Systems, Journal of*, vol. 14, no. 5, pp. 961–970, 2005.

[53] G. Song, V. Chaudhry, and C. Batur, "Precision tracking control of shape memory alloy actuators using neural networks and a sliding-mode based robust controller," *Smart Materials and Structures*, vol. 12, no. 2, pp. 223–231, 2003.

[54] A. Mannani and H. Talebi, "A fuzzy lyapunov-based control strategy for a macro-micro manipulator: Experimental results," *Control Systems Technology, IEEE Transactions on*, vol. 15, no. 2, pp. 375–383, 2007.

[55] Z. Chen and X. Tan, "A control-oriented and physics-based model for ionic polymer–metal composite actuators," *Mechatronics, IEEE/ASME Transactions on*, vol. 13, no. 5, pp. 519–529, 2008.

[56] L. Riccardi, D. Naso, H. Janocha, and B. Turchiano, "A precise positioning actuator based on feedback-controlled magnetic shape memory alloys," *Mechatronics*, vol. 22, no. 5, pp. 568–576, 2012.

[57] Y. Shan and K. K. Leang, "Dual-stage repetitive control with Prandtl-Ishlinskii hysteresis inversion for piezo-based nanopositioning," *Mechatronics*, vol. 22, no. 3, pp. 271–281, 2012.

[58] J. L. Arlett, J. R. Maloney, B. Gudlewski, M. Muluneh, and M. L. Roukes, "Self-sensing micro- and nanocantilevers with attonewton-scale force resolution," *Nano Letters*, vol. 6, no. 5, pp. 1000–1006, 2006.

[59] C. K. Pang, G. Guo, B. Chen, and T.-H. Lee, "Self-sensing actuation for nanopositioning and active-mode damping in dual-stage hdds," *Mechatronics, IEEE/ASME Transactions on*, vol. 11, no. 3, pp. 328–338, 2006.

[60] C.-C. Lan, C.-M. Lin, and C.-H. Fan, "A self-sensing microgripper module with wide handling ranges," *Mechatronics, IEEE/ASME Transactions on*, vol. 16, no. 1, pp. 141–150, 2011.

[61] B.-D. Chan, F. Mateen, C.-L. Chang, K. Icoz, and C. Savran, "A compact manually actuated micromanipulator," *Microelectromechanical Systems, Journal of*, vol. 21, no. 1, pp. 7–9, 2012.

[62] F. Beyeler, A. Neild, S. Oberti, D. Bell, Y. Sun, J. Dual, and B. Nelson, "Monolithically fabricated microgripper with integrated force sensor for manipulating microobjects and biological cells aligned in an ultrasonic field," *Microelectromechanical Systems, Journal of*, vol. 16, no. 1, pp. 7–15, 2007.

[63] N. Weber, D. Hertkorn, H. Zappe, and A. Seifert, "Polymer/silicon hard magnetic micromirrors," *Microelectromechanical Systems, Journal of*, vol. 21, no. 5, pp. 1098–1106, 2012.

[64] G.-B. Lee, C.-H. Lin, and S.-C. Chang, "Micromachine-based multi-channel flow cytometers for cell/particle counting and sorting," *Journal of Micromechanics and Microengineering*, vol. 15, no. 3, pp. 447–454, 2005.

[65] S.-H. Liu, T.-S. Huang, and J.-Y. Yen, "Tracking control of shape-memory-alloy actuators based on self-sensing feedback and inverse hysteresis compensation," *Sensors*, vol. 10, no. 1, pp. 112–127, 2009.

[66] A. Badel, Q. Jinhao, G. Sebald, and D. Guyomar, "Self-sensing high speed controller for piezoelectric actuator," *Journal of Intelligent Material Systems and Structures*, vol. 19, no. 3, pp. 395–405, 2008.

[67] I. A. Ivan, M. Rakotondrabe, P. Lutz, and N. Chaillet, "Current integration force and displacement self-sensing method for cantilevered piezoelectric actuators," *Review of Scientific Instruments*, vol. 80, no. 12, pp. 126 103–1–126 103–3, 2009.

[68] B. K. Nguyen and K. K. Ahn, "Feedforward control of shape memory alloy actuators using fuzzy-based inverse Preisach model," *Control Systems Technology, IEEE Transactions on*, vol. 17, no. 2, pp. 434–441, 2009.

[69] M. Rakotondrabe, I. Ivan, S. Khadraoui, C. Clevy, P. Lutz, and N. Chaillet, "Dynamic displacement self-sensing and robust control of cantilever piezoelectric actuators dedicated for microassembly," in *Advanced Intelligent Mechatronics (AIM), IEEE/ASME International Conference on*, 2010, pp. 557–562.

[70] T. Takigami, K. Oshima, and Y. Hayakawa, "Application of self-sensing actuator to control of a cantilever beam," in *American Control Conference, Proceedings of the*, vol. 3, 1997, pp. 1867–1872.

[71] J. Qiu and M. Haraguchi, "Vibration control of a plate using a self-sensing piezoelectric actuator and an adaptive control approach," *Journal of Intelligent Material Systems and Structures*, vol. 17, no. 8-9, pp. 661–669, 2006.

[72] U. Boettcher, L. Matthes, B. Knigge, R. A. Callafon, and F. E. Talke, "Suppression of cross-track vibrations using a self-sensing micro-actuator in hard disk drives," *Microsystem Technologies*, vol. 18, no. 9-10, pp. 1309–1317, 2012.

[73] T. M. Wang, Z. Y. Shi, D. Liu, C. Ma, and Z. H. Zhang, "An accurately controlled antagonistic shape memory alloy actuator with self-sensing," *Sensors*, vol. 12, no. 6, pp. 7682–7700, 2012.

[74] H. Ikeda and T. Morita, "High-precision positioning using a self-sensing piezoelectric actuator control with a differential detection method," *Sensors and Actuators A: Physical*, vol. 170, no. 1âĂŞ2, pp. 147–155, 2011.

[75] P. Dernier, "Structural investigation of the metal-insulator transition in V_6O_{13}," *Materials Research Bulletin*, vol. 9, no. 7, pp. 955–963, 1974.

[76] J. Feinleib and W. Paul, "Semiconductor-to-metal transition in V_2O_3," *Physical Review*, vol. 155, pp. 841–850, 1967.

[77] K. Kosuge, "The phase diagram and phase transition of the V_2O_3-V_2O_5, system," *Journal of Physics and Chemistry of Solids*, vol. 28, no. 8, pp. 1613–1621, 1967.

[78] W. Burkhardt, T. Christmann, B. Meyer, W. Niessner, D. Schalch, and A. Scharmann, "W- and F-doped VO_2 films studied by photoelectron spectrometry," *Thin Solid Films*, vol. 345, no. 2, pp. 229–235, 1999.

[79] S. Kabashima, T. Goto, K. Nishimura, and T. Kawakubo, "Impurity conduction in Ti-doped VO_2 studied by microwave frequency conductivity," *Journal of the Physical Society of Japan*, vol. 32, no. 1, pp. 158–163, 1972.

[80] M. Marezio, D. B. McWhan, J. P. Remeika, and P. D. Dernier, "Structural aspects of the metal-insulator transitions in Cr-doped VO_2," *Physical Review B*, vol. 5, pp. 2541–2551, 1972.

[81] T. Phillips, R. Murphy, and T. Poehler, "Electrical studies of reactively sputtered Fe-doped VO_2 thin films," *Materials Research Bulletin*, vol. 22, no. 8, pp. 1113–1123, 1987.

[82] J. Laverock, A. R. H. Preston, D. Newby, K. E. Smith, S. Sallis, L. F. J. Piper, S. Kittiwatanakul, J. W. Lu, S. A. Wolf, M. Leandersson, and T. Balasubramanian, "Photoemission evidence for crossover from Peierls-like to Mott-like transition in highly strained VO_2," *Physical Review B*, vol. 86, pp. 195 124–1–195 124–5, 2012.

[83] L. Jiang and W. Carr, "A surface micromachined light modulator based on vanadium dioxide array," in *Micro Electro Mechanical Systems, IEEE International Conference on. (MEMS)*, 2004, pp. 57–60.

[84] S. Chen, H. Ma, X. Yi, H. Wang, X. Tao, M. Chen, X. Li, and C. Ke, "Optical switch based on vanadium dioxide thin films," *Infrared Physics & Technology*, vol. 45, no. 4, pp. 239–242, 2004.

[85] N. Fieldhouse, S. M. Pursel, M. W. Horn, and S. S. N. Bharadwaja, "Electrical properties of vanadium oxide thin films for bolometer applications: processed by pulse dc sputtering," *Journal of Physics D: Applied Physics*, vol. 42, no. 5, pp. 055 408–1–055 408–6, 2009.

[86] J. Zhou, Y. Gao, Z. Zhang, H. Luo, C. Cao, Z. Chen, L. Dai, and X. Liu, "VO_2 thermochromic smart window for energy savings and generation," *Scientific Reports*, vol. 3, pp. 03 029–1–03 029–5, 2013.

[87] W. W. Li, J. J. Zhu, J. R. Liang, Z. G. Hu, J. Liu, H. D. Chen, and J. H. Chu, "External electric field manipulations on structural phase transition of vanadium dioxide nanoparticles and its application in field effect transistor," *The Journal of Physical Chemistry C*, vol. 115, no. 47, pp. 23 558–23 563, 2011.

[88] S.-Y. Li, K. Namura, M. Suzuki, G. A. Niklasson, and C. G. Granqvist, "Thermochromic VO_2 nanorods made by sputter deposition: Growth conditions and optical modeling," *Journal of Applied Physics*, vol. 114, no. 3, pp. 033 516–1–033 516–11, 2013.

[89] Y. F. Wu, L. L. Fan, S. M. Chen, S. Chen, C. W. Zou, and Z. Y. Wu, "Spectroscopic analysis of phase constitution of high quality VO_2 thin film prepared by facile sol-gel method," *AIP Advances*, vol. 3, no. 4, pp. 042 132–1–042 132–10, 2013.

[90] J. B. Goodenough, "The two components of the crystallographic transition in VO_2," *Journal of Solid State Chemistry*, vol. 3, no. 4, pp. 490–500, 1971.

[91] V. Eyert, "The metal-insulator transitions of VO_2: A band theoretical approach," *Annalen der Physik*, vol. 11, no. 9, pp. 650–704, 2002.

[92] E. Merced, R. Cabrera, H. Coy, F. E. Fernández, and N. Sepúlveda, "Frequency tuning of VO_2-coated buckled microbridges," *Microelectromechanical Systems, Journal of*, vol. 20, no. 3, pp. 558–560, 2011.

[93] B. Viswanath, C. Ko, and S. Ramanathan, "Thermoelastic switching with controlled actuation in VO_2 thin films," *Scripta Materialia*, vol. 64, no. 6, pp. 490–493, 2011.

[94] R. Cabrera, E. Merced, and N. Sepúlveda, "A micro-electro-mechanical memory based on the structural phase transition of VO_2," *Physica Status Solidi (a)*, vol. 210, no. 9, pp. 1704–1711, 2013.

[95] A. Rúa, R. Cabrera, H. Coy, E. Merced, N. Sepúlveda, and F. E. Fernández, "Phase transition behavior in microcantilevers coated with M_1-phase VO_2 and M_2-phase VO_2:Cr thin films," *Journal of Applied Physics*, vol. 111, no. 10, pp. 104 502–1–104 502–10, 2012.

[96] R. Cabrera, E. Merced, N. Sepúlveda, and F. E. Fernández, "Dynamics of photothermally driven VO_2-coated microcantilevers," *Journal of Applied Physics*, vol. 110, no. 9, pp. 094 510–1–094 510–8, 2011.

[97] Y. Okada and Y. Tokumaru, "Precise determination of lattice parameter and thermal expansion coefficient of silicon between 300 and 1500 k," *Journal of Applied Physics*, vol. 56, no. 2, pp. 314–320, 1984.

[98] D. Kucharczyk and T. Niklewski, "Accurate X-ray determination of the lattice parameters and the thermal expansion coefficients of VO_2 near the transition temperature," *Journal of Applied Crystallography*, vol. 12, no. 4, pp. 370–373, 1979.

[99] S. TIMOSHENKO, "Analysis of bi-metal thermostats," *Journal of the Optical Society of America*, vol. 11, no. 3, pp. 233–255, 1925.

[100] W. A. Brantley, "Calculated elastic constants for stress problems associated with semiconductor devices," *Journal of Applied Physics*, vol. 44, no. 1, pp. 534–535, 1973.

[101] W. Fan, S. Huang, J. Cao, E. Ertekin, C. Barrett, D. R. Khanal, J. C. Grossman, and J. Wu, "Superelastic metal-insulator phase transition in single-crystal VO_2 nanobeams," *Phys. Rev. B*, vol. 80, pp. 241 105–1–241 105–4, 2009.

[102] P. Jin, S. Nakao, S. Tanemura, T. Bell, L. Wielunski, and M. Swain, "Characterization of mechanical properties of VO_2 thin films on sapphire and silicon by ultramicroindentation," *Thin Solid Films*, vol. 343âĂŞ344, pp. 134–137, 1999.

[103] K. Y. Tsai, T. S. Chin, and H. P. D. Shieh, "Effect of grain curvature on nanoindentation measurements of thin films," *Japanese Journal of Applied Physics*, vol. 43, pp. 6268–6273, 2004.

[104] S. D. Senturia, *Microsystem Design.* Norwell, Massachusetts: Kluwer Academic Publishers, 2001.

[105] A. Werber and H. Zappe, "Thermo-pneumatically actuated, membrane-based micromirror devices," *Journal of Micromechanics and Microengineering*, vol. 16, no. 12, pp. 2524–2531, 2006.

[106] B. Yang and Q. Lin, "A latchable phase-change microvalve with integrated heaters," *Microelectromechanical Systems, Journal of*, vol. 18, no. 4, pp. 860–867, 2009.

[107] N. D. Mankame and G. K. Ananthasuresh, "Comprehensive thermal modelling and characterization of an electro-thermal-compliant microactuator," *Journal of Micromechanics and Microengineering*, vol. 11, no. 5, pp. 452–462, 2001.

[108] J. Luo, Y. Q. Fu, J. A. Williams, and W. Milne, "Thermal degradation of electroplated nickel thermal microactuators," *Microelectromechanical Systems, Journal of*, vol. 18, no. 6, pp. 1279–1287, 2009.

[109] X. Tan and J. S. Baras, "Modeling and control of hysteresis in magnetostrictive actuators," *Automatica*, vol. 40, no. 9, pp. 1469–1480, 2004.

[110] A. Janaideh and P. Krejci, "Inverse rate-dependent Prandtl & Ishlinskii model for feedforward compensation of hysteresis in a piezomicropositioning actuator," *Mechatronics, IEEE/ASME Transactions on*, vol. 18, no. 5, pp. 1498–1507, 2013.

[111] G. Gu and L. Zhu, "Modeling of rate-dependent hysteresis in piezoelectric actuators using a family of ellipses," *Sensors and Actuators A: Physical*, vol. 165, no. 2, pp. 303–309, 2011.

[112] S. Timoshenko, *Vibration problems in engineering*, 2nd ed. New Jersey: D. Van Nostrand Company, Inc., 1937, vol. 2, p. 86.

[113] R. J. Roark, W. C. Young, and R. G. Budynas, *Roark's formulas for stress and strain*, 7th ed. New York: McGraw-Hill, 2002, vol. 7, p. 138.

[114] L. D. Landau and E. M. Lifshits, *Fluid mechanics.* Massachusetts: Pergamon Press; Addison-Wesley Pub. Co., 1959, vol. 6, pp. 88–101.

[115] H. Lamb, *Hydrodynamics*, 6th ed. New York: Dover Publications, 1945, vol. 6, pp. 604–605.

[116] A. Esbrook, X. Tan, and H. K. Khalil, "Self-excited limit cycles in an integral-controlled system with backlash," *Automatic Control, IEEE Transactions on*, 2013, 10.1109/TAC.2013.2281859.

[117] A. Cavallo, C. Natale, S. Pirozzi, and C. Visone, "Limit cycles in control systems employing smart actuators with hysteresis," *Mechatronics, IEEE/ASME Transactions on*, vol. 10, no. 2, pp. 172–180, 2005.

[118] Z. Lai, D. Y. Xue, J.-K. Huang, and C. Mei, "Panel flutter limit-cycle suppression with piezoelectric actuation," *Journal of Intelligent Material Systems and Structures*, vol. 6, no. 2, pp. 274–282, 1995.

[119] Y. Zhou, X. Chen, C. Ko, Z. Yang, C. Mouli, and S. Ramanathan, "Voltage-triggered ultrafast phase transition in vanadium dioxide switches," *Electron Device Letters, IEEE*, vol. 34, no. 2, pp. 220–222, 2013.

[120] A. S. Alexandrov, A. M. Bratkovsky, B. Bridle, S. E. Savelev, D. B. Strukov, and R. S. Williams, "Current-controlled negative differential resistance due to joule heating in TiO_2," *Applied Physics Letters*, vol. 99, no. 20, pp. 202 104–1–202 104–3, 2011.

[121] N. Ma, B. Shen, F. J. Xu, L. W. Lu, Z. H. Feng, Z. G. Zhang, S. B. Dun, C. P. Wen, J. Y. Wang, F. Lin, D. T. Zhang, and M. Sun, "Current-controlled negative differential resistance effect induced by gunn-type instability in n-type GaN epilayers," *Applied Physics Letters*, vol. 96, no. 24, pp. 242 104–1–242 104–3, 2010.

[122] S. Kumar, M. D. Pickett, J. P. Strachan, G. Gibson, Y. Nishi, and R. S. Williams, "Local temperature redistribution and structural transition during joule-heating-driven conductance switching in VO_2," *Advanced Materials*, vol. 25, no. 42, pp. 6128–6132, 2013.